The Thesis Committee for Charles Averill Harman
Certifies that this is the approved version of the following thesis:

Quantified Facies Distribution and Sequence Geometry of the Yates Formation, Slaughter Canyon, New Mexico

APPROVED BY
SUPERVISING COMMITTEE:

Supervisor:

Charles Kerans

David Mohrig

Edmund Frost, III

Quantified Facies Distribution and Sequence Geometry of the Yates Formation, Slaughter Canyon, New Mexico

by

Charles Averill Harman, B.S.

Thesis

Presented to the Faculty of the Graduate School of

The University of Texas at Austin

in Partial Fulfillment

of the Requirements

for the Degree of

Master of Science in Geological Sciences

The University of Texas at Austin

August 2011

Dedication

To my family for their constant support, encouragement, and shared wisdom.

Acknowledgements

I would like to thank my advisor Charles Kerans for guidance and inspiration in the field and the classroom. This thesis benefitted from thoughtful reviews by committee members David Mohrig and Ned Frost as well as conversations with Andrew Parker, Mark Sonnenfeld, Lyn Canter, Mahmoud Hasan Al-Nazghah, and David Hunt. Early field work benefitted from the efforts of Eric Anderson and Luke Fidler. Thanks are also due to the researchers, students, and sponsors of the Reservoir Characterization Research Laboratory (RCRL) at the Bureau of Economic Geology, to whom I am grateful for their high expectations, financial support, and camaraderie. Additional thanks to the Jackson School of Geosciences for funding of field work and to Carlsbad Caverns National Park for permission to work in Slaughter Canyon. Thanks to Whiting Petroleum Corporation for an internship looking at the subsurface Yates Fm. in the summer of 2010.

I am indebted to my friends who were a source of support through the good times and bad; may they never forget the relief a game of foosball, good music, and climbing on rocks provides.

Lastly I owe much to Dana Schultz for her patience, honesty, and strength of heart. She has been a lone voice after long days, a needed perspective outside of geology, and an essential source of inspiration.

Abstract

Quantified Facies Distribution and Sequence Geometry of the Yates Formation, Slaughter Canyon, New Mexico

Charles Averill Harman, M.S.Geo.Sci.

The University of Texas at Austin, 2011

Supervisor: Charles Kerans

This study uses a new integrated outcrop data and airborne lidar from Slaughter Canyon, New Mexico, to quantitatively characterize the cycle-scale facies architecture within the G23-G26 high frequency sequences of the Yates Formation. High frequency cycle-scale mapping of these sequences shows sedimentological evidence for accommodation reduction associated with the Permain composite sequence (CS) 13 highstand (G23-G25). Development of the G26 HFS additionally demonstrates the isochronous balance of mixed carbonate-siliciclastic deposition across the Yates-Capitan reef-rimmed shelf during the initial CS-scale transgression following significant exposure and bypass of sand across the shelf.

This sequence framework is quantitatively analyzed using progradation to aggradation (P/A) ratios, facies proportions, facies tract dip width, and facies tract bedding angles to evaluate the interplay of eustacy and syndepositional deformation as drivers of stratigraphic architecture. The sequences defined here developed in response to both eustacy and syndepositional deformation, but individual facies distributions and

cycle stacking patterns were largely controlled by eustacy; while facies, cycle, and sequence thicknesses as well as facies bedding angles were locally influenced by syndepositional faulting. A reconstruction of each high frequency sequence and stepwise documentation of post-depositional fault displacement and HFS basinward rotation was generated using the lidar data. This analysis shows that the G23-G26 HFS developed basinward-dipping depositional topography from the shelf crest to the shelf margin reef. This geometry was largely unaltered by syndepositional faults during individual HFS deposition, but was rotated basinward shortly thereafter by younger fault movement.

The accommodation trends recorded in this largely shelf crest to shelf margin window can be additionally projected into the middle shelf producing zones of the prolific Yates-aged reservoirs on the Northwest Shelf and Central Basin Platform.

Table of Contents

List of Tables

List of Figures

List of Plates

INTRODUCTION

Detailed outcrop studies are instrumental in the development of high-resolution sequence stratigraphic frameworks that organize complex facies assemblages into genetically-related time equivalent units according to variations in accommodation and depositional processes (Van Wagoner et al., 1990; Kerans and Fitchen, 1995). This study quantifies outcrop facies geometry within a sequence stratigraphic framework to describe and compare intrinsic and extrinsic stratigraphic variables (Kerans and Tinker, 1999), aiding the identification of dominant controls on facies architecture and sequence development. Understanding of the Capitan depositional profile has evolved with the integration of observed syndepositional faulting and deformation (Hunt et al., 2002; Kosa et al., 2003; Hunt et al., 2005; Kosa and Hunt, 2005, 2006a, 2006b), modeled differential compaction (Resor and Flodin, 2010), and platform margin collapse (Rush and Kerans, 2010). Interpretation of the processes that controlled the Capitan System's profile also vary from fault-dominated in Seven Rivers-Yates-Capitan in Slaughter Canyon (Hunt et al., 2002) to facies stacking pattern-dominated, temporarily modified by brittle failure, basinward tilting, and mass wasting in uppermost Yates-Tansill-Capitan in Walnut Canyon (Rush and Kerans, 2010). An outcrop-based, high-resolution, quantified sequence stratigraphic model was developed to test the relative importance of each process through analysis of facies distribution, geometry, and the resulting depositional profile of the upper Yates-Capitan shelf in Slaughter Canyon. This model also provides a predictive framework for analogous, data-limited subsurface equivalents (Kerans et al. 1994).

The Guadalupe Mountains of Texas and New Mexico are frequently targeted for stratigraphic research due to the number of excellent, kilometer-scale shelf-to-basin

outcrops of Leonardian through Guadalupian mixed carbonate-siliciclastic depositional systems along the northwestern edge of the Delaware Basin. The Yates Formation and the equivalent Capitan Reef are well exposed within and to the northeast of McKittrick Canyon and dominate the northeastern wall of Slaughter Canyon. Numerous authors have documented the value of these large-scale outcrops with Borer and Harris (1995), Tinker (1996, 1998), Osleger (1998), Kerans and Tinker (1999), Osleger and Tinker (1999), and Rush and Kerans (2010) describing the high-frequency sequence evolution of the Seven Rivers-Yates-Tansill-Capitan reef-rimmed shelf in McKittrick, Slaughter, Walnut, and Dark canyons. The adaptation of terrestrial scanning light detection and ranging (lidar) to outcrop geology (Bellian et al., 2005) additionally provides the means to generate quantified three-dimensional stratigraphic models (e.g. Janson et al. 2007; Phelps and Kerans, 2007; Phelps et al. 2008; Pyles et al. 2010) which show seismic-scale stratal geometry and contain the data coverage and resolution of an outcrop.

Recent work on syndepositional deformation of the Yates Formation and the equivalent Capitan reef has emphasized a strong fault-related control over thickness, facies, and stratal geometry (Hunt et al., 2002) contrary to the previously defined dominant factors of eustasy and depositional topography (Kerans and Tinker, 1999). This study uses stratigraphic and sedimentologic field data (measured sections, facies and surface mapping to photomosaics, and thin section petrology) integrated with a recently acquired airborne lidar survey of the canyon to create a high resolution, quantifiable digital outcrop model. Through the quantitative analysis of cycle-scale facies distribution, sequence development, and stratal geometry I address the balance between syndepositional deformation and eustasy in the development of the G23 to G26 high frequency sequences (HFS) of the Yates-Capitan shelf.

GEOLOGIC SETTING

The Guadalupe Mountains of Texas and New Mexico are composed of the exhumed Guadalupian-aged strata of the northwestern edge of the Delaware Basin (King, 1948) (Figure 1). Basin and range extensional tectonics created NNW-SSE oriented high-angle normal faults, which formed laterally continuous and relatively undeformed world-class outcrops along the Western and Shattuck Escarpments (King, 1948; Newell, 1953; Hayes, 1964). Further east, erosional canyons including McKittrick, Big, Double, Slaughter, Rattlesnake, and Walnut also create km-scale generally dip-parallel outcrops exposing a combination of shelf, margin, slope, and basinal strata (King, 1948; Hayes, 1964). The Guadalupes show a gentle structural dip of 1-2 degrees to the east, therefore vertical section is gained by moving to the topographically lower but stratigraphically higher eastern canyons (King, 1948) (Figure 2). Slaughter Canyon is an ideal location to observe the Yates Formation as it is well exposed for more than 4 km along the generally dip-parallel northeastern wall of the canyon. The Yates Formation is progressively eroded to the north, as it transitions from resistant dolomite-dominated facies to erosion-prone sand and evaporite-dominated facies. Significant research on these updip Yates facies has been conducted using subsurface data from the Northwest Shelf and Central Basin Platforms further to the east (Borer and Harris, 1991a, 1991b, 1995; Andreason, 1992).

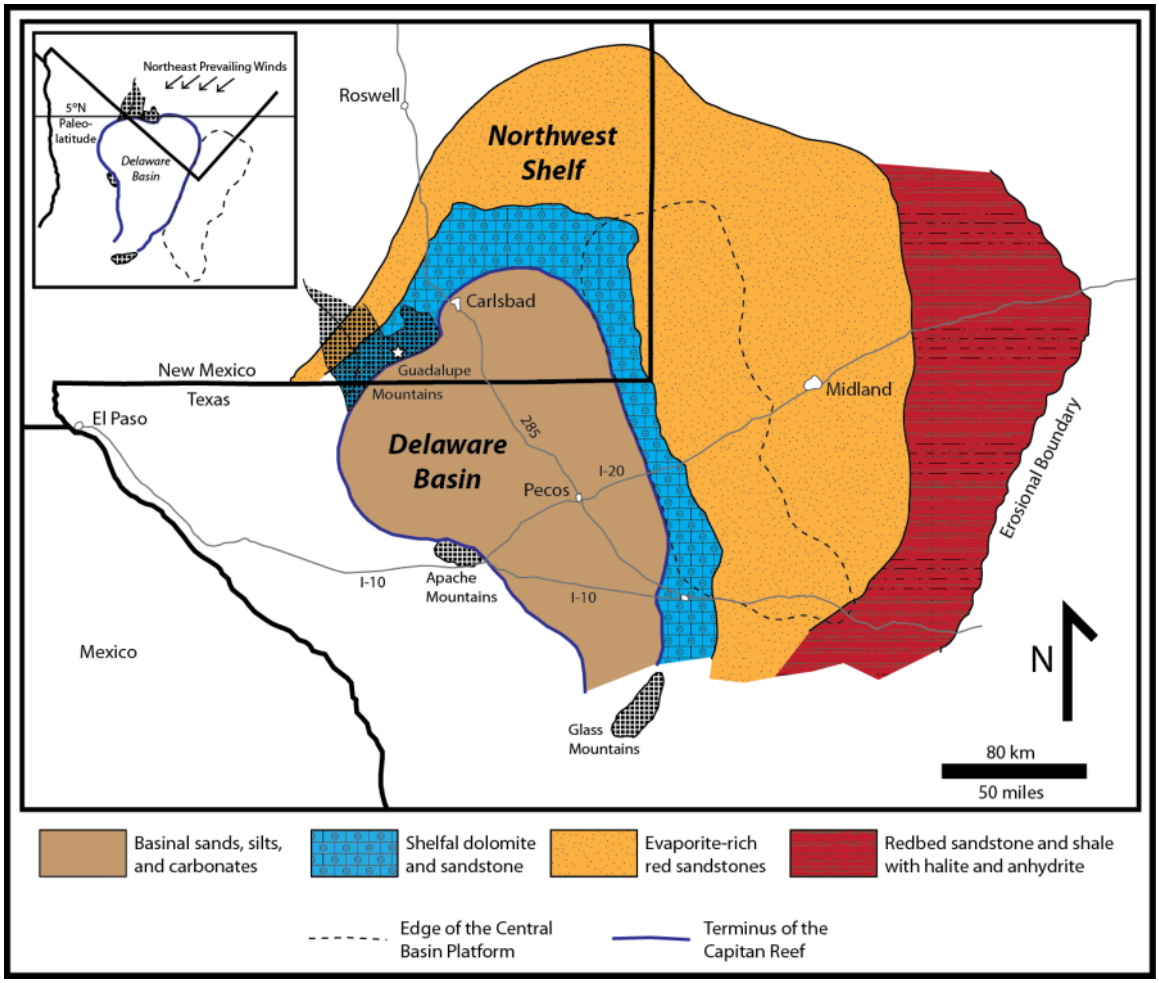

Figure 1: Map of relevant geographic and geologic areas close to the Guadalupe Mountains. The paleogeographic regions after Ward et al. (1986) represent general Yates-Seven Rivers-Queen shelf environments. During Tansill deposition, the sandy evaporitic regions evolved to be evaporite-dominated. Inset shows paleolatitude, orientation, and prevailing wind directions for the Middle Permian, after Kerans and Tinker (1999) and Walker et al. (1995).

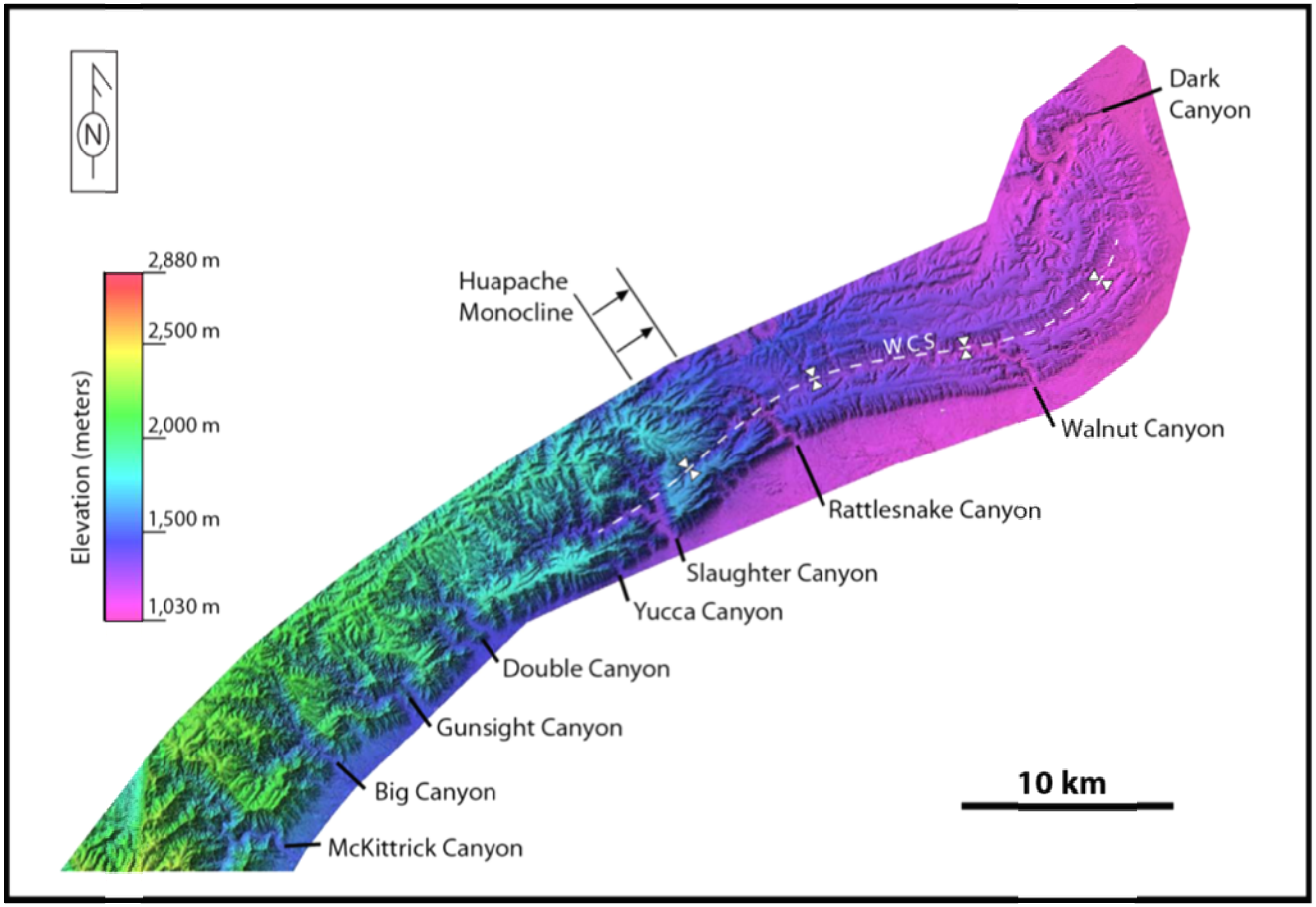

Figure 2: Shaded and elevation-colored DEM of the eastern Guadalupe Mountains from unpublished RCRL lidar data. Note that elevation decreases to the east, following a structural 1-2 degree dip (enhanced at the Huapache Monocline). A trellis drainage pattern dominates the southeastern escarpment (Kosa and Hunt, 2006b), best illustrated by the strike-parallel Walnut Canyon Syncline (WCS).

The Yates Formation was deposited across a mixed carbonate-siliciclastic-evaporite reef-rimmed shelf grading into the time-equivalent Capitan Reef at the margin of the Northwest Shelf (King, 1948; Newell et al., 1953; Hayes, 1964; Silver and Todd, 1969; Kendall, 1969; Dunham, 1972; Meissner, 1972; Smith, 1974; Esteban and Pray, 1977; Neese and Schwartz, 1977; Yurewicz, 1977; Ward et al., 1986; Candelaria, 1982; Borer and Harris, 1989; Garber et al., 1989; Hurley, 1989; Borer and Harris, 1991; Andreason, 1992; Mutti and Simo, 1993). This reef-rimmed shelf formed a shallow perimeter around the Delaware Basin of New Mexico and Texas (Figure 1), as part of a series of carbonate margins which surrounded the Delaware and Midland Basins from Leonardian to Guadalupian time (King, 1948; Newell et al., 1953; Saller et al., 1999).

Structurally, the Delaware Basin developed during the Late Mississippian-Early Permian, coincident with the Ouachita-Marathon orogeny. This tectonic event occurred along basement-involved thrust faults which elevated the Central Basin Platform relative to the Delaware Basin to the west and the Midland Basin to the east (Yang and Dorobek, 1994; Ye et al. 1996). Displacement ceased by the end of the Wolfcampian (Ye et al. 1996) and by the Late Guadalupian the Midland Basin had a flat, filled topography that had coalesced with the Central Basin Platform, thereby making the Delaware Basin the locus of Yates-Capitan deposition (King, 1948).

The Yates Formation is younger than all but the Tansill Formation within the Artesia Group (Tyrrell, 1962) (Figures 3, 4). The underlying Seven Rivers and most of the Yates Formation are within the *Polydiexodina* fusulinid Zone (Wilde, 1999) while the entire Yates generally correlates to the *Postserrata* conodont Zone (Lambert et al., 2002; Rush and Kerans, 2010). The Yates-Tansill boundary is based on an upward-decrease in interbedded siliciclastics, as well as the transition from the *Codonofusiella extensa* (top Yates) to *Yabeina texana* (base Tansill) fusulinid Zones (Wilde, 1999). In the basin, the

Yates-Capitan reef-rimmed shelf is equivalent to the fine-grained siliciclastic Bell Canyon Formation, with the slope to basinal Lower and Upper Radar, McCombs, and McKittrick Canyon Limestone members equating to Yates deposition (Tinker, 1998; Wilde, 1999; Rush and Kerans, 2010).

During the Late Guadalupian, the Delaware Basin was located in a tropical and arid climate near 5 degrees north paleolatitude with dominantly north-easterly winds (Ross, 1978; Irving, 1979; Bambach et al. 1980; Scotese and McKerrow, 1990; Walker et al., 1995) (Figure 1). These conditions were ideal for carbonate producing organisms to grow in shallow marine waters and for evaporite minerals to precipitate in restricted areas. It is useful to divide the Yates Formation general depositional facies tracts, characterized in a proximal-to-distal trend from an evaporite and red-bed dominated inner shelf, a dominantly lagoonal subtidal siliciclastic (porosity not occluded by evaporites) middle shelf, a tepee-pisoid rich shelf crest with minor siliciclastics and evaporites, and a carbonate rich outer shelf with open marine fauna and minor siliciclastics which grade into the Capitan shelf margin (Dunham, 1969; Smith, 1974; Esteban and Pray, 1977; Garber et al. 1989; Borer and Harris, 1991; Andreason, 1992, Kerans and Harris, 1993) (Figure 5). The width and presence of these facies tracts changes with accommodation over time with the shelf margin being the most narrow (often < 100 m).

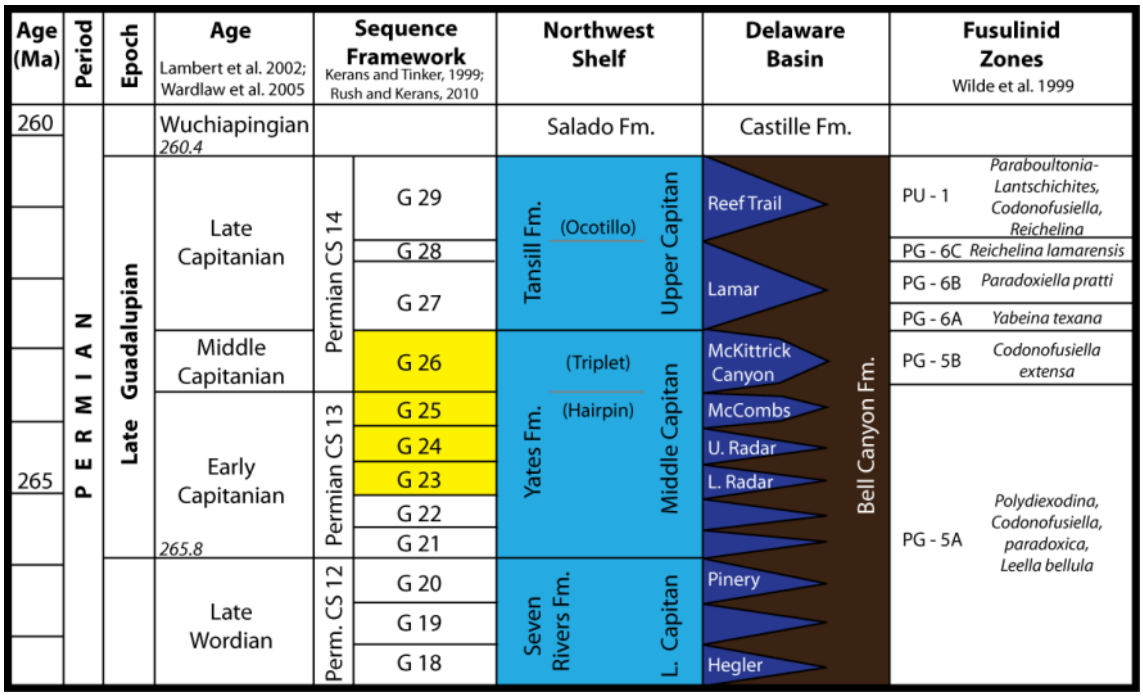

Figure 3: Stratigraphic chart for the Late Guadalupian after Rush and Kerans (2010). This study focuses on the G23-G26 HFS which represent the late transgression and highstand of the Permian CS 13 (G23-G25) and the early transgression of the Permian CS 14 (G26); as defined by Kerans and Tinker (1999) and Rush and Kerans (2010). These HFS's are composed of interbedded sandstones, dolomites, and limestones of the shelfal Yates Formation, the time-equivalent Capitan Reef margin and forereef, and the interbedded slope to basinal sands, silts, and limestones of the Bell Canyon Formation. Informal names within the Yates and Tansill Formations from Esteban and Pray (1977). The majority of the succession within this study (G23-G25) is within the same biostratigraphic zone (PG-5a), characterized by the presence of the large fusulinid, *Polydiexodina* (Wilde et al., 1999).

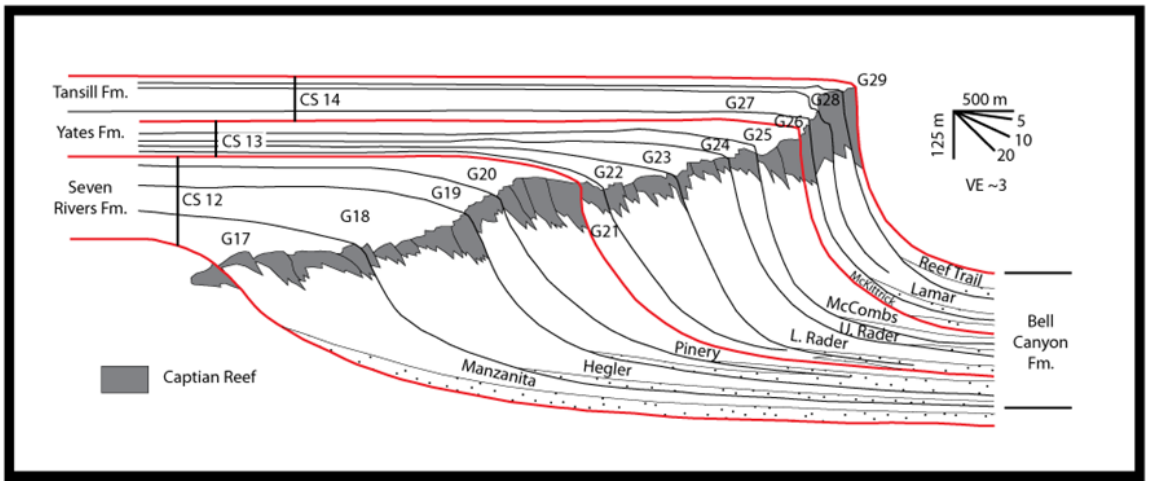

Figure 4: Generalized shelf-to-basin stratigraphic cross section of the Capitan Shelf built from exposures in McKittrick, Walnut, and Dark Canyons; after Tinker (1998) and Rush and Kerans (2010). Note the highly progradational nature of the Yates-Capitan reef-rimmed shelf (CS 13) and its subsequent transition to greater aggradation during the deposition of the Tansill Formation (CS 14).

PREVIOUS WORK

The mixed carbonate-clastic shelves around the Delaware and Midland Basins have long been a laboratory for research in stratigraphy, sedimentology, and cyclic sedimentation. Following the pioneering work by King (1948) numerous studies developed depositional models based on outcrop and subsurface data, recognized correlative cyclic siliciclastic-carbonate strata, and used the model of reciprocal sedimentation to explain these regional, lithologic alternations which later became the foundation for a modern sequence stratigraphic framework (Wilson, 1967; Silver and Todd, 1969; Meissner, 1972; Jacka et al., 1972). Recent workers in the Guadalupes have also characterized extensive syndepositional fault systems that are beginning to be integrated with the established sedimentology and stratigraphy, and further complicate questions about the primary depositional profile of the Yates-Capitan shelf.

Depositional Models

The constituent facies of the Yates Formation and its equivalents have been studied extensively in the Guadalupe Mountains and the subsurface. These differing data sources have led to a division of the Yates depositional model (Figure 5), such that outcrop studies generally focused on carbonate-rich facies within and seaward of the shelf crest (e.g. Kendall, 1969; Dunham, 1972; Smith, 1974a, 1974b; Yurewicz, 1977; Neese and Schwartz, 1977; Esteban and Pray, 1983; Babcock and Yurewicz, 1989; Candelaria, 1989; Borer and Harris, 1989; Kerans and Harris, 1993; Tinker, 1998; Osleger, 1998) while subsurface studies generally focus on dominantly siliciclastic, hydrocarbon-prone middle shelf facies (Ward et al., 1987; Borer and Harris, 1991a, 1991b, 1995; Andreason, 1992). An exception to this focus on the middle shelf in the subsurface is work done by Garber et al. (1989) on the Gulf PBD-04 research well of the shelf crest through Capitan Reef. Consequently, there are accommodation-specific

depositional models (Andreason, 1992; Tinker, 1998) for the proximal (subsurface) Yates facies and the distal (outcrop) facies; but no model for the entire system that accounts for the heterogeneity in both carbonate and siliciclastic facies (Figure 5).

The most fundamental lithologic relationship in the Yates Formation is the alternation between the deposition of sand and carbonate. These alternations occur at the cycle to sequence-scale and are characterized by (1) sand transport and bypass to the basin across the exposed carbonate shelf during low relative sea level, (2) subsequent trapping and preservation of these marine-reworked sands on the shelf during transgression, and (3) progressive gradation into carbonate deposition as carbonates initiate at the margin and force the sands into proximal lagoons (Kendall, 1969; Silver and Todd, 1969; Meissner, 1972; Mazullo et al. 1985; Fischer and Sarnthein, 1988; Borer and Harris, 1991a, 1991b; Andreason, 1992; Kerans et al. 1992; Kerans and Harris, 1993; Tinker, 1998; Osleger, 1998) (Figure 5). There is wide agreement on the further division of the Yates-Capitan Shelf into generalized facies tracts: the proximal inner shelf, middle shelf, shelf crest, outer shelf, and shelf margin (Figure 5).

The inner shelf is composed of interbedded evaporites and red beds representing a wide, evaporitic sabhka/playa/salina environment; the facies of which form a lateral seal for the prolific Yates-aged fields on the western edge of the Central Basin Platform (Ward et al., 1986; Borer and Harris, 1991a, 1991b, Andreason, 1992).

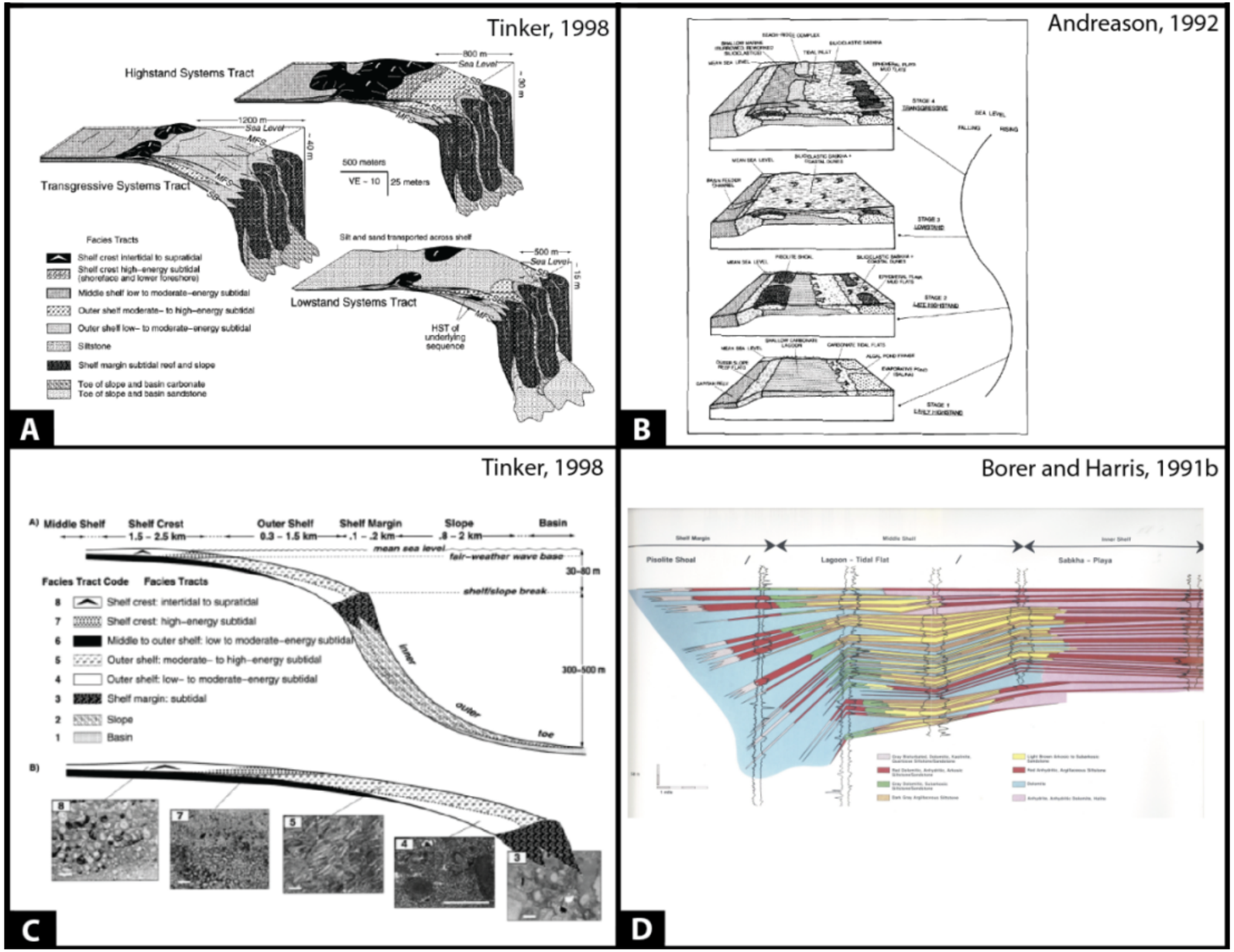
Tinker, 1998
Highstand Systems Tract
800 m
Sea Level
~ 30 m
1200 m
Sea Level
~ 40 m
MFS
Transgressive Systems Tract
500 meters
VE = 10
25 meters
Facies Tracts
Shelf crest intertidal to supratidal
Shelf crest high–energy subtidal (shoreface and lower foreshore)
Middle shelf low to moderate–energy subtidal
Outer shelf moderate– to high–energy subtidal
Outer shelf low– to moderate–energy subtidal
Siltstone
Shelf margin subtidal reef and slope
Toe of slope and basin carbonate
Toe of slope and basin sandstone
Silt and sand transported across shelf
500 m
Sea Level
~ 15 m
Lowstand Systems Tract
HST of underlying sequence
A
Andreason, 1992
B
Tinker, 1998
A) Middle Shelf
Shelf Crest
Outer Shelf
Shelf Margin
Slope
Basin
1.5 – 2.5 km
0.3 – 1.5 km
.1 – .2 km
.8 – 2 km
mean sea level
fair–weather wave base
30–80 m
Facies Tract Code
Facies Tracts
8 Shelf crest: intertidal to supratidal
7 Shelf crest: high–energy subtidal
6 Middle to outer shelf: low to moderate–energy subtidal
5 Outer shelf: moderate– to high–energy subtidal
4 Outer shelf: low– to moderate–energy subtidal
3 Shelf margin: subtidal
2 Slope
1 Basin
shelf/slope break
300–500 m
inner
outer
toe
B)
C
Borer and Harris, 1991b
Shelf Margin
Middle Shelf
Inner Shelf
Pisolite Shoal
Lagoon – Tidal Flat
Sabkha – Playa
D

Figure 5: Outcrop- and subsurface-based 2D and 3D depositional models for the Yates Formation. A) Three-dimensional, accommodation-specific depositional model for the G23 HFS from Tinker (1998), built from outcrops in McKittrick Canyon, note that the greatest detail focuses on the Shelf Crest to Margin facies tracts. B) Three-dimensional, accommodation-specific depositional model from Andreason (1992), built from core and log data from Ward County, TX; note that the greatest detail focuses on the facies tracts landward of the "pisolite shoal" (Shelf Crest). C) Generalized two-dimensional model of a Yates cycle with the location and dimensions of the constituent facies tracts from Tinker (1998). D) Two-dimensional cross section showing the location of siliciclastic facies in relation to carbonates from Borer and Harris (1991b), built from wells and cores along the Northwest Shelf and Central Basin Platform.

The middle shelf is composed of interbedded arkosic sandstones, dolomitic silty sandstones, argillaceous siltstones, microbially laminated carbonates, and intraclast-peloid wacke/packstones (Borer and Harris, 1991a, 1991b; Andreason, 1992). This facies tract represents a shallow, siliciclastic-dominated lagoon which becomes lower energy with decreasing accommodation, causing fining-upward cyclicity (Borer and Harris, 1989, 1991a, 1991b; Andreason, 1992). The arkosic sandstones of the middle shelf also serve as the main reservoir facies of the Yates-aged oil fields (Ward et al., 1986; Borer and Harris, 1991a, 1991b; Andreason, 1992).

The distinctive shelf crest facies tract is characterized by pisoids, tepee structures, fenestral fabric, microbial lamination, and thin skeletal interbeds; red anhydritic silty sandstones are also present at cycle bases and infilling underlying truncated tepee structures (Smith, 1974b; Esteban and Pray, 1983; Borer and Harris, 1989, 1991a, 1991b; Tinker, 1998). The shelf crest facies represent the topographic high of the shelf (Dunham, 1969), characterized by intertidal-supratidal islands and tidal flats (Kendall, 1969; Smith, 1974a, 1974b; Esteban and Pray, 1983; Borer and Harris, 1989, 1991a, 1991b; Kerans and Harris, 1993; Tinker, 1998). Tinker (1998) additionally included the distally-flanking ooid grainstones as a “high-energy subtidal” subdivision indicative of a foreshore-to-shoreface environment established on the seaward edge of the island complex (Tinker, 1998).

The outer shelf facies tract is composed of dominantly carbonate grainstone/rudstones to wackestones with significant skeletal and non-skeletal allochems including ooids, peloids, oncoids, intraclasts, the fusulinid *Polydiexodina*, the green alga *Mizzia*, smaller foraminifera, bivalves, gastropods, and crinoids. Basinward-thinning and divergent dolomitic sandstones are also present, sharply overlying carbonate strata and grading upward into the next carbonate units (Neese and Schwartz, 1977; Neese, 1989;

Borer and Harris, 1989, 1991b; Kerans and Harris, 1993; Tinker, 1998; Osleger, 1998; Rush and Kerans, 2010). Grain-dominated, cross-stratified fabrics are most common in the proximal outer shelf, immediately adjacent to the shelf crest; fabric and skeletal preservation indicates that depositional energy decreased in a distal direction and water depth increased (Neese and Schwartz, 1977; Babcock, 1977; Yurewicz, 1977; Esteban and Pray, 1983; Neese, 1989; Babcock and Yurewicz, 1989; Kerans and Harris, 1993; Tinker, 1998; Osleger, 1998). The outer shelf facies tract represents subtidal, high-to-low energy deposition likely above storm wave base (during the Yates) (Neese and Schwartz, 1977; Yurewicz, 1977; Neese, 1989; Kerans and Harris, 1993; Tinker, 1998; Osleger, 1998). The deepening profile from the shelf crest through the outer shelf into the shelf margin was originally proposed as the "marginal mound" of Dunham (1972), this profile is one of four in the literature (King, 1948; Newell et al., 1953; Dunham, 1972; Kirkland-George, 1992; Harris and Saller, 1999) (Figure 8) and is the most widely accepted for the Yates (Tinker, 1998; Osleger, 1998; Kerans and Tinker, 1999; Rush and Kerans, 2010).

The shelf margin facies tract is largely characterized by a framework including a diverse sponge fauna, the problematic algae *Collenella* and *Tubiphytes*, *Archaeolithoporella*, bryozoans, shelf-derived internal sediment, and cavity-filling aragonite botryoids as well as fibrous relic Mg-calcite cements and younger blocky calcite spar (Babcock, 1977; Mazzullo and Cys, 1977; Yurewicz, 1977; Wood et al., 1994, 1996; Kirkland et al., 1993, 1998). Although there are multiple depositional profiles for the Capitan Shelf Margin (Figure 8), recent workers have shown that its depth changed over time, generally becoming shallower from the Seven Rivers to the Tansill (Tinker, 1998; Kerans and Tinker, 1999). Outcrop-based depositional models of the Yates shelf margin support the marginal mound hypothesis, showing that it is consistently deeper bathymetrically than the time-equivalent shelf crest, and deeper than

or level with the outer shelf (Neese and Schwartz, 1977; Kerans et al., 1992; Kerans and Harris, 1993; Tinker, 1998; Osleger, 1998; Kerans and Tinker, 1999) (Figure5).

Sequence Stratigraphy

Modern sequence stratigraphic interpretation was applied to the late Leonardian through Guadalupian strata by Kerans et al. (1992) using the hierarchical scales of high-frequency cycles (HFCs), high-frequency sequences (HFSs), and composite sequences (CSs), modifying the terminology of Mitchum and Van Wagoner (1991). The Seven Rivers-Yates-Tansill-Capitan reef-rimmed shelf system is divided into three composite sequences (CSs), the Permian CS 12, CS 13, and CS 14, each of which is composed of transgressive, aggadational, and regressive high-frequency sequences (HFSs) which are composed of cycle sets and high-frequency cycles (HFC's) (Kerans et al., 1992; Tinker, 1996, 1998; Osleger, 1998; Kerans and Tinker, 1999) (Figures 3, 4). The Yates Formation contains the entire CS 13, which begins at Seven Rivers/Yates contact and encompasses the G21-G25 HFS (Kerans et al., 1992, Tinker, 1998; Kerans and Tinker, 1999; Rush and Kerans, 2010) (Figures 3, 4). The G26 HFS contains the upper section of the Yates Formation, and represents the early transgressive HFS of the CS 14; this HFS also coincides with the informal "Triplet" interval (Neese and Schwartz, 1977; Esteban and Pray, 1977), which is uniquely characterized by a distinct sand-carbonate-sand recessive pattern below the cliff-forming Tansill HFSs. A number of differing sequence organization schemes have been used in the literature in reference to the Yates Formation, Figure 6 summarizes these terminologies in relation to the one used for this study.

The north eastern wall of Slaughter Canyon contains the distal portion of the G20 HFS (top Seven Rivers), represented largely by basinward dipping outer shelf facies and

equivalent Capitan Reef. The location of the Seven Rivers/Yates contact (G20/G21) has varied since it was first mapped by Newell et al. (1953). Osleger (1998) mapped the contact approximately 350 meters north of where Rankey and Lehrman (1996) reported Seven Rivers toplap geometry, which was shown to be lower Yates and significantly deformed by syndepositional faulting by Hunt et al. (2002) (Figure 6). The G21 and G22 HFS in Slaughter Canyon (Y1 of Osleger, 1998) are difficult to differentiate due to syndepositional faulting and deformation (Hunt et al., 2002; Kosa et al., 2003; Kosa and Hunt, 2005, 2006a, 2006b). The overlying G23-G26 HFS are easily correlated across most of the wall (Osleger, 1998) although there is additional syndepositional fault offset throughout the canyon (Hunt et al., 2002; Kosa et al., 2003; Hunt et al., 2005; Kosa and Hunt, 2005, 2006a, 2006b) (Figure 7). The lower Tansill G27 HFS is present at the top of the southern 3km of the wall and is progressively eroded to the north, as are the G26 and G25 when the respective overlying HFSs are absent. The southern-most end of the wall is dominated by the G25-G27 reef and forereef, characterized by the sub-vertical massive cliffs of the Capitan and vegetated, basinward-dipping forereef-to-upper slope beds. The exact stratigraphic geometry of the G27 HFS is difficult to constrain as a result of the absence of well-defined marker beds or surfaces extending through the reef. However, the presence of chaotic backfilling debris-rich breccias overlying and onlapping steeper bedded G27-equivalent forereef grainflows suggests a change in deposition style associated with either platform margin collapse during the G28 lowstand (Rush and Kerans, 2010) or a late G27/early G28 transition to an escarpment-type margin (Kerans, 2011) (Figure 7). Additional biostratigraphic work using the framework of Rush and Kerans (2010) with biostratigraphic constraints developed by Tyrell (1969) and Wilde (1999) is needed to clarify the geometry and timing of these strata.

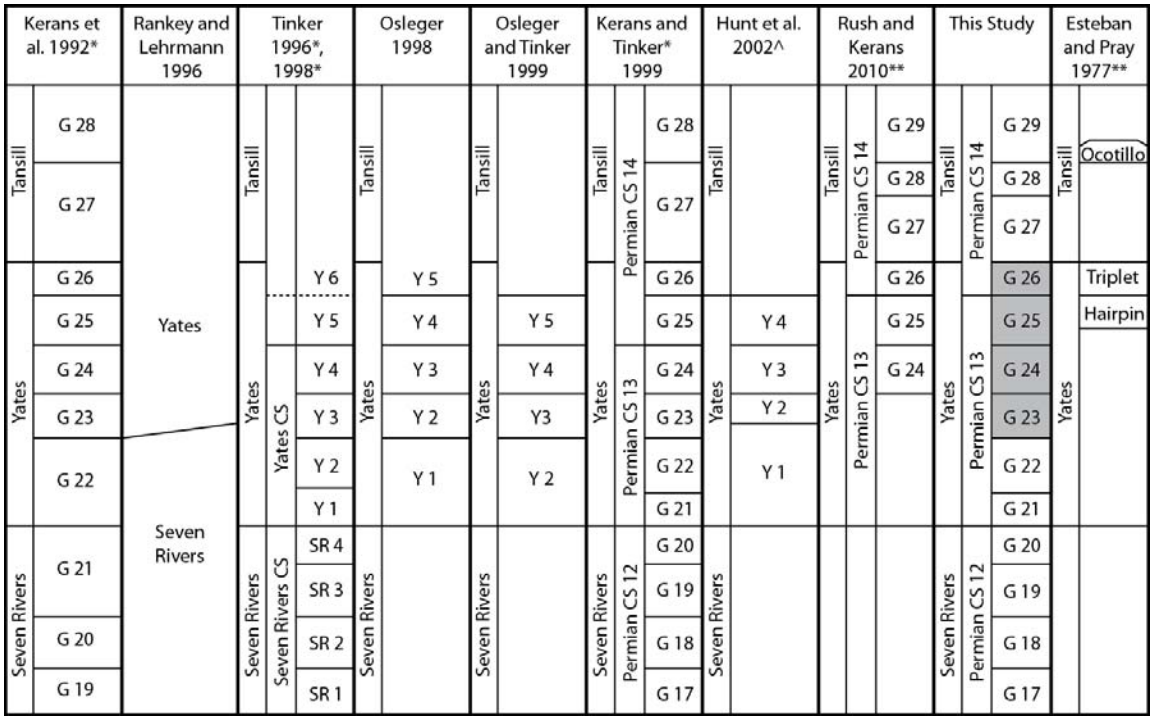

Figure 6: Various terminologies used for sequence organization of the Yates Formation. Studies noted with (*) are based on work in McKittrick Canyon, (**) studies are based on work in Walnut Canyon; all others are based on work in Slaughter Canyon. The terminology in Hunt et al. (2002) was also used in the later, related publications of Kosa et al. (2003); Hunt et al. (2005); and Kosa and Hunt (2005, 2006a, 2006b). This study is focused on the G23 to G26 HFS (shaded).

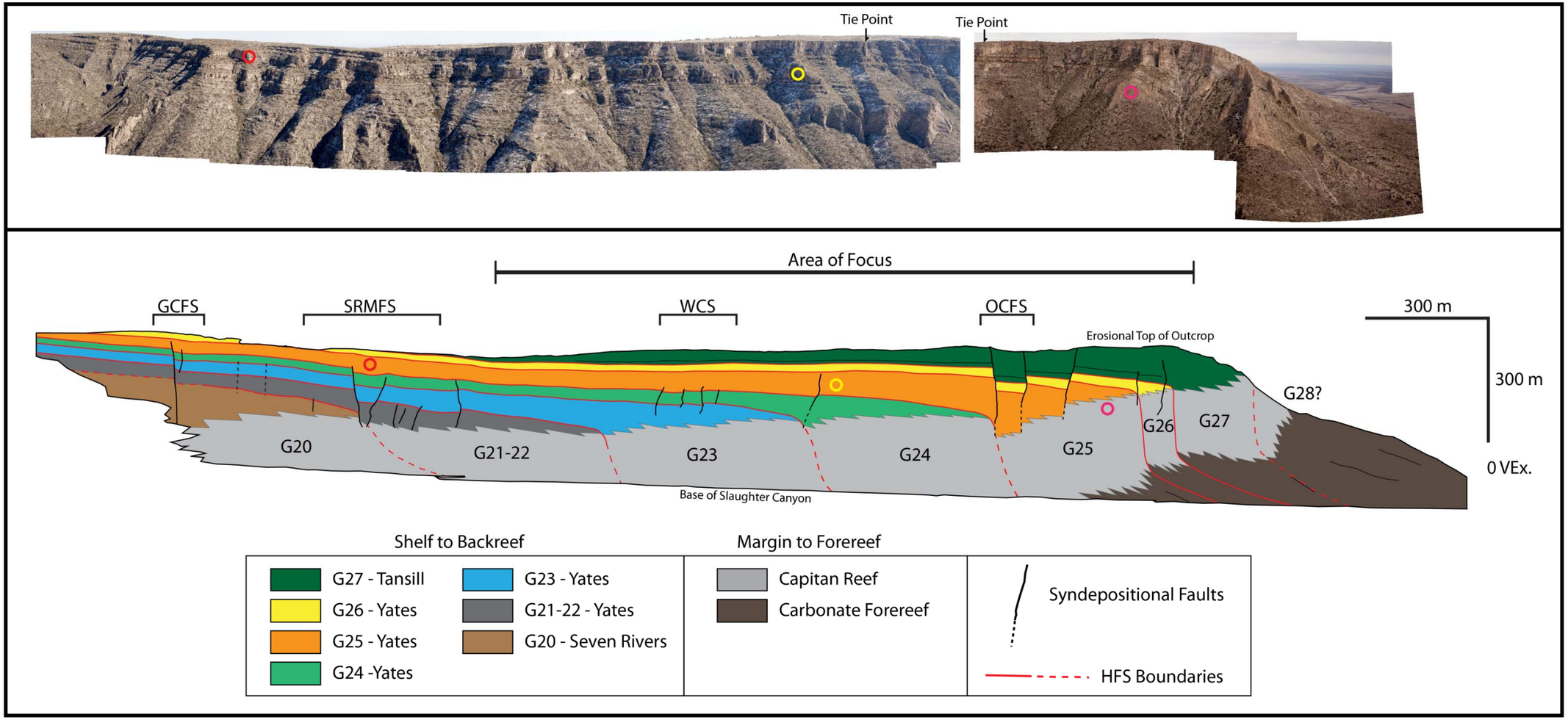

Figure 7: Top) Outcrop photomosaics of the northeastern wall of Slaughter Canyon with tie points between the photos noted with arrows and reference points to the lidar model (below) noted with colored circles. Bottom) HFS-scale cross section of the northeastern wall of Slaughter Canyon based on projected lidar interpretations, after Osleger (1998), Hunt et al. (2002), Kosa et al. (2003); and Kosa and Hunt (2005, 2006a, 2006b). Dashed lines indicate a lower level of confidence due to poor outcrop or lack of distinct bedding.

Syndepositional Faults and Related Deformation

Many workers have noted the presence of faults and neptunian dikes in the Capitan reef and Yates backreef strata (King, 1948; Hayes, 1964; Newell et al., 1953; Babcock, 1977; Yurewicz, 1977; Jagnow, 1979; Melim, 1991; Rankey and Lehrmann, 1996; Osleger, 1998; Longley, 1999) but few interpreted the faults (observed offset) to be synchronous with Permian deposition, similar to the dikes (no observed offset).

Slaughter Canyon has recently been a laboratory for the identification and classification of syndepositional faults, fractures and their respective histories of initiation, karstification, fill, and reactivation (Hunt et al., 2002; Kosa et al., 2003; Hunt et al., 2005; Kosa and Hunt, 2005, 2006a, 2006b). These follow prior studies of differential compaction in underlying Leonardian and Guadalupian prograding carbonate margins (Hunt et al., 1995) and in time equivalent Capitan strata exposed in Slaughter and McKittrick Canyons (Saller, 1996; Longley, 1999). These studies build on longstanding research into the depositional profile of the Seven Rivers-Yates-Capitan Shelf, namely the depth of the reef and the nature of the outer shelf “fall-in beds” of Hurley (1978, 1989) (Figure 8).

Hunt et al. (2002) documented a number of closely spaced syndepositional faults with up to 24 meters of offset and related deformational structures in a 500-by-200 meter outcrop window in Slaughter Canyon, noting that the faults exerted a primary control on changes in thickness, facies, and stratal geometry. The steepening, shallowing, and reversal of bedding orientation, as well as down-to-the-basin tilting and rotation of reef and backreef strata were all attributed to the observed syndepositional faulting; this was corroborated by measurements of geopetals in the Capitan reef which showed similar

values to those of Saller (1996) and Harwood and Kendall (1999) but contrasted those of Hurley (1978).

Further work within the canyon by Kosa et al. (2003) showed additional strike-parallel syndepositional faults which were vertically and laterally segmented and enlarged by karst processes, becoming sediment-filled caverns. Additional outcrop windows detailed the vertical and lateral distribution of seven different carbonate and siliciclastic cavern-filling lithologies and served as a framework for a progressive model of fault/cavern development and fill characterized by incremental fault growth overprinted by multiple dissolution events, brecciation, cavern collapse, deposition of platform-derived sediments, cementation, and dolomitization (Kosa et al., 2003).

Kosa and Hunt (2005) categorized the structural heterogeneity of the syndepositional faults in Slaughter by organizing these features into four basic types based on the upper fault termination: faults that break a surface, faults that tip out in non-growth folded strata, faults that tip out beneath growth monoclines, and buried faults with no surficial expression in overlying surfaces. Additionally, they note that these four types of faults vary vertically and laterally, and that the sense of displacement may change during the development of the fault (Kosa and Hunt, 2005).

Kosa and Hunt (2006a) synthesize a model of fault/cavern-fill distribution and timing in the context of sequence stratigraphy, noting that karstification and deposition of siliciclastic-dominated fill likely occurred during sea level lowstands while mixed carbonate-siliciclastic fills were generated during subsequent transgressions and carbonate-dominated fills, faulting and growth geometry, spar cement breccias, and dolomitizing fluids were generated during highstands. Fault/cavern fill type and heterogeneity was also found to vary with proximity to the “Y4” (G25) margin, such that faults/caverns located greater than 3 kilometers up dip were dominantly filled with

siliciclastics, had greater heterogeneity, and likely acted as dolomitizing-fluid conduits (Kosa and Hunt, 2006a). Faults from 3 to 1.4 kilometers up dip of the G25 margin had dominantly mixed carbonate-siliciclastic fill lithologies and likely acted as fluid baffles (Kosa and Hunt, 2006a). They also note that most karsted faults in the Capitan reef facies have carbonate-dominated fill and a “bulbous” morphology (Kosa and Hunt, 2006a).

Kosa and Hunt (2006b) relate the location of syndepositional faults in Slaughter, Rattlesnake, and Walnut canyons to the modern surficial geomorphology of the north eastern Guadalupe Mountains and the caves present throughout the shallow subsurface. They note that within 5 to 6 km of the final Capitan margin there is trellis drainage topography, controlled by the Permian-aged syndepositional faults, while drainage beyond that distance is largely dendritic (Kosa and Hunt, 2006b). They also identify three phases of karst development, the first (Phase I) equates to the faults and caverns developed during the Permian deposition of the Capitan Shelf (Kosa and Hunt, 2006b). The second, (Phase II) correlates to post-Permian karstification generated by dissolution of overlying evaporites and fill of arkosic sands in only the faults and fractures closest to the terminal Capitan margin (Kosa and Hunt, 2006b), inferring similar mechanisms as those documented in Johnson (1993). Although proposed ages for these post-Permian fills range from the Triassic to Pleistocene (Hill, 1996) Kosa and Hunt (2006b) conclude that they are likely Early Cretaceous due to cross-cutting relations, in agreement with King (1948), Hayes (1964), Kendall (1969), and Hill (1996, 2000). The third and final karstification event (Phase III) created the modern caves which follow both Permian syndepositional and Tertiary uplift-related structures (Kosa and Hunt, 2006b); when present, Phase III karst features were also found to consistently cross cut those of Phases I and II (Kosa and Hunt, 2006b).

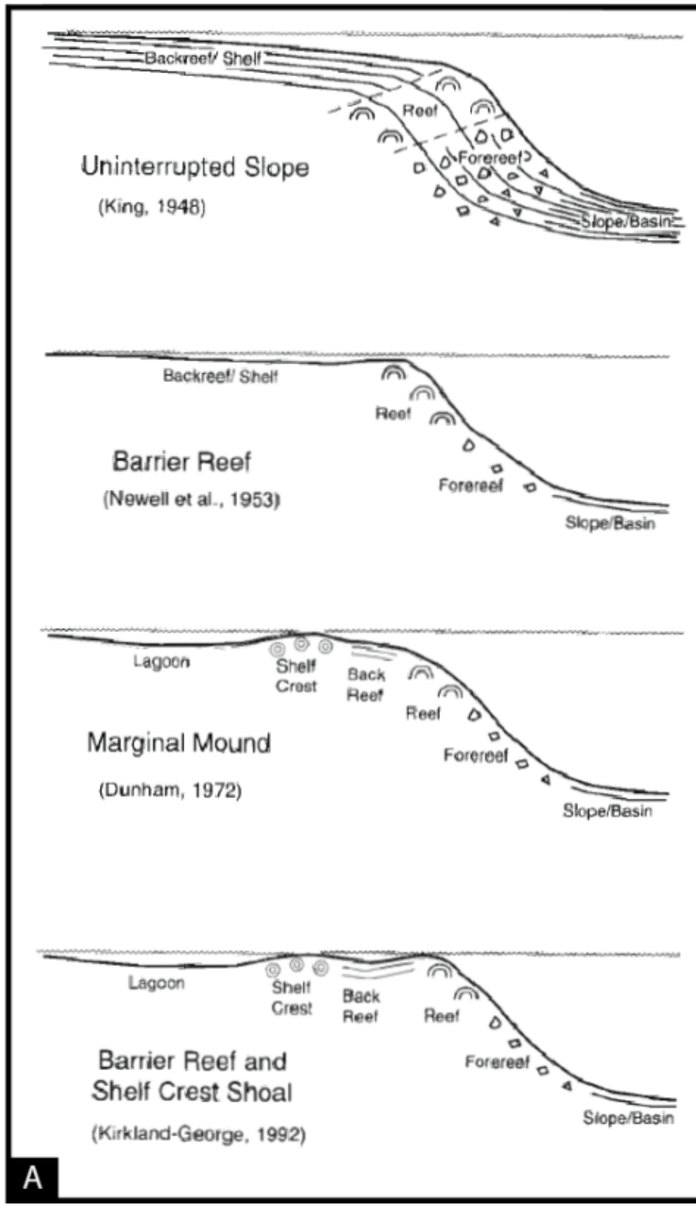
Backreef/ Shelf
Reef
Forereef
Slope/Basin
Uninterrupted Slope
(King, 1948)
Backreef/ Shelf
Reef
Forereef
Slope/Basin
Barrier Reef
(Newell et al., 1953)
Lagoon
Shelf Crest
Back Reef
Reef
Forereef
Slope/Basin
Marginal Mound
(Dunham, 1972)
Lagoon
Shelf Crest
Back Reef
Reef
Forereef
Slope/Basin
Barrier Reef and Shelf Crest Shoal
(Kirkland-George, 1992)
A

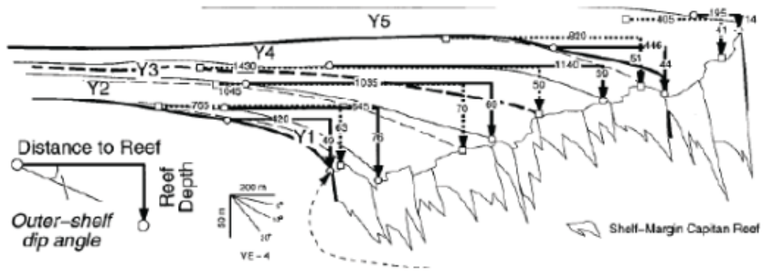
Y5
Y4
Y3
Y2
Y1
Distance to Reef
Reef Depth
Outer-shelf dip angle
Shelf-Margin Capitan Reef
B

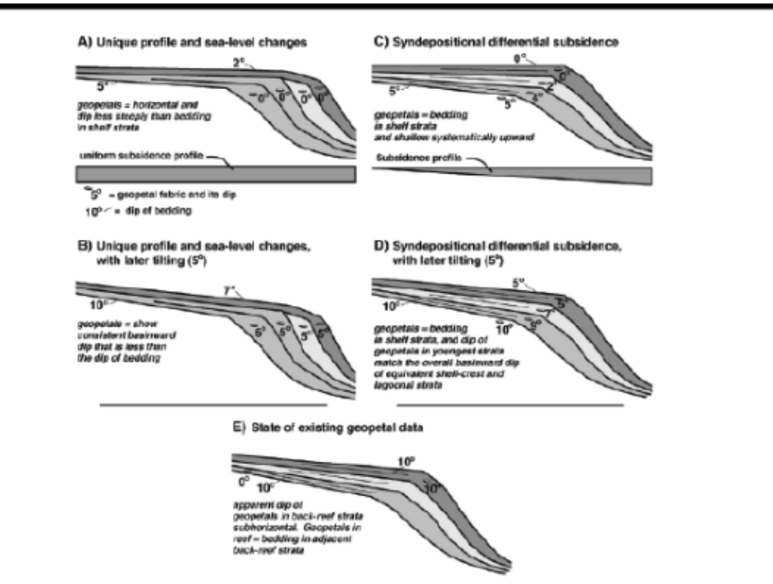
A) Unique profile and sea-level changes
C) Syndepositional differential subsidence
geopetals = horizontal and dip less steeply than bedding in shelf strata
uniform subsidence profile
= geopetal fabric and its dip
= dip of bedding
geopetals = bedding in shelf strata and shallow systematically upward
Subsidence profile
B) Unique profile and sea-level changes, with later tilting (5°)
D) Syndepositional differential subsidence, with later tilting (5°)
geopetals = show consistent basinward dip that is less than the dip of bedding
geopetals = bedding in shelf strata, and dip of geopetals in youngest strata match the overall basinward dip of equivalent shelf-crest and lagoonal strata
E) State of existing geopetal data
apparent dip of geopetals in back-reef strata subhorizontal. Geopetals in reef = bedding in adjacent back-reef strata
C

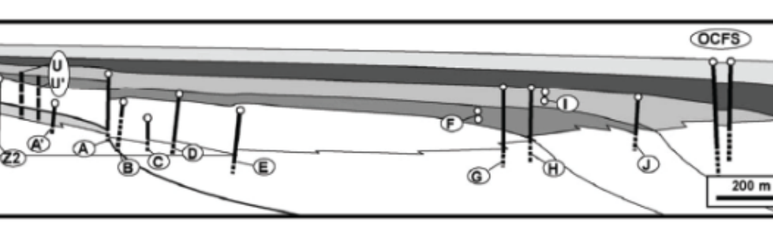
T
Y4
Y3
Y2
Y1
SR
Capitan Reef
160 m
OCFS
200 m
C
D

Figure 8: A) Diagrams of the four most prevalent interpretations of the Capitan Shelf's depositional profile after King (1948), Newell et al. (1953), Dunham (1972), and Kirkland-George, (1992); from Harris and Saller (1999). The marginal mound profile of Dunham (1972) is the most accepted for the Yates-Capitan system (Tinker, 1998), although none of these profiles infer synsedimentary deformation. B) Yates depositional profile from Tinker (1998) showing the lateral distance and depth from the Shelf Crest to the Shelf Margin in successive HFSs. C) Figure from Hunt et al. (2002) illustrating idealized profiles with variable amounts of differential subsidence as well as the current extent of data (at the time). D) Profile of Yates HFS in Slaughter Canyon from Kosa and Hunt (2005) showing the location and offset on syndepositional faults.

METHODOLOGY

The methods used for this study were fundamentally based on field work but are expanded for the construction of the lidar-based digital outcrop model. Eight vertical measured sections form the foundation of this study, with the major allochems, sedimentary structures, fabrics, and mineralogy recorded at a 10 cm resolution with additional notes concerning the location of samples, photographs, and prominent bedding planes (Figure 9). Throughout the section measuring process the prominent bedding planes, facies contacts, tepees, and faults were mapped onto printed photomosaics of the outcrop which served as a valuable tool for correlation between sections and onto the lidar survey. Photomosaics were shot with a digital SLR camera from the opposite side of the canyon (maximum of 1550 m away) at focal lengths of 100mm and 200mm; the resulting images were merged using conventional photo-stitching software. Two photomosaics taken from different perspectives at approximately the same distance from the study area were used for mapping, as the width of the study area created significant edge distortion in a mosaic of the entire outcrop taken from a single perspective. The mixed siliciclastic-carbonate lithology of the Yates Formation creates a distinct weathering profile in which the sands typically form recessive, vegetated benches and the carbonates form bedded-to-massive cliffs. This contrast is most prominent at sequence boundaries, which are characterized by sands sharply overlying carbonates, creating stair-step outcrop morphology. These surfaces were easily mapped in the photomosaics and lidar, as they were geomorphologically distinct (Figure 10). All other stratigraphic and structural features that were resolvable in the lidar were mapped, including all the faults, the top and base of the outcrop, and a number of prominent bedding planes referenced to the measured sections.

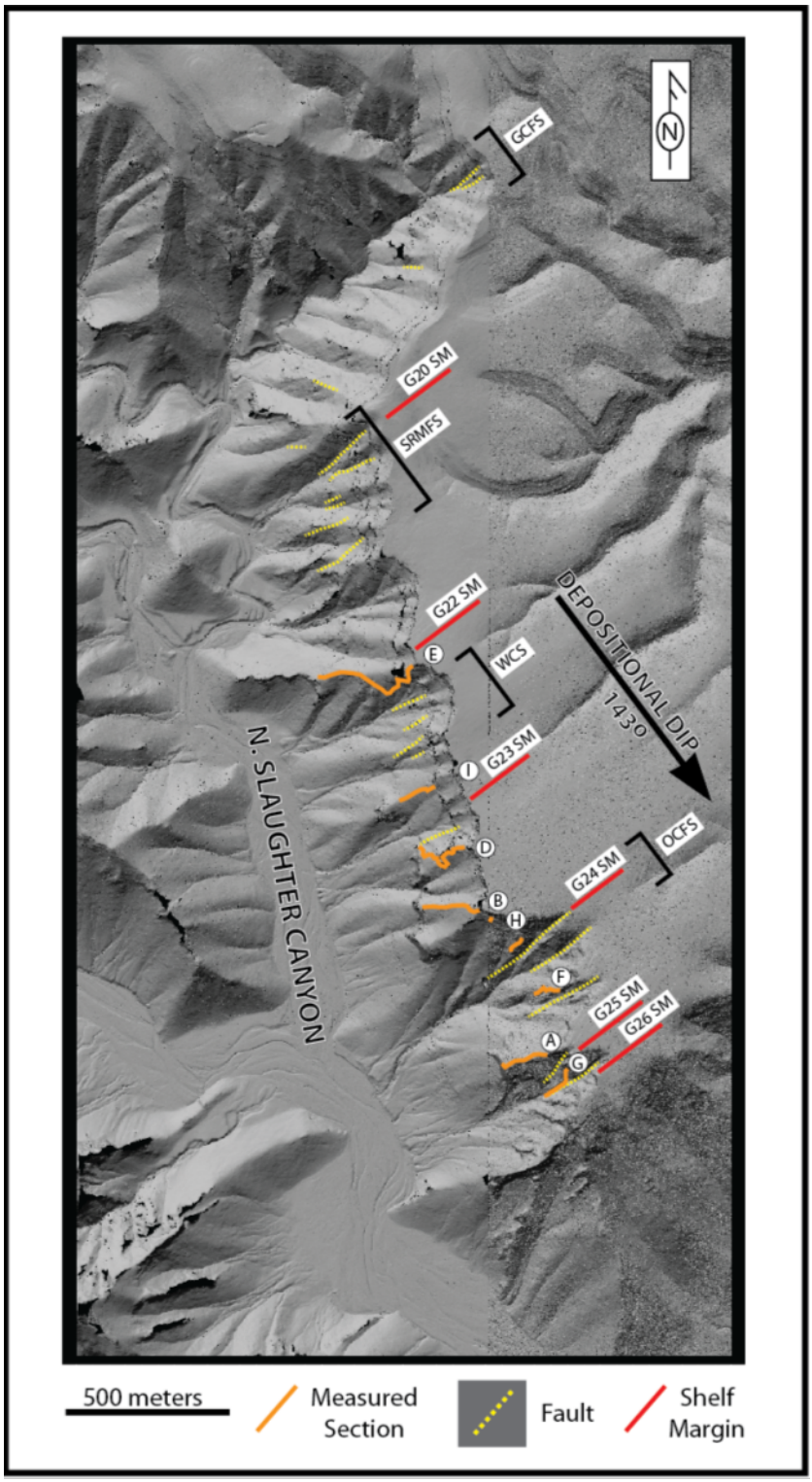
GCFS
G20 SM
SRMFS
G22 SM
E
WCS
DEPOSITIONAL DIP
143°
I
G23 SM
N. SLAUGHTER CANYON
D
OCFS
G24 SM
B
H
F
G25 SM
G26 SM
A
G
N
500 meters
Measured Section
Fault
Shelf Margin

Figure 9: Lidar-based shaded DEM showing the study area along the north east wall of Slaughter Canyon. Faults include many from Hunt et al. (2002), Kosa et al. (2003), Kosa and Hunt (2005, 2006a, 2006b); GCFS = Goat Cave Fault System, SRMFS = Seven Rivers Margin Fault System, WCS = Walnut Canyon Syncline, and OCFS = Ogle Cave Fault System. The approximate map-view locations of successive HFS terminal margins are also noted (Osleger, 1998; Hunt et al., 2002). Depositional dip value from the shelf margin trend of the Capitan in Slaughter Canyon from Kosa and Hunt (2005).

The lidar survey was taken as a part of the Guadalupe and Delaware Mountains Airborne Lidar Project which was funded by the JSG Goldhammer Chair, the Reservoir Characterization Research Laboratory (RCRL), and a consortium of oil companies (Chevron, ConocoPhillips, ExxonMobil, and StatOil). The project acquired airborne lidar over the entire southeastern edge of the Guadalupe Mountains as well as the Delaware Mountains. Acquisition and initial processing of this data was carried out by LidarUSA LLC, and was enhanced by adding point-normal referencing to the data for sun-shading capabilities by Ruben Reyes of the Bureau of Economic Geology. The entirety of Slaughter Canyon is covered by this survey with an average point spacing of less than 0.5 m; this point cloud was isolated and copied prior to interpretation in order to minimize data overload on software. Basic visualization and mapping of geologic features onto the lidar was done in Innovmetric Polyworks software; as well as later modeling and measurement. The final stratigraphic model of the northeast wall of Slaughter Canyon was generated by projecting (copies of) all the mapped geologic features on the digital outcrop model to a vertical plane oriented perpendicular (dip-parallel, 143-323 degrees) to the shelf margin trend of the Capitan in Slaughter Canyon (053-233 degrees) from Kosa and Hunt (2005). Use of a vertical plane was chosen for simplicity after much trial and error. Given the variable strike and dip created by syndepositional faulting, regional structural dip to the east, and the proximity of the Huapache Monocline, this technique provided a simple means for normalizing and comparing stratigraphic and structural geometry from a rugose outcrop.

The final cross section and related figures were constructed in drafting software using a dip-parallel vector graphic of the projected interpretations exported from Polyworks. The final cross section is "in situ" in that it has not been vertically

exaggerated, given a datum, or rotated. Individual HFS cross sections employ the upper sequence-bounding surface as a datum, which was reconstructed if offset by faults.

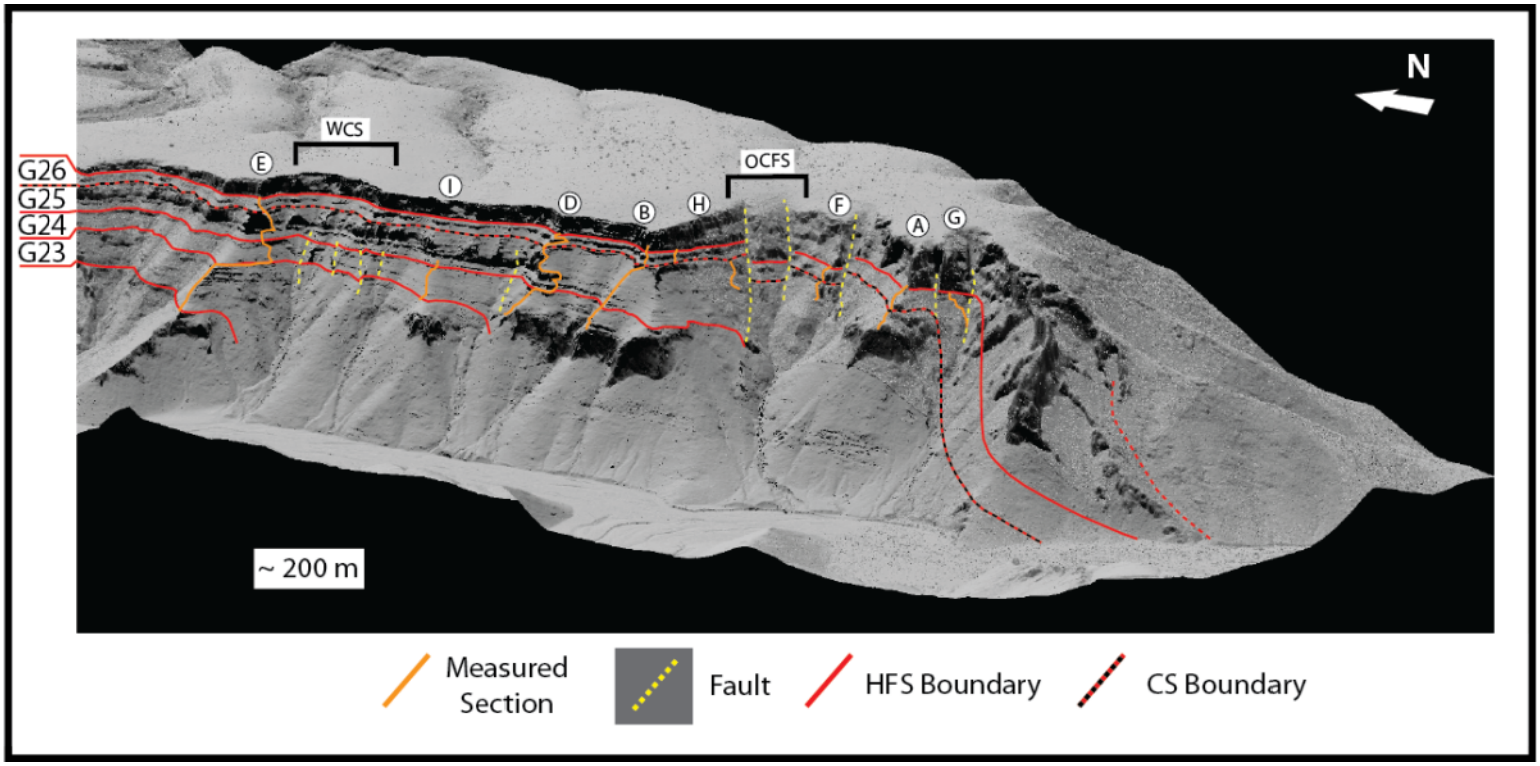

Figure 10: Oblique view of shaded lidar DEM with measured sections, faults, HFS Boundaries and CS Boundary noted. As in Figure 9, WCS = Walnut Canyon Syncline and OCFS = Ogle Cave Fault System. Note the geomorphological expression of the underlying stratigraphic and structural features.

CONSTIUENT FACIES TRACTS

The northwestern wall of Slaughter Canyon exposes the Yates-aged shelf crest, outer shelf, and shelf margin facies tracts with minor amounts of the middle shelf and upper slope (Osleger, 1998). A total of 15 facies were identified in the measured sections and mapped study area; they are organized within the well-studied and previously described facies tracts, and grouped according to energy regime (*sensu* Tinker, 1998; Table 1; Figure 11). These divisions allow for more specific identification of processes controlling deposition. The shelf crest and outer shelf are each therefore split into low/moderate and high energy sub-environments. The majority of these facies have been described in the literature (Kendall, 1969; Dunham, 1972; Smith, 1974a, 1974b; Yurewicz, 1977; Neese and Schwartz, 1977; Esteban and Pray, 1977; Babcock and Yurewicz, 1989; Candelaria, 1989; Borer and Harris, 1989; Kerans and Harris, 1993; Tinker, 1996, 1998; Osleger, 1998) therefore only facies requiring additional documentation are fully described in the text.

Middle Shelf

The middle shelf facies tract in Slaughter Canyon contains two recognized facies: dolomitic siltstone-to-sandstone and silty fenestral peloid wackestone-to-packstone. Typically, the dolomitic siltstone-to-sandstone is massive with a lower-very-fine sand grain size, rare skeletal fragments, and rare planar lamination. This facies sharply overlies carbonate facies of the shelf crest (low to moderate energy) or middle shelf. When a bed of this siliciclastic facies is traced in a basinward direction, it is common to find numerous basinward-thickening carbonate tongues within it (Figure 12). It is gradationally overlain by silty fenestral peloid wackestone to packstone, which is characterized by thin bedding, sheet cracks, irregular microbial lamination, and fenestral fabric (Figure 13). Peloids, occasional pisoids, intraclasts, and rare skeletal fragments are

the dominant allochems while there are also occasional evaporite pseudomorphs after gypsum. In the subsurface of the Central Basin Platform, Andreason (1992) additionally documented nodular and massive anhydrite facies with strontium concentrations consistent with a gypsum precursor (600-750 ppm). These evaporite facies are not preserved in the study area, but equivalent middle shelf facies distal to the evaporites were observed.

Facies Tract	*Facies Name*	*Fabric*	*Dominant Grain Types*	*Sedimentary Structures*	*Diagenesis*	*Bedding Geometry*	*Interpretation*
Middle Shelf	Silty Fenestral Peloid Wackestone-Packstone	Wackestone-Packstone	Peloids, silt-sized quartz and feldspar, rare skeletal fragments	Sheet cracks, irregular microbial lamination, fenestrae	Extensively dolomitized, evaporite psuedomorphs after gypsum	Flat, sub-meter scale bedding, recessive	Intertidal flats and washover from the Shelf Crest
Shelf Crest - Low to Moderate Energy	Tepee-Pisoid Rudstone	Rudstone	Pisoids, composite grains, superficial ooids, ooids, peloids	Meter-scale TP-buckle structures, aragonite botryoids, fenestrae, irregular laminations	Displacive syn-depositional cement growth, dolomitization	Concave-upward buckled TP's, cliff-forming	Intertidal-supratidal island complex
Shelf Crest - Low to Moderate Energy	Fenestral Coated Grain-Peloid Laminite	Mud-dominated Packstone to Rudstone	Peloids, coated grains, pisoids, ooids, skeletal fragments, rare sand	Fenestrae, irregular microbial laminations	Dolomitization, blocky isopachus cement rimming pores	Planar sub-meter scale bedding	Intertidal Flats
Shelf Crest - High Energy	Ooid-Fusulinid Grainstone/Rudstone	Grainstone/Rudstone	Polydiexodina fusulinids, ooids	Seaward-aligned (imbricate) tests, vertical rosettes of tests, seaward-dipping cross beds, beachrock intraclasts, fenestrae	Meniscus cements, isopachus radiaxial cement	Planar meter-scale bedding	Very high energy foreshore
Shelf Crest - High Energy	Ooid Grainstone	Grainstone	Ooids after peloids, skeletal fragments; peloids, pisoids, fusulinids	Shingled seaward-dipping cross beds	Extensively dolomitized, oomoldic porosity, isopachus to pore-filling blocky cement	Planar meter-scale bedding	Foreshore
Middle-Outer Shelf	Dolomitic Siltstone to UVFSS	Lower very fine to upper very fine sandstone/siltstone	Quartz, feldspars, peloids, rare skeletal fragments, fusulinids	HCS, planar thin bedded, ripple laminated, bioturbated to massive, fenestrae, LLH stromatolites	Dolomitization of peloids, dolomite and clay cements	Recessive, slope-forming	Aeolian transport, transgressive subtidal to intertidal reworking
Outer Shelf - High Energy	Skeletal-ooid Grainstone	Grainstone	Ooids, forams, fusulinids, peloids, gastropods, crinoid fragments	multidirectionally cross stratified, planar, massive	Dolomitization, micritized grain rims	Planar to seaward dipping meter-scale bedding	High energy subtidal shoal
Outer Shelf - High Energy	Skeletal-Mizzia-fusulinid Grainstone/Rudstone	Grainstone/Rudstone	Polydiexodina fusulinids, Mizzia, forams, crinoids, oncoids, peloids	Low angle cross stratification to massive	Minor Dolomitization, micritized grains, isopachus bladed and radiaxial cements	Planar to seaward dipping meter-scale bedding	High energy subtidal intershoal
Outer Shelf - Low to Moderate Energy	Skeletal-Peloid-Oncoid Grain-dominated Packstone/Rudstone	Grain-dominated Packstone/Rudstone	Oncoids, peloids, bivalves, crinoids, forams	Massive, bioturbated	Minor Dolomitization, blocky rim cement	Seaward dipping meter-scale bedding	Moderate energy subtidal
Outer Shelf - Low to Moderate Energy	Oncoid-foram-peloid Mud-dominated Packstone	Mud-dominated Packstone	Peloids, forams, small oncoids, crinoids, bivalves	Massive, likely bioturbated	Minor Dolomitization	Seaward dipping meter-scale bedding	Moderate energy subtidal
Outer Shelf - Low to Moderate Energy	Foram-peloid Wackestone	Wackestone	Peloids, forams, crinoids	Massive	Minor Dolomitization	Seaward dipping meter-scale bedding	Low energy subtidal
Outer Shelf/Margin	Crinoid-Collenella Grain-dominated packstone	Grain-dominated Packstone	Collenella sponges, crinoids, bivalves, gastropods, peloids, bryozoan fragments	Massive	Minor Dolomitization, patchy brecciated dolomite at exposure surfaces	Seaward dipping, poorly bedded	Moderate energy backreef to reef crest
Shelf Margin	Sponge-algal Boundstone	Boundstone	Sponges, Tubiphytes, internal sediment, brachiopods	Massive with internal cavities filled with aragonite botryoid cement, internal sediment (geopedals)	Aragonite Botryoids, radiaxial fibrous cement	Massive, cliff forming, 10's of meters thick	Moderate energy shelf margin reef
Upper Slope	Interclast-skeletal Grain-dominated Packstone-to-Rudstone	Grain-dominated Packstone, Grainstone, Rudstone	Sponge fragments, brachiopod fragements, crinoid fragments, reef-derived clasts, fusulinids, forams, peloids, oncoids	Graded bedding, internal sediment in shells, slumping around large clasts	Minor Dolominitzation, blocky isopachus cement	Meter-scale bedding, steep basinward dip (>20 degrees)	Upper Slope with rock fall, grain flows, debris flows

Table 1: Facies tracts, constituent facies and facies characteristics. Dominant grain types are listed in order of relative abundance.

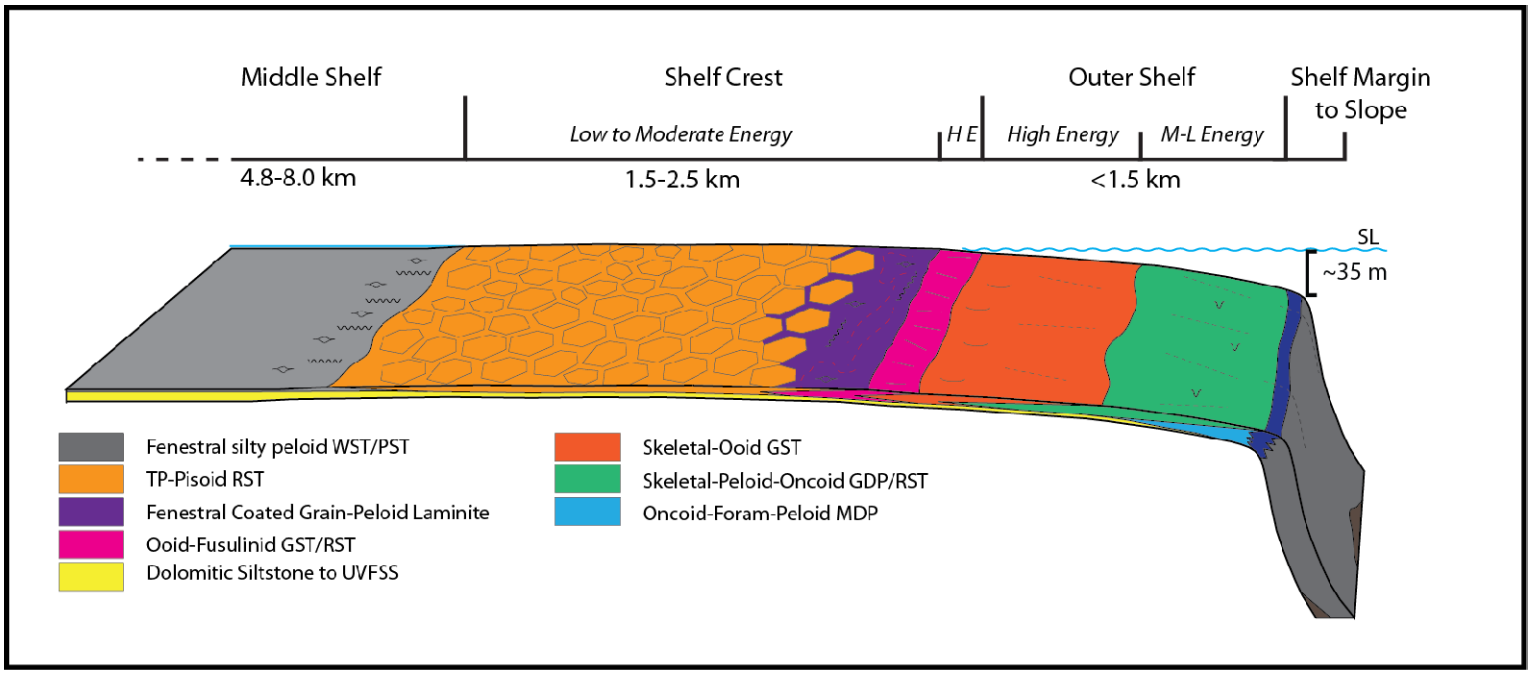

Figure 11: Depositional block diagram illustrating the proximal to distal distribution of the facies tracts further divided by depositional energy conditions (HE=High Energy; M-L=Moderate to Low). Select individual colored facies show common constituent lithology for each facies tract. After Tinker (1998).

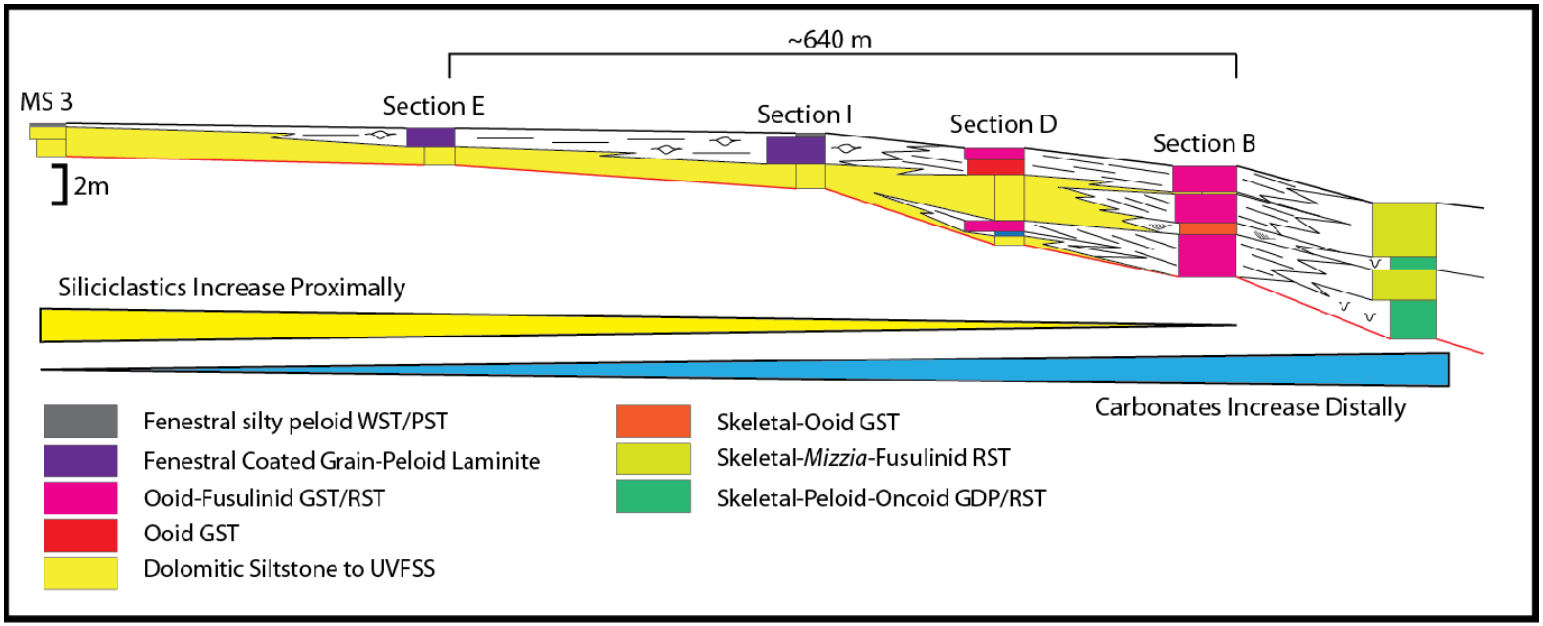

Figure 12: Cycle-scale cross section illustrating the basinward divergence of the dolomitic siltstone to sandstone facies. Note that in ~640 meters the single siliciclastic unit splits into three carbonate-bounded units all of which pinch out in close proximity to Section D. This shows the time-equivalent deposition of carbonates and siliciclastics as well as the variable record of cyclicity depending on dip position. Data from cycle 25.1.

The middle shelf facies are interpreted to represent deposits in and around a shallow, low energy, and protected lagoon landward of the shelf crest facies tract. The dolomitic siltstone to sandstone was transported onto and across the shelf by aeolian processes during periods of exposure and was reworked by shallow marine processes during the subsequent transgression (Borer and Harris, 1989, 1995; Tinker, 1996, 1998; Osleger, 1998; Harris and Saller, 1999). As transgression continued, environmental conditions on the shelf became conducive to carbonate deposition such that a gradational transition to silty fenestral peloid wackestone to packstone occurred. The basinward thinning and division of the siliciclastic facies indicates the distal transition to time-equivalent carbonate facies. The middle shelf facies were likely deposited in elevated salinity conditions as faunal diversity is limited with exception of common evidence of microbial binding organisms, and there were likely depositional evaporites proximally (Andreason, 1992). It is significant to note that the carbonates do not exhibit a “shoaling-up” fabric character, indicating that accommodation reduction within this shallow restricted lagoon was accompanied by energy reduction. Again in the subsurface of the Central Basin Platform where the middle shelf carbonates are better developed in an updip location, Andreason (1992) defined four distinct middle shelf carbonate facies: peloid/oncoid dolostone, fossiliferous peloid dolostone, fenestral-cryptalgalaminite dolostone, and dolomitic intraclast breccia. These four facies were interpreted by Andreason to represent subtidal to supratidal deposition with a maximum of 2 meters water depth.

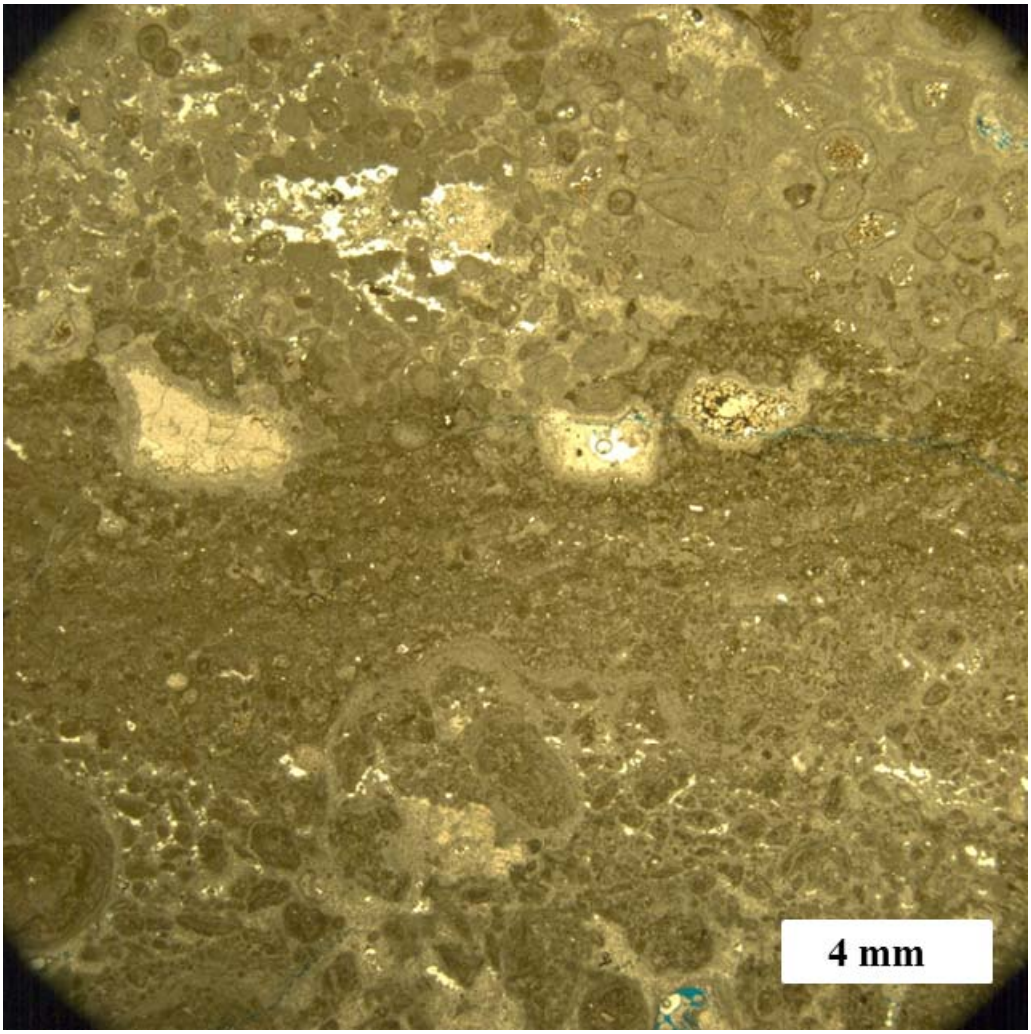

Figure 13: Photomicrograph of silty fenestral peloid wackestone-to-packstone with common intraclasts, composite grains, and superficial ooids. This facies is characteristic of the middle shelf. Sample from Measured Section B (#B-7) from cycle 26.2.

Low to Moderate Energy Shelf Crest

The low to moderate energy shelf crest is located basinward of the middle shelf and proximal to the high energy shelf crest (Figure 11); it is characterized by three facies: dolomitic siltstone-to-sandstone, tepee pisoid rudstone and fenestral coated grain-peloid laminite. As in the middle shelf, the dolomitic siltstone-to-sandstone is massive with a lower-very-fine sand texture and rare skeletal fragments although thin beds, ripple lamination, and fenestral laminated-to-LLH stromatolitic fabrics are more common (typically in that respective upward succession).

The tepee-pisoid rudstone is the indicator facies for the shelf crest, within the study area tepee structures ranged from 0.5 meters to 2 meters high. The core of the tepees is generally chaotic and variably filled with intraclasts, siliciclastics, and botryoidal aragonite cement. The flanks of the tepees are characterized by interbedded fenestral coated grain-peloid laminite, graded pisoid beds, and beds of botryoidal aragonite (Figure 14). A basinward decrease in tepee core-filling siliciclastics was also observed *sensu* Tinker (1996, 1998). The tepee-pisoid rudstone facies is also commonly truncated at cycle caps within HFS highstands, often accompanied by a thin, laterally extensive recessive siliciclastic bed in the middle of cliff-forming tepee complexes (Tinker, 1996, 1998). The fenestral coated grain-peloid laminite (mud-dominated packstone to rudstone fabric) is typically found distally adjacent to the tepees and contains variable amounts of peloids, pisoids, ooids, and coated skeletal grains. Thin (<10 cm) graded interbeds of skeletal-ooid grainstones are common.

The low to moderate energy shelf crest facies are interpreted to represent intertidal to supratidal deposition on a strike-elongate bathymetric high, separating the restricted middle shelf from the open marine outer shelf, in agreement with the conclusions of Esteban and Pray (1977, 1983), Tinker (1996, 1998), and Kerans and

Tinker (1999). Field observations of lateral facies changes and vertical stacking patterns agree with the models of Kerans and Harris (1992) and Tinker (1996, 1998) which argue for rising accommodation and early marine cementation during the aggradational building of tepee structures and their related strata. Here, the dolomitic siltstone to sandstone has the same transgressive origin as the equivalent middle shelf facies, but there is a higher relative percentage of shallow subtidal to intertidal microbial fabrics, indicating a shallower depositional environment prior to gradation into carbonates. Cycles within the low to moderate energy shelf crest are commonly capped by tepee-pisoid rudstone, but not exclusively, as the fenestral coated grain-peloid laminite caps cycles distally, and the silty fenestral peloid wackestone-to-packstone of the middle shelf caps cycles proximally.

High Energy Shelf Crest

The high energy shelf crest is located basinward of the low to moderate energy shelf crest and proximal to the high energy outer shelf (Figure 11). It is characterized by three facies: dolomitic siltstone-to-sandstone, ooid-fusulinid grainstone/rudstone and ooid grainstone. The dolomitic siltstone-to-sandstone is similar to those found in the middle shelf and low to moderate energy shelf crest, however both carbonate facies are distinct due to their low angle seaward dipping cross stratification (Figure 15). The ooid-fusulinid grainstone/rudstone is characterized by aligned fusulinid tests with a long axis-basinward orientation as well as patches of vertically aligned tests (Figures 16, 17). This facies also contains occasional ooids and rare pisoids. The ooid grainstone contains peloid-cored ooids and skeletal fragments, as well as peloids, fusulinids, and occasional pisoids (Figure 18). Dolomitization is common in both the ooid grainstone and ooid-fusulinid grainstone/rudstone. Proximity to the low-to-moderate energy shelf crest facies is

apparent as the updip contact between these two facies is gradational with both the ooid grainstone and ooid-fusulinid grainstone/rudstone becoming more crudely stratified and fenestral in a proximal direction.

The facies of the high energy shelf crest represent a shingled foreshore environment, positioned between the intertidal to supratidal flats of the low to moderate energy shelf crest and the subtidal outer shelf. The seaward-dipping cross stratification is characteristic of wave swash in the foreshore and the mud-poor fabric is indicative active winnowing of fines. The ooid-fusulinid grainstone/rudstone is interpreted to record depositional episodes (likely storms) where energy held the ooids and finer allochems in suspension, washing all but the large fusulinids onto the proximal shelf crest or distally into the outer shelf and upper slope.

High Energy Outer Shelf

The high energy outer shelf facies tract is composed of three facies: dolomitic siltstone-to-sandstone, skeletal-ooid grainstone, and skeletal-*Mizzia*-fusulinid grainstone/rudstone. The dolomitic siltstone-to-sandstone is very similar to the clastic facies of the middle shelf and shelf crest, but it generally occurs in thinner beds with higher percentages of ooids and skeletal fragments (Figure 19). The skeletal-ooid grainstone exhibits multidirectional and planar cross stratification with individual bedforms <1m high; it is also occasionally massive (Figure 20). The skeletal-ooid grainstone (shoal bodies) have a maximum dip with of 400 m and thickness of 4.5 m. Peloids and skeletal fragments are the most common ooid nuclei while intraclasts, small forams, fusulinids, peloids, gastropods, and crinoid fragments constitute the remaining allochems. The skeletal-*Mizzia*-fusulinid grainstone/rudstone shows occasional low angle cross stratification but is typically massive (Figure 21). Although fusulinids dominate,

Mizzia fragments are also common as are smaller forams, mollusk fragments, and crinoid fragments. Although not common, meniscus cements were observed in one thin section, overlain by the more common isopachus radiaxial fibrous cement (Figure 22). These facies are distinct from the high energy shelf crest due to the difference of sedimentary structures as well as the significantly higher percentage and diversity of skeletal allochems, despite similar fabrics.

The high energy outer shelf is interpreted to be the subtidal upper shoreface immediately basinward of the high energy shelf crest foreshore. Cycle bases are composed of subtidal, transgressively reworked dolomitic siltstone to sandstone with rare-to-common fusulinids, ooids, and oncoids. As in the middle shelf and shelf crest, the siliciclastics grade upward into the carbonate facies. The constituent carbonate facies represent high energy, winnowed fabrics within fair weather wave base with the skeletal-ooid grainstone representing shoals and the skeletal-*Mizzia*-fusulinid rudstone intershoals. This shoaling environment was ideal for ooid formation and the stable sand between shoals was favorable for fusulinid growth (Haynes, 1981; Tinker, 1998). The rare meniscus cement is likely of subtidal origin as no other evidence for subaerial exposure in this facies was found (Hillgartner et al., 2001). This environment grades distally into finer grained packstones and wackestones of the moderate to low energy outer shelf.

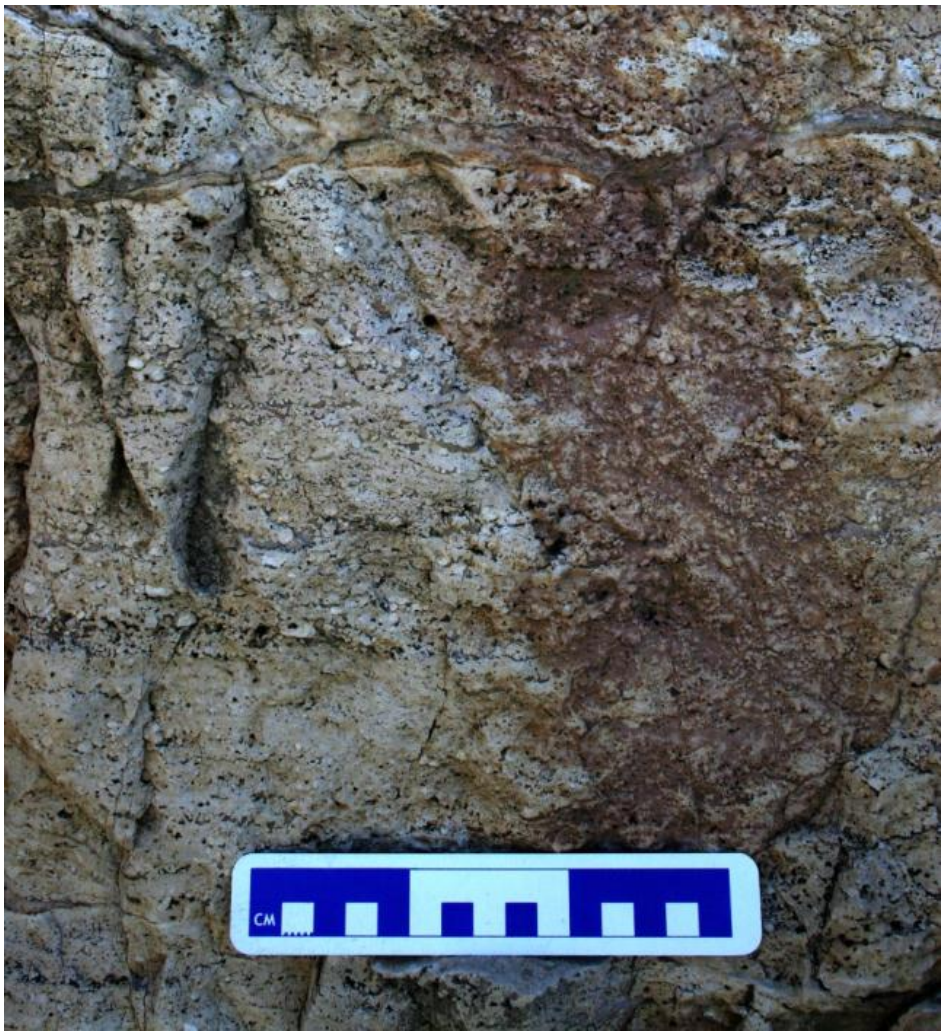

Figure 14: Outcrop photograph of fenestral coated grain-peloid rudstone with common skeletal fragments, occasional pisoids, and thin, crude bedding. This facies is typical of the low to moderate energy shelf crest facies tract. Photo taken in close proximity to Section B in the upper portion of the G25 HFS.

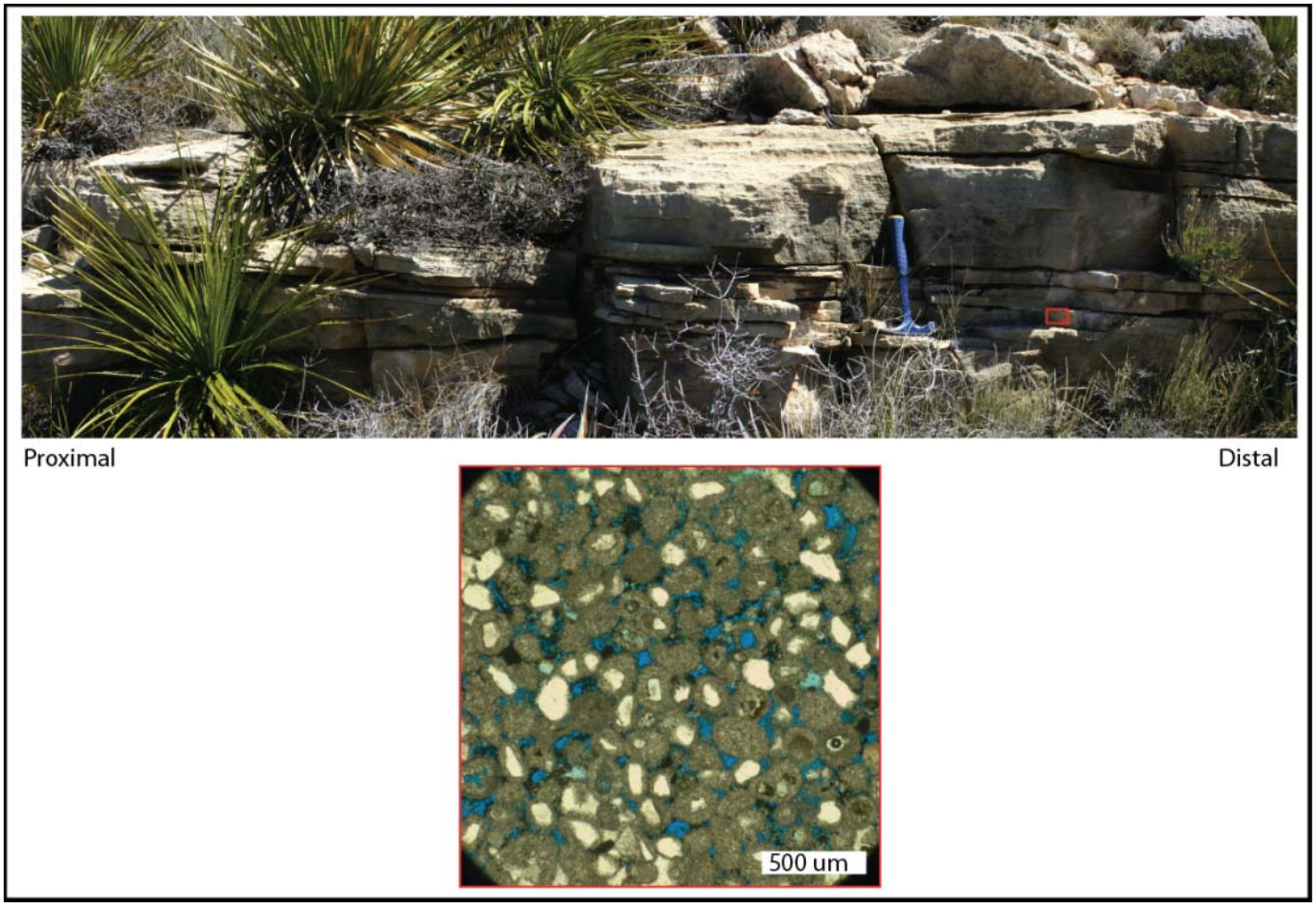

Figure 15: Top) Outcrop photograph of shingled, seaward-dipping ooid grainstone indicative of a foreshore environment and typical of the high energy shelf crest facies tract. Hammer for scale ~30 cm. Bottom) Photomicrograph of the ooid grainstone (with common quartz sand ooid nuclei) from outcrop sample marked with the red box. Photo and sample taken from Section B, cycle 26.1, (#B-6).

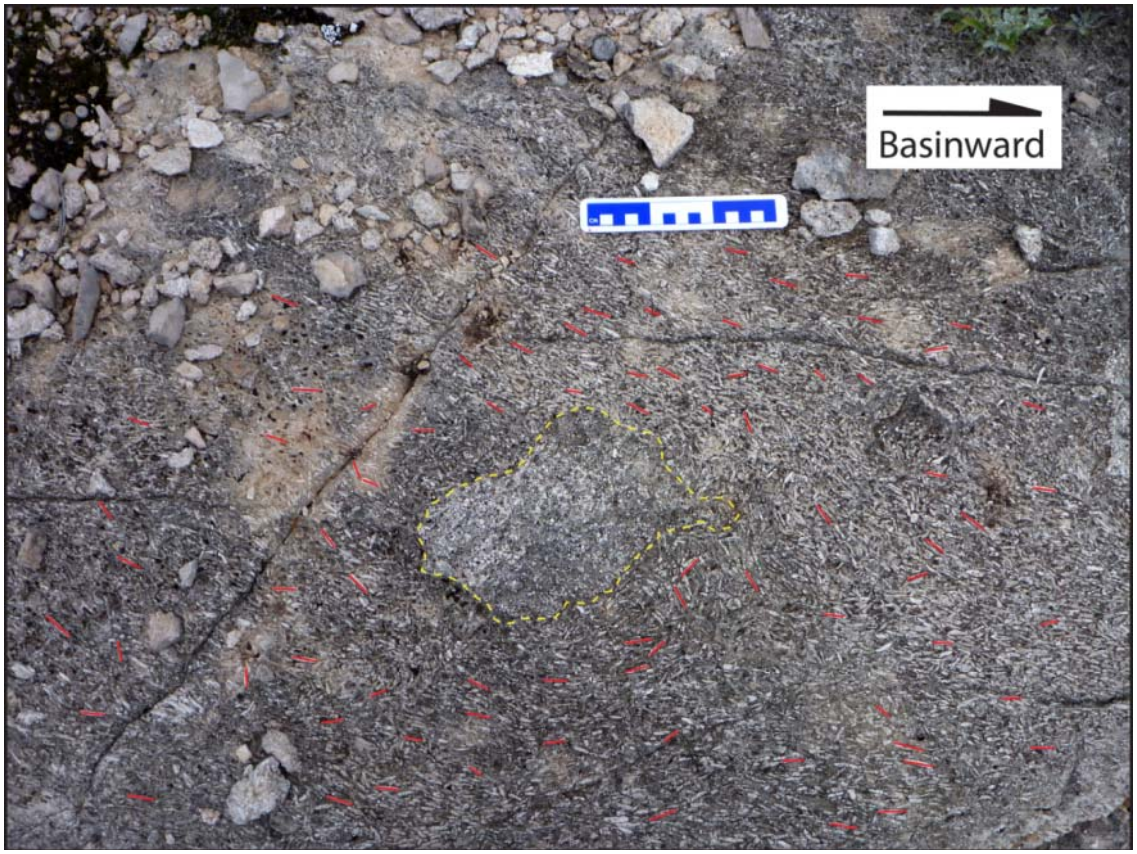

Figure 16: Bedding plane-perpendicular outcrop photograph of a fusulinid grainstone/rudstone exhibiting aligned *Polydiexodina* fusulinids oriented in a long axis-basinward direction (small red lines). Additionally there is a ~15 cm patch of vertically aligned fusulinids (outlined with yellow dashes), formed either as an intraclast or as an edgewise coquina in the foreshore/swash zone of the high energy shelf crest facies tract. Note how the orientation of the fusulinids changes around the edgewise patch, indicating penecontemporaneous hydrodynamic control over their positions. Photo taken near Section I within cycle 24.1. Scale in centimeters.

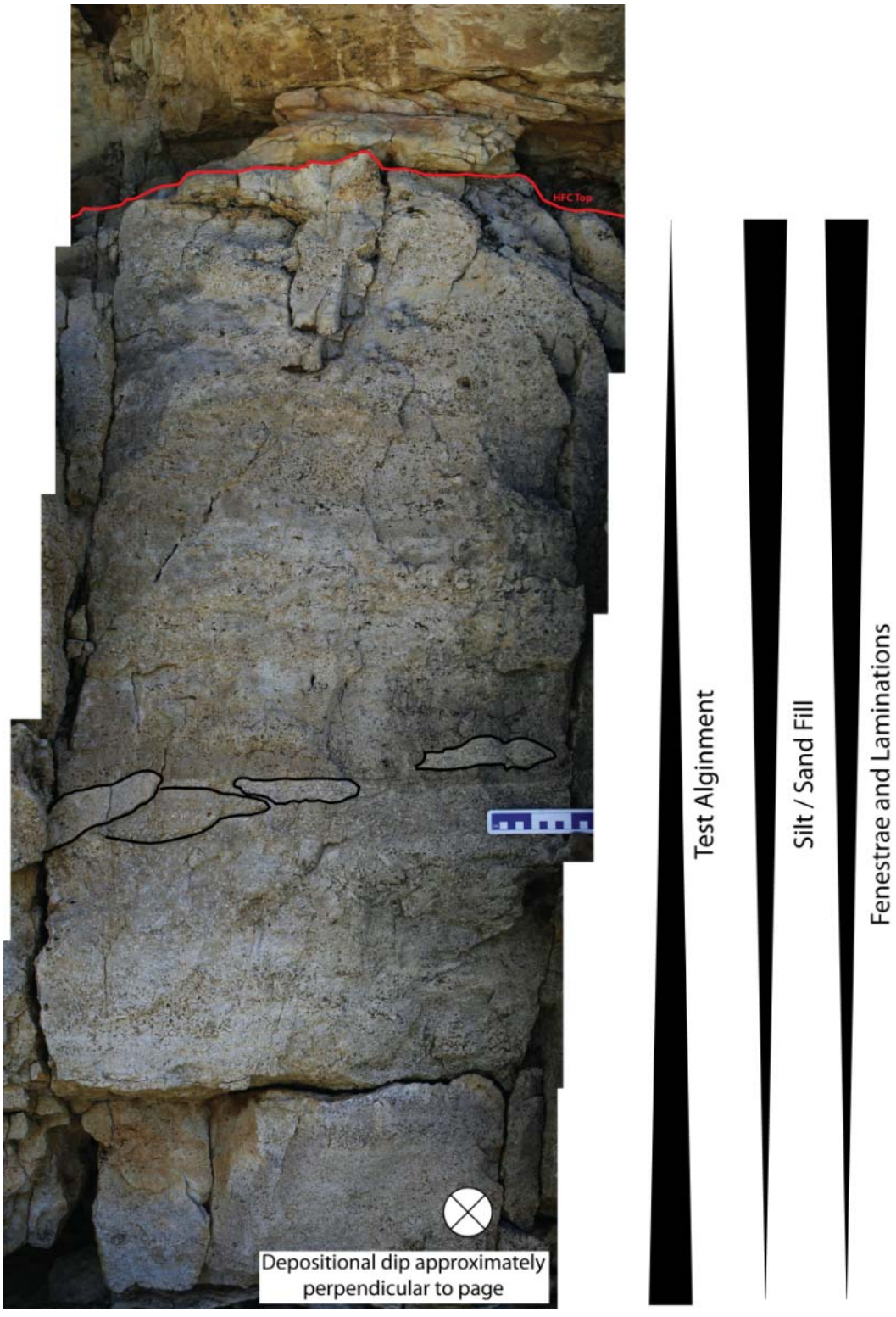
HFC Top
Depositional dip approximately perpendicular to page
Test Alginment
Silt / Sand Fill
Fenestrae and Laminations

Figure 17: Vertical outcrop photograph of the transition from high energy intertidal/subtidal aligned-test ooid-fusulinid rudstone (at base) through intertidal fusulinid rudstone with intraclasts (black outlines) and capped by fenestral fusulinid rudstone with pore-filling sand and laminated crusts. Photo taken along Section B in cycle 25.1. Scale in centimeters.

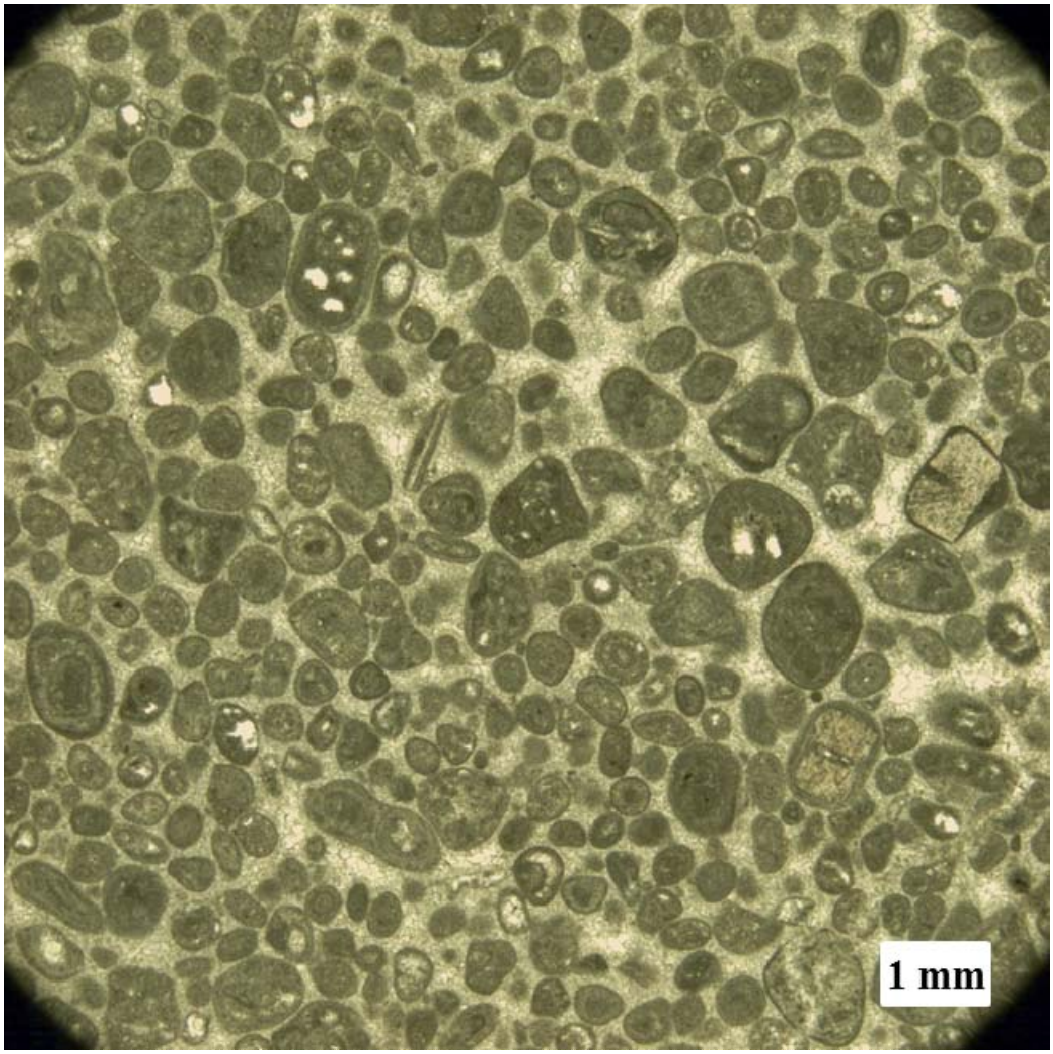

Figure 18: Photomicrograph of the ooid grainstone facies with common composite grains and superficial ooids after skeletal fragments (crinoids, forams) typical of the high energy shelf crest facies tract. Faint cross lamination (grain sorting) is also visible. This facies contains bladed rim cement and pore-filling blocky spar. Sample from Section A (#A-2) from cycle 26.2.

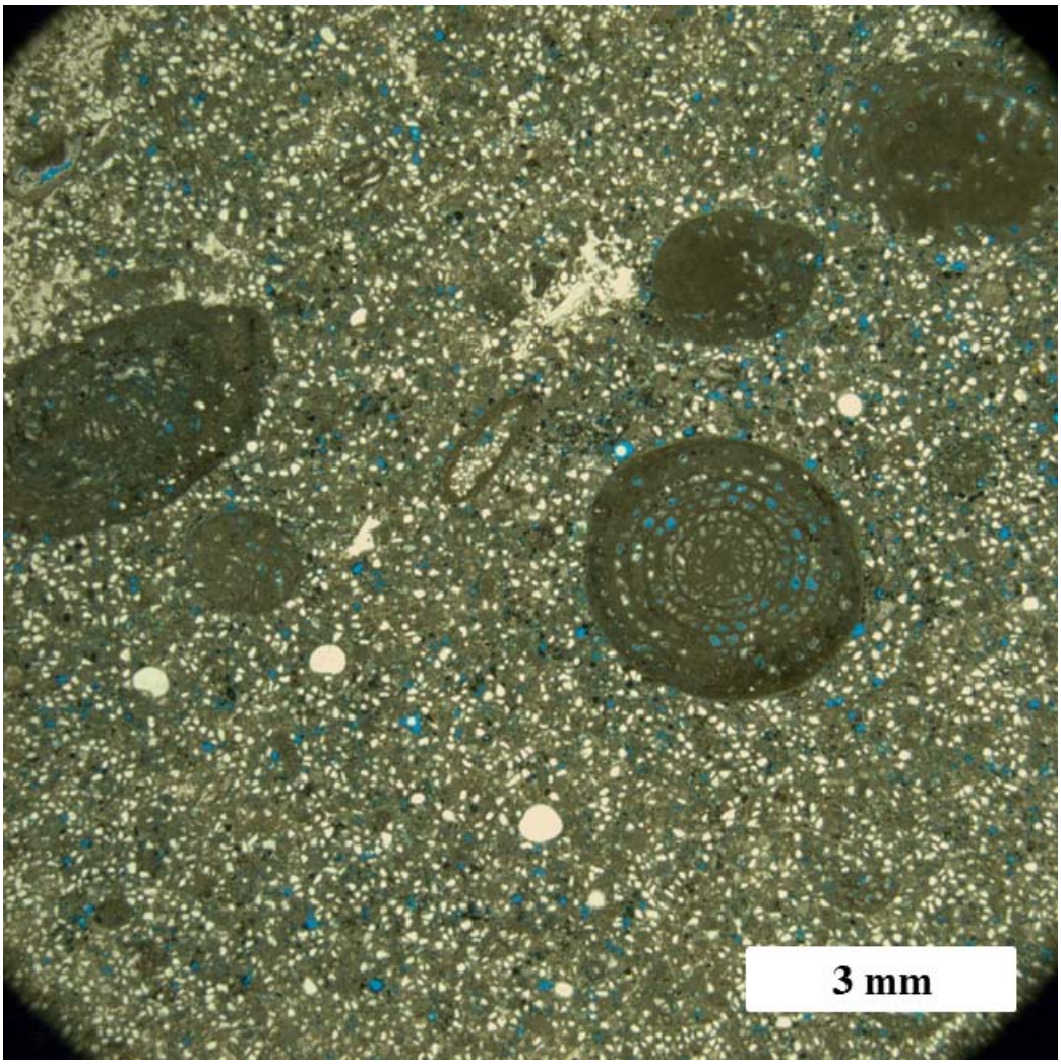

Figure 19: Photomicrograph of dolomitic siltstone to sandstone with an abundance of siliciclastic-cored ooids, fusulinids, and very well rounded medium grain size quartz grains. Note the bimodal grain size distribution of siliciclastic grains, indicating aeolian transport. This facies is characteristic of the siliciclastics within the high energy outer shelf facies tract. Sample from Measured Section D (#D-7) from cycle 25.4.

Figure 20: Outcrop photograph of multidirectional and planar cross stratified skeletal-ooid grainstone typical of the high energy outer shelf facies tract. Photo taken along Section E in cycle 23.7; hammer for scale is ~30 cm.

Figure 21: Outcrop bedding plane photograph of a skeletal-*Mizzia*-fusulinid rudstone typical of the high energy outer shelf facies tract. Note that the fusulinid tests are not aligned when compared to those in Figure 13. Photo taken distal to (south) of Section B in the G25 HFS. Scale in centimeters.

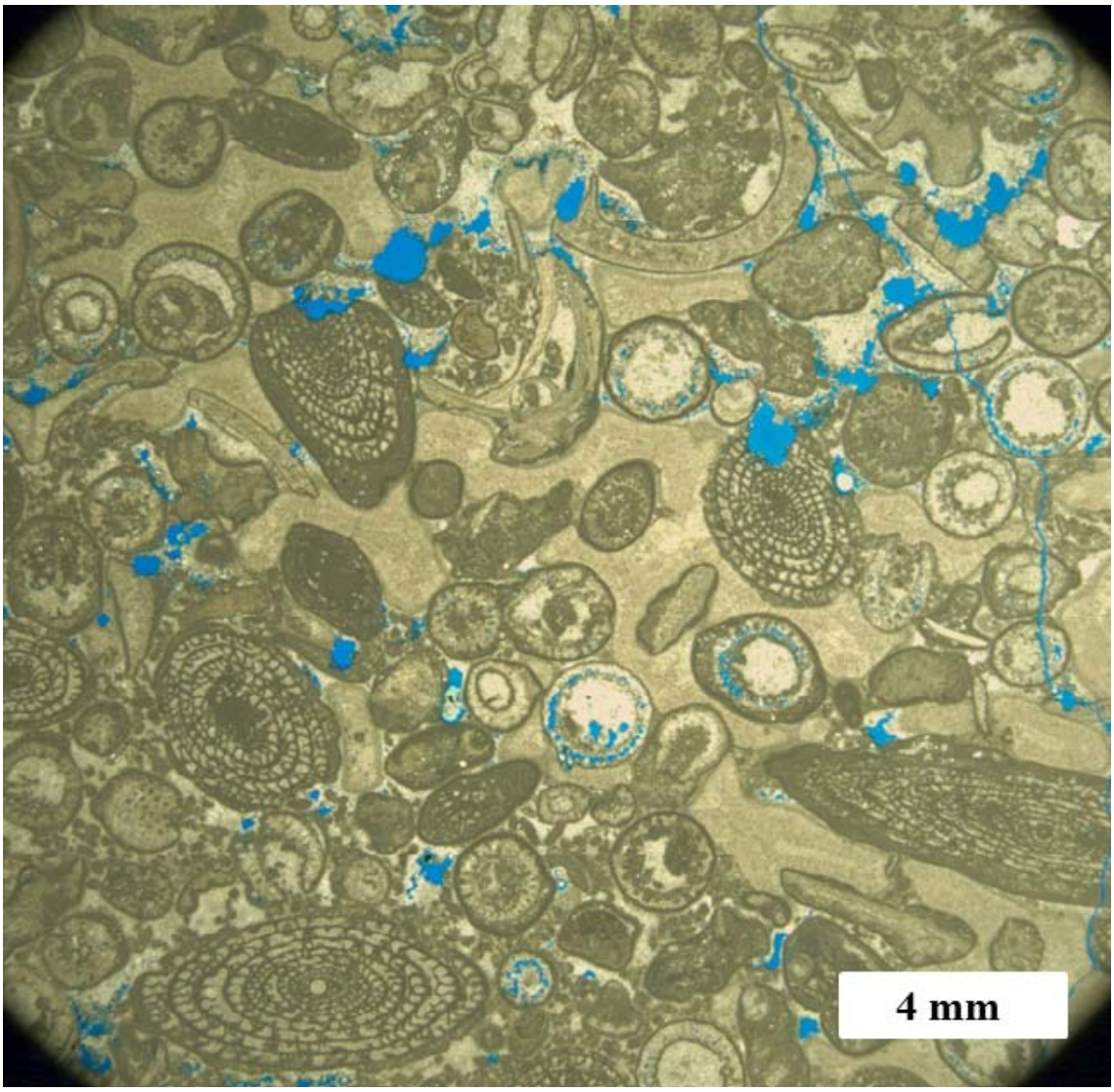

Figure 22: Photomicrograph of skeletal-*Mizzia*-fusulinid grainstone/rudstone typical of the high energy outer shelf facies tract. Note the presence of thin meniscus cements overlain by thick, isopachous radiaxial fibrous cement. Sample from Section B (#B-3) from cycle 24.7.

Moderate to Low Energy Shelf Crest

The moderate to low energy outer shelf facies tract is distal to the high energy outer shelf and proximal to the shelf margin (Figure 11). It is composed of four facies: skeletal-peloid-oncoid grain-dominated packstone/rudstone, oncoid-foram-peloid mud-dominated packstone, foram-peloid wackestone, and rare dolomitic siltstone-to-sandstone. As previously noted, the observed siliciclastics are thin (<1m) and occur only at cycle bases, with a considerably higher percentage of carbonate allochems than in the previously described updip facies tracts. The carbonate facies show a greater mud content but are largely still grain-supported, cycle tops are picked largely on the basis of fabric, although amalgamation is common (Tinker, 1996, 1998; Osleger, 1998). The packstones are characterized by 1-3 meter thick, seaward-dipping beds while the wackestone is commonly massive. Peloids, oncoids, small forams, bivalves, gastropods, and crinoid fragments are common throughout these facies. The distinctive oncoid-rich facies also exhibit extensive micritization and a clotted texture (Figure 23). The foram-peloid wackestone is the muddiest facies and typically occurs in the middle of cycles within the late TST/early HST of HFS's. All of these facies are generally gradational. The outer shelf grades distally into the shelf margin facies tract, transitioning from grain-dominated, ooid, *Mizzia,* and fusulinid-rich grainstones and rudstones to mud-dominated, peloid, skeletal, and oncoid-rich packstones with faint bedding. No evidence for positive depositional relief of the margin such as landward-dipping margin facies debris was observed (Tinker, 1996, 1998; Kerans and Tinker, 1999).

The moderate-to-low energy outer shelf represents subtidal carbonate deposition distal to the shoals of the high energy outer shelf (Tinker, 1998). The relative increase in muddy fabrics and decrease in stratification indicates lower depositional energy than the high energy outer shelf; below fair weather wave base. The presence of packstone fabrics

and fragmented skeletal allochems do indicate some winnowing and depostional energy characteristic of deposition above storm wave base. The additional increase of mud content in a basinward direction indicates that energy decreased and bathymetry increased with proximity to the margin, as in the "marginal mound" of Dunham (1972), Kerans and Harris (1993), Tinker (1996, 1998), and Osleger (1998).

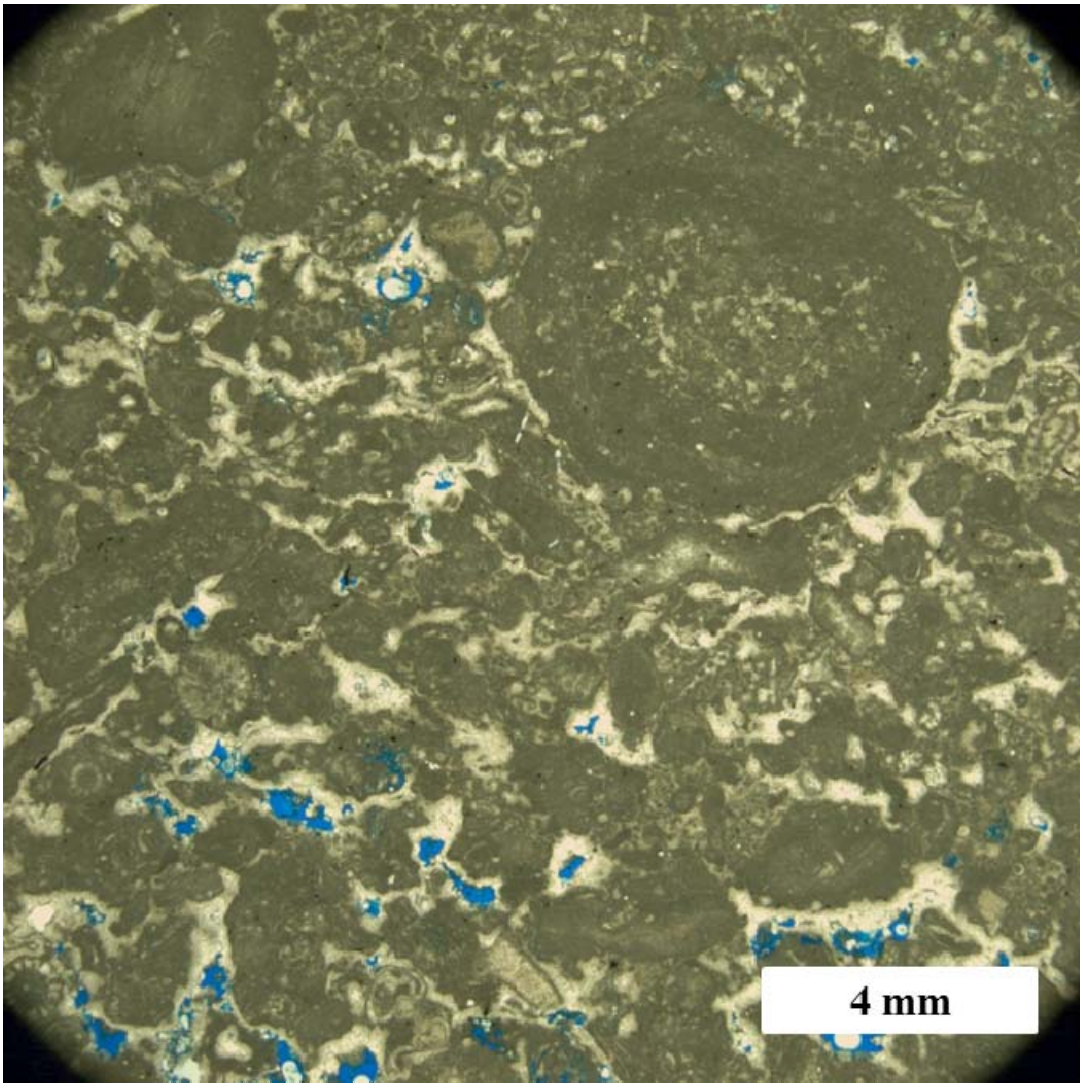

Figure 23: Photomicrograph of the skeletal-peloid-oncoid grain-dominated packstone/rudstone typical of the moderate to low energy outer shelf facies tract. Note the micritic, clotted texture of the oncoid and surrounding grains. Sample from Measured Section B (B-1) in cycle 24.5.

Shelf Margin

The shelf margin facies tract (Capitan Reef/Massive) is characterized by two facies: crinoid-*Collenella* grain-dominated packstone and sponge-algal boundstone. The crinoid-*Collenella* grain-dominated packstone is gradational with the Moderate-to-Low Energy Outer Shelf facies and contains a diverse fauna including *Collenella*, crinoid fragments, bivalves, gastropods, and bryozoans. This facies is typically dominated by limestone, but exhibits small amounts of siliciclastics, dolomite, and faint brecciation near HFS boundaries (Kerans and Harris, 1993; Tinker, 1996, 1998). The sponge-algal boundstone is the volumetrically dominant facies of the Shelf Margin, but it represents a far greater vertical extent than dip width. It is largely composed of sponges, *Tubiphytes*, *Archaeolithoporella*, marine cement, and internal sediment. Both of the shelf margin facies are massively bedded, creating cliffs 10's of meters high. Siliciclastic and carbonate-filled syndepositional faults and fractures (often referred to as neptunian dikes) occur within this facies tract. The source of the fill material is largely derived from the outer shelf (Kerans and Harris, 1993; Hunt et al., 2002; Kosa et al., 2003; Stanton and Pray, 2005; Kosa and Hunt, 2005, 2006a, 2006b), which suggests these features were open to the seafloor during deposition. These deformation features tend to be focused in close proximity (within ~100m) to the location of high-frequency sequence and composite sequence bounding margins. The sediment fill is generally more carbonate-dominated near the younger margins (Kosa and Hunt, 2006a).

The Shelf Margin facies represent subtidal deposition along a high-relief, basin-rimming margin which was supported by a fabric of encrustation, binding, sponge-framework, and early marine cementation. During the G23-G26 the margin was likely at or close to fair weather wave base, progressively shallowing with proximity to the G25-

G26 CS boundary (Babcock and Yurewicz, 1989; Kerans and Harris, 1993; Wood et al., 1994; Tinker, 1996, 1998; Kerans and Tinker, 1999).

Upper Slope

The upper slope facies tract is exposed at the southeastern end of Slaughter Canyon, showing only deposits equivalent to the G25 and younger shelf sequences. This facies tract is characterized by two facies, only one of which is present in Slaughter Canyon: (1) intraclast-skeletal grain-dominated packstone-to-rudstone, and (2) siliciclastic slope facies (which are either covered or below the base of the canyon). The intraclast-skeletal grain-dominated packstone-to-rudstone contains a diverse mixture of shelf-derived allochems, primarily skeletal fragments, clasts of reef material, and peloids. Graded bedding, internal cavity fill and soft sediment deformation are common in the steeply basinward-dipping beds (>30 degrees). The youngest of these facies (possibly G28-equivalent) are chaotically bedded with a backfilling, lower-angle geometry (as observed elsewhere by Playton, 2008).

This facies represents an upper slope environment with evidence for rock fall, grain flow, and debris flows distal to the shelf margin (Brown and Loucks, 1993; Mruk and Bebout, 1993; Melim and Scholle, 1995; Tinker, 1998). The G25 to G27 equivalent facies appear to be generally finer grained with more bedding organization, while the younger, coarser and more chaotic upper slope may represent a transition in forereef/upper slope architecture from accretionary to bypass (Figure 24).

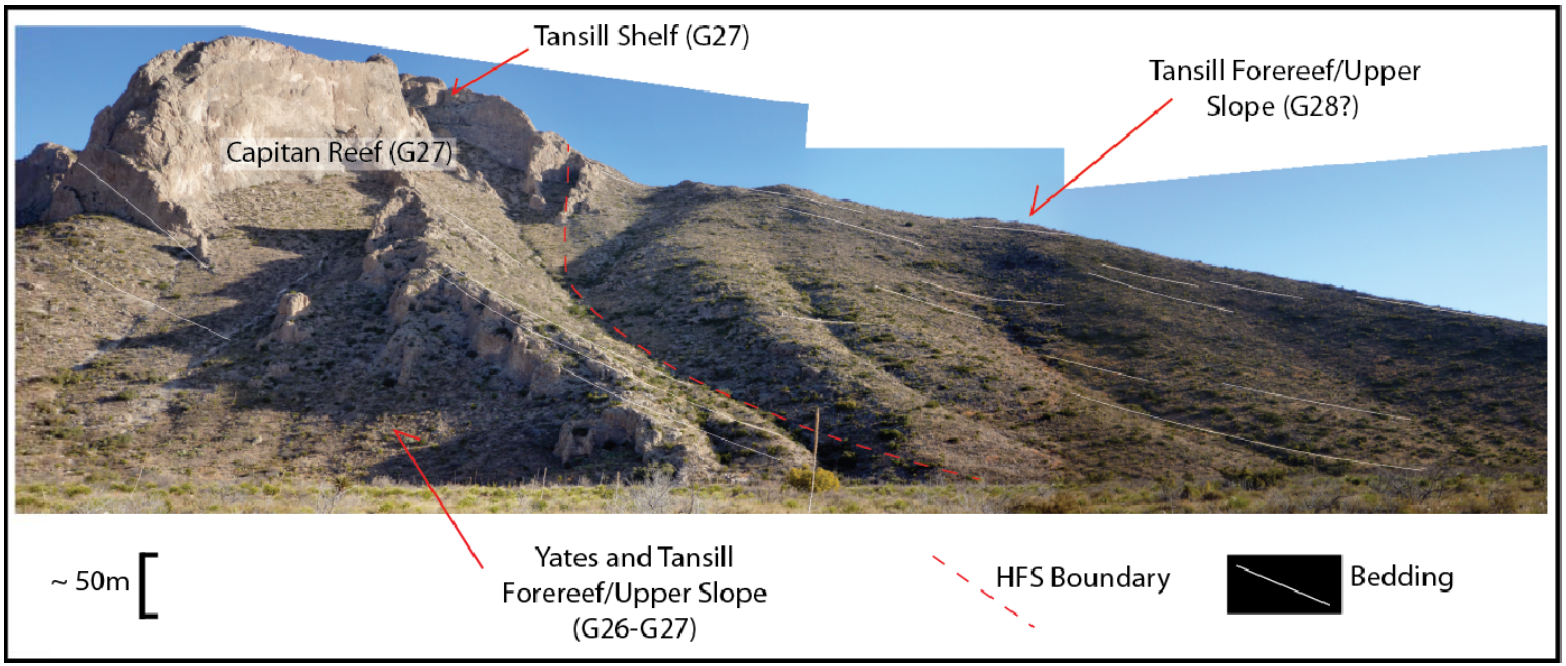

Figure 24: Photomosaic of the southeastern mouth of Slaughter Canyon showing the massive Capitan shelf margin facies (upper left), steeply basinward-dipping forereef to upper slope facies (>30 degrees) equivalent to G26-G27 shelf deposition. Note the lower angle and more chaotic bedding of forereef/upper slope facies above the hypothesized G27/G28 boundary, indicating a transition from an accretionary to bypass slope. Scale is approximate as there is evident photographic distortion (the perspective condenses the top of the outcrop relative to the base).

SEQUENCE EVOLUTION

The facies within the facies tracts of the Yates-Capitan depositional system show hierarchical cyclic stacking patterns, the fundamental unit of which is the high frequency cycle (HFC) (*eg.*, Kerans and Fitchen, 1995). These cycles can be correlated from proximal (middle shelf) to distal (shelf margin) facies tracts; through these transitions the constituent facies change (Neese and Schwartz, 1977; Kerans and Fitchen, 1995; Tinker, 1996, 1998; Osleger, 1998). Intra-cycle lateral facies changes occur due to depositional energy controlled by position relative to the shelf margin and by relative restriction behind the shelf crest; thereby creating a fining-upwards facies succession in the middle shelf and coarsening-upwards facies succession in the outer shelf. Cycle amalgamation is also common where changes in accommodation are insufficient to cause facies change. Amalgamation is common in the middle shelf, low to moderate energy shelf crest, moderate to low energy outer shelf, and shelf margin where a cycle can be represented by two or even one facies. Consequently, the bathymetric region containing the high energy shelf crest and high energy outer shelf sediments best captures high frequency cyclicity, as it is common for a single cycle to contain a subtidal to intertidal vertical facies succession, filling all the available space. It is also common for the facies of two facies tracts to overlap in a cycle within the same vertical position. The dolomitic siltstone to sandstone facies is the most common cycle base, occurring across multiple facies tracts and showing subtle differentiation depending on its dip position on the shelf.

The character of a HFC also changes depending on its relation to lower-order accommodation trends (Kerans and Fitchen, 1995; Tinker, 1996, 1998; Osleger, 1998). Within each described high frequency sequence (HFS), the constituent facies of a cycle generally partition according to that cycle's position in the overall HFS and composite sequence (CS); such that cycles near a dual HFS and CS maximum flooding surface have

a higher percentage of low energy outer shelf facies while cycles within a dual HFS and CS highstand have a higher percentage of shelf crest facies (Tinker, 1996, 1998) (Figures 25, 26, 27).

The sequence framework used in this study (Kerans and Tinker, 1999), is built from the hierarchical bundling of HFC's into cycle sets, cycle sets into HFS's, and HFS's into CS's (Kerans et al., 1992, Kerans and Fitchen, 1995; Tinker, 1996, 1998). The HFC's show the dominant scale of variability documented in the study area. Cycle amalgamation occasionally causes an apparent single updip or downdip cycle to be equivalent to two or even three shallowing-upward successions where facies contrast is more distinct. The following section describes the development of each HFS with respect to cycle-scale vertical stacking patterns, lateral facies associations, facies proportions, cycle-capping facies, and syndepositional growth on faults. Descriptions are based on measured sections, field mapping, lidar mapping, and reconstruction of each HFS using the projected lidar data. Reconstruction involved aligning the upper datum (top sequence boundary) for each HFS to remove younger fault offset. Plates I and II show updip and downdip interpreted outcrop photomosaics, Plate III shows the reconstructed cross section, and Plate IV shows the *in situ* cross section. The description of fault fill and morphology is highly simplified in the study area as the focus of this study was primarily the stratigraphy around them. Detailed descriptions of most of the fault fill, morphology, and timing in the area can be found in Hunt et al. (2002), Kosa et al. (2003); Hunt et al. (2005), and Kosa and Hunt (2005, 2006a, 2006b).

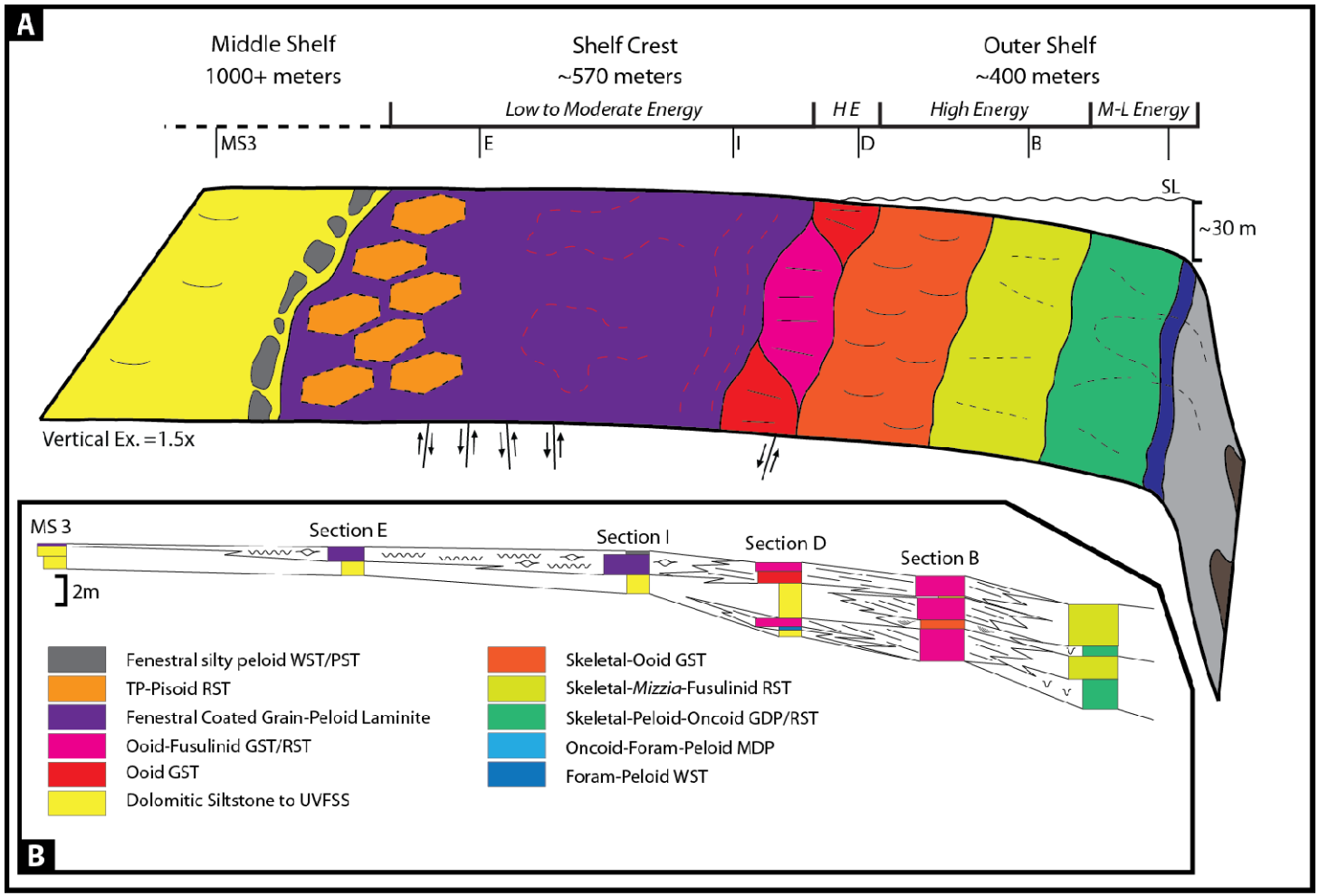

Figure 25: A) Depositional model representative of a transgressive cycle in the G25 HFS; note the width of the general facies tracts and the proximity of the siliciclastic middle shelf. B) Cross section of cycle 25.1 illustrating the variation in cycle character along dip, with significant amalgamation proximally. MS 3 adopted from Hunt et al. 2002.

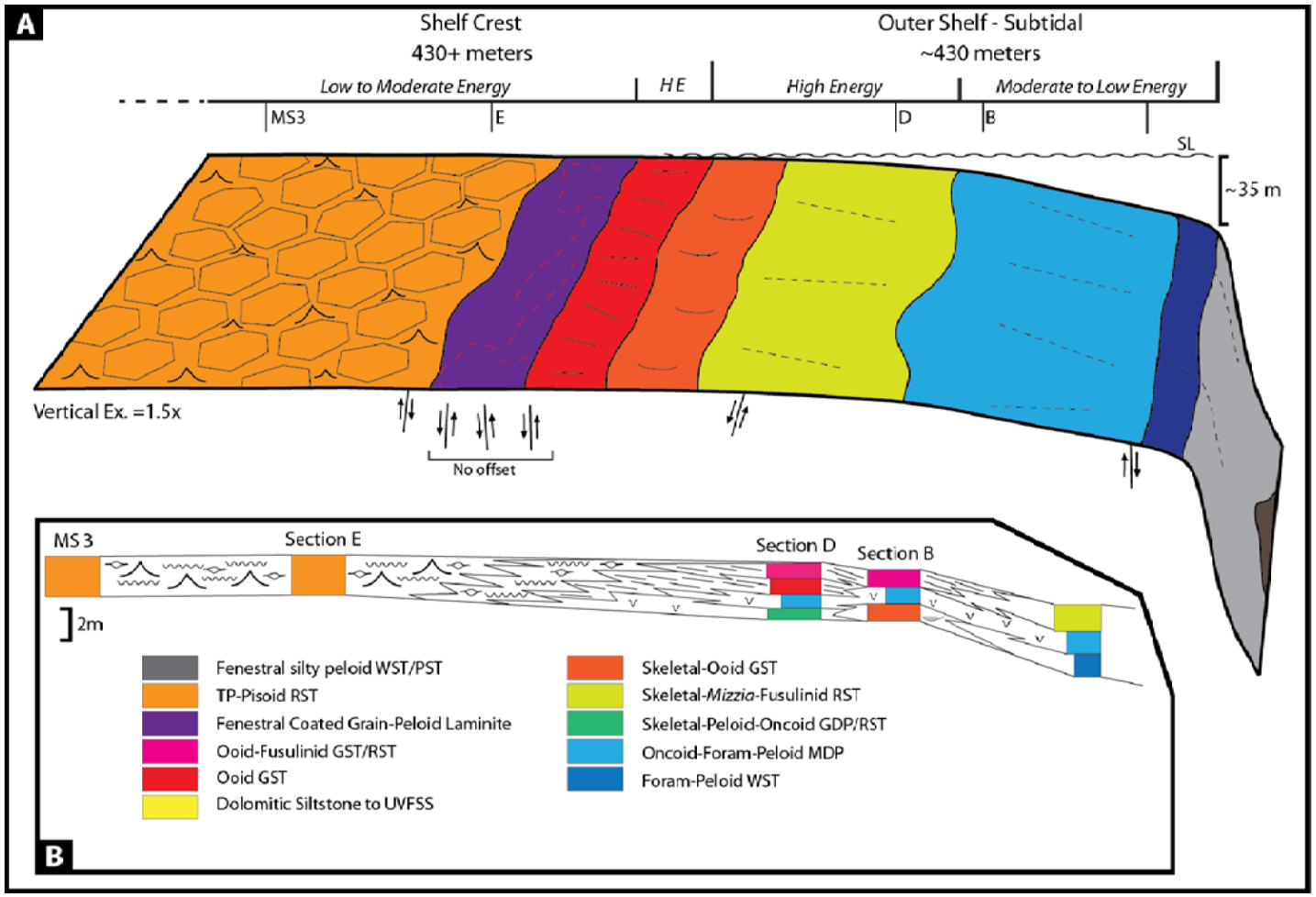

Figure 26: A) Depositional model representative of a cycle containing the G25 MFS; note the greater width of the outer shelf and the loss of the middle shelf (in the study area). B) Cross section of cycle 25.5 illustrating the variation in cycle character along dip, with significant amalgamation proximally and symmetric cycle development in Section B. MS 3 adopted from Hunt et al. 2002.

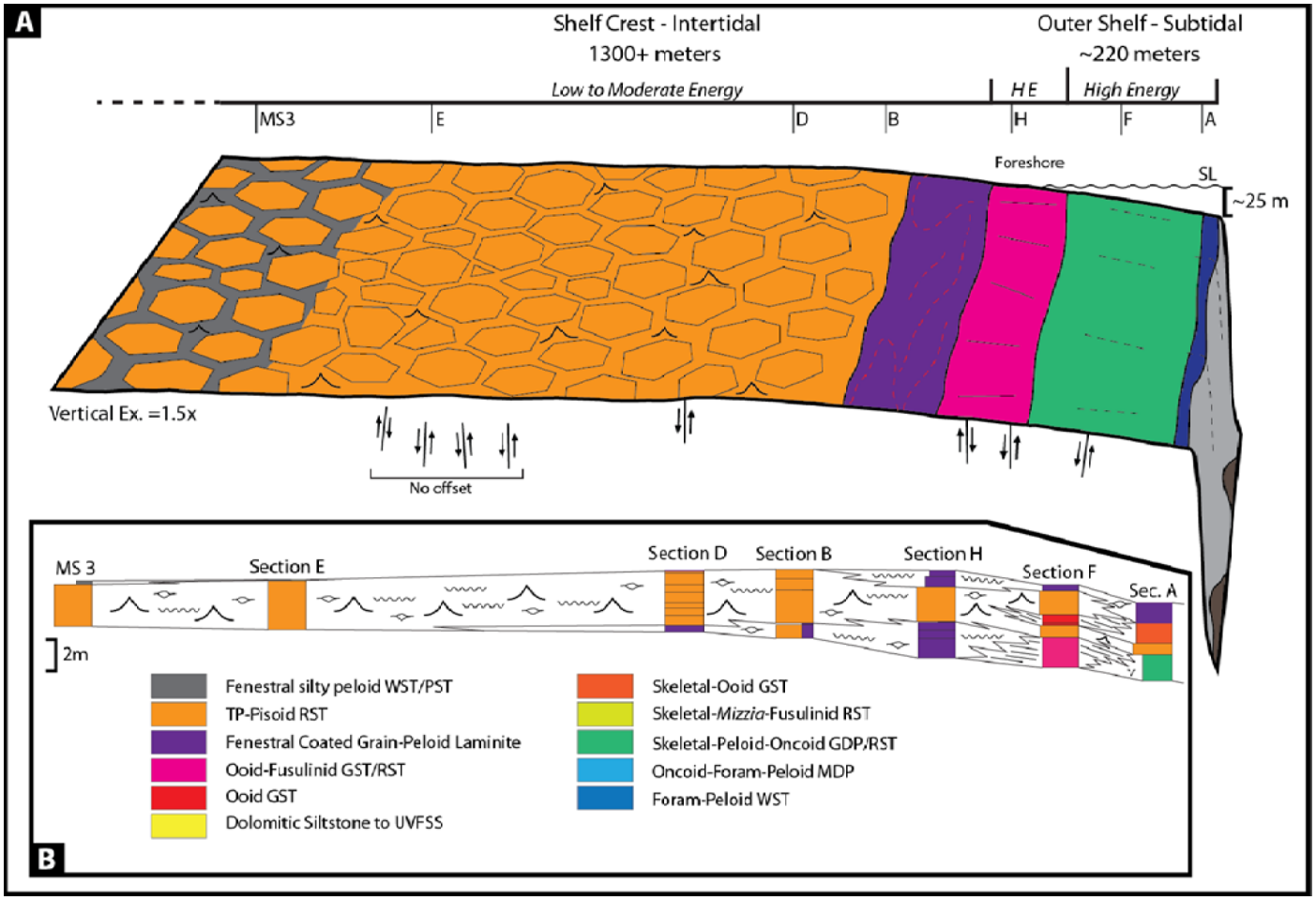

Figure 27: A) Depositional model representative of a highstand cycle from the G25 HFS; note the greater width of the shelf crest and the reduced width of the outer shelf. B) Cross section of cycle 25.13 illustrating the variation in cycle character along dip, with significant amalgamation proximally in the tepee-pisoid rudstone complex of the shelf crest. MS 3 adopted from Hunt et al. 2002.

G23

The G23 HFS is partially exposed within the study area, such that the observed cycles are characterized by facies deposited seaward of the low to moderate energy shelf crest. Previous studies show that the cycles within this sequence are dominated by progressively shallower facies updip (Osleger, 1998; Hunt et al., 2002). This HFS is composed of 13 HFCs, which show dominantly asymmetric, shallowing-upward facies stacking patterns (Figures 28, 29). Cycles 23.1 and 23.3 exhibit dolomitic siltstone-to-sandstone facies at their bases, with cycle 23.1 shallowing immediately to foreshore ooid-fusulinid grainstone and cycle 23.3 shallowing more gradually through outer shelf facies to foreshore ooid grainstones. Cycles 23.2 and 23.4 are entirely composed of shallowing-upward outer shelf facies in the study area. Cycles 23.5 and 23.6 are thicker than those below but show significant progradation with amalgamated foreshore ooid-fusulinid grainstone/rudstone and ooid grainstone caps, grading to skeletal rudstones and packstones at the margin. The base of cycle 23.7 shows considerable transgressive facies offset of moderate to low energy outer shelf oncoid-foram-peloid mud-dominated packstone on high energy shelf crest ooid-fusulinid grainstone/rudstone. Cycles 23.7 and 23.8 shallow to skeletal-ooid grainstone and ooid-fusulinid grainstone/rudstone respectively indicating an overall progradational trend; expressed distally as an upward-gradation from oncoid-foram-peloid mud-dominated packstone to skeletal-*Mizzia*-fusulinid rudstone. Significant transgressive offset is again recorded at the base of cycle 23.9, which shallows only to high energy outer shelf rudstone; however, the overlying cycles progressively shallow and prograde with increasing proportions of high energy shelf crest facies capping cycles and approaching the margin. The only low to moderate energy shelf crest facies occur immediately below the G23/G24 sequence boundary, and represent significant progradation at the top of the HFS. There is no evidence for

karstification at the top of the G23, although there is a sharp contact and significant facies tract offset of middle shelf-derived siliciclastics over low to moderate energy shelf crest facies.

The shelf margin was highly progradational (471 m) and moderately aggradational (29 m) during the G23 HFS. Although there is adequate outcrop to pinpoint the lower and upper sequence bounding surfaces at the margin, poor outcrop is common at the likely position of the margin in between, preventing cycle-scale evaluation of the shelf margin evolution.

Outcrop quality and lack of facies contrast impedes the ability to measure growth on the three (possibly four) faults which visibly intersect the distal portion of the G23 HFS within the study area, although they contain some siliciclastic fill; possibly indicating infiltration during exposure (Kosa and Hunt, 2006a).

Determination of a maximum flooding surface for the G23 is difficult with the available data which covers only the most basinward section of the HFS. Stacking pattern analysis points towards the lower portions of cycles 23.4, 23.7, and 23.9 as candidate MFS given the transgressive offset of moderate to low energy outer shelf facies within each. However, the cycle-capping facies of 23.4 suggest that it contains the best candidate for an MFS, as this cycle shallows only to skeletal-peloid-oncoid grain-dominated packstone (moderate to low energy outer shelf), rather than skeletal-*Mizzia*-fusulinid rudstone (high energy outer shelf).

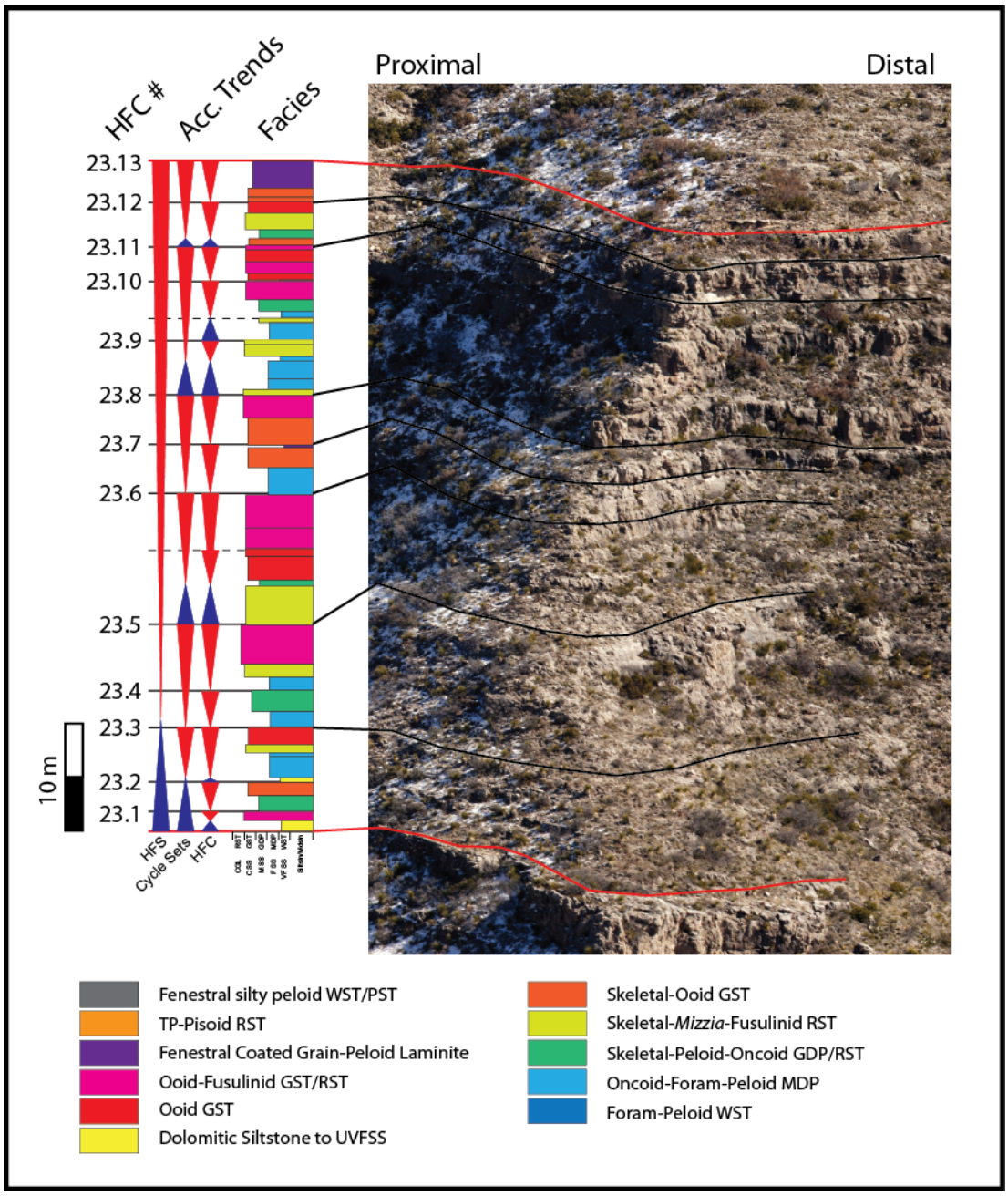

Figure 28: Measured Section E covering the G23 HFS and referenced to its approximate outcrop location. Cycle, cycle set, and HFS accommodation trends indicated. WST = wackestone; MDP = mud-dominated packstone; GDP = grain-dominated packstone; GST = grainstone; RST = rudstone; UVFSS = upper very fine sandstone. Photograph window from Plate I.

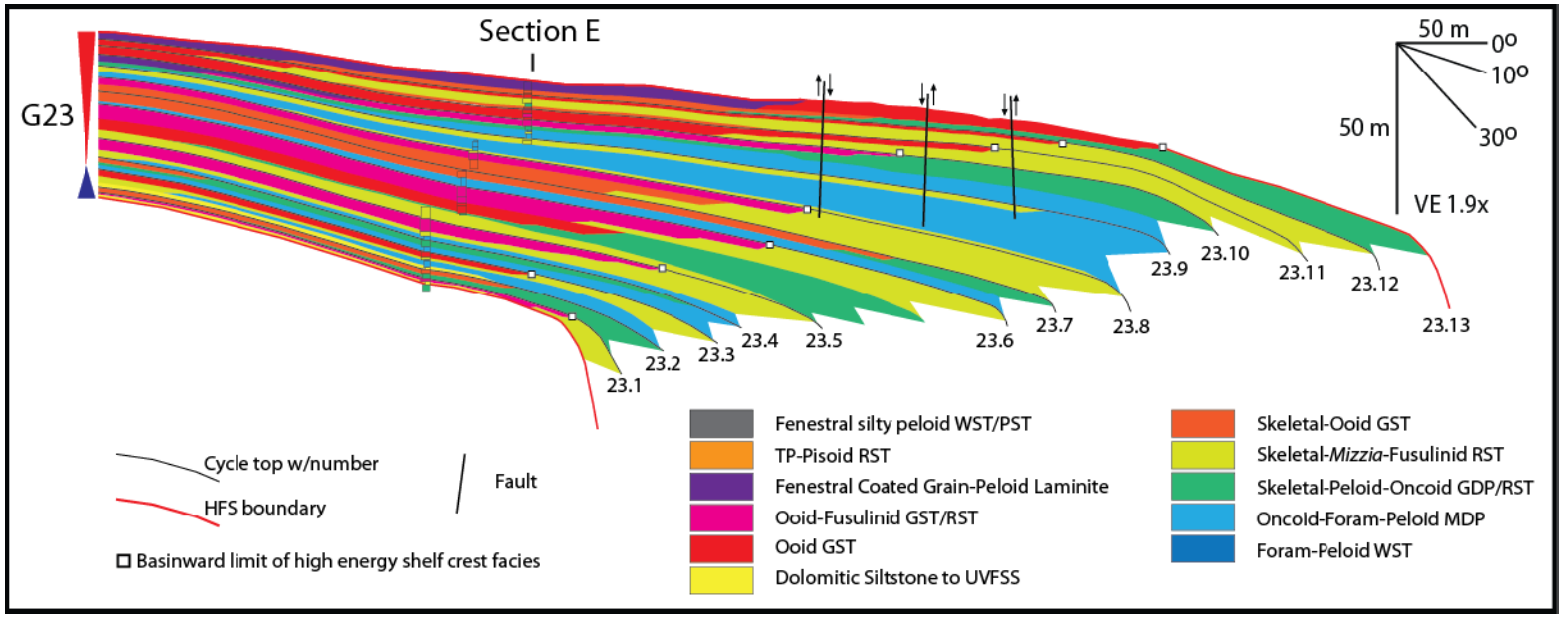

Figure 29: Reconstructed lidar-projected cross section showing the cycle-scale distribution of facies within the G23 HFS. The location of Measured Section E is noted for reference to Figure 23. Solid black lines show the location of faults whose lower tips were obscured by covered outcrop and likely extend into the underlying shelf margin. HFS-scale accommodation triangles for the G23 are shown at the left; their shared apex represents the location of the maximum flooding surface. See Plate # for a more detailed version of this figure.

G24

The G24 HFS outcrops across the study area with facies from the shelf crest to the shelf margin. Most of the 12 cycles contained within this HFS grade updip into the low to moderate energy shelf crest and downdip into the moderate to low energy outer shelf (Figures 30, 31). Cycle 24.1 amalgamates updip into dolomitic siltstone-to-sandstone basinward of the faults of the Walnut Canyon Syncline (F, G, H, and I of Kosa and Hunt, 2006a). Cycles 24.8 and 24.11 amalgamate downdip into outer shelf rudstones and packstones. Cycles 24.1 and 24.2 both contain basal dolomitic siltstone-to-sandstone facies proximally, thinning and grading into outer shelf grain-dominated packstone and rudstone distally; both also shallow to ooid-fusulinid grainstone/rudstone shelf crest foreshore facies. Cycle 24.2 transgresses further proximally than 24.1 (which amalgamates into siliciclastics), where it is characterized by fenestral laminites of the low to moderate energy shelf crest. Cycles 24.3 and 24.4 show a generally aggradational stacking pattern with an amalgamated ooid-fusulinid grainstone/rudstone foreshore complex in the center of the profile (Section I) that expanded landward in the 24.4 cycle as well as developing a skeletal-ooid grainstone shoal distally. Cycles 24.5 to 24.7 are characterized by an incursion of moderate to low energy outer shelf packstones above the older foreshore, causing the dip width of the high energy shelf crest to decrease; interestingly, these cycles were still capped by high energy shelf crest and outer shelf facies almost to the margin. Cycles 24.8 to 24.13 are characterized by renewed progradation of the shelf crest, with those facies capping each cycle with generally increasing percentages. Distally, progradation of high energy outer shelf rudstones is additionally apparent.

The shelf margin was significantly less aggradational during the G24 than the G23 (15 m vs. 29 m), and it appears that the only periods of aggradation occurred from

cycles 24.1 to 24.4 and 24.6 to 24.7 while progradation was dominant in 24.5 and 24.8 to 24.13.

Growth faulting occurred in two areas within the studied G24 HFS. A relatively small amount of growth (maximum cycle offset of 3.2 m) developed on the down-thrown sides of faults within the Walnut Canyon Syncline (Figure 26), which healed (no offset) by cycle 24.5 (faults F, G, H, and I of Kosa and Hunt, 2006a). Significantly more growth occurred in the fault above the lower sequence margin (margin of surface 24.0); here a maximum fault throw of 11 m (on proximal, down-thrown side) was observed, which was not healed until cycle 24.11 (fault J of Kosa and Hunt, 2006a). This growth was accommodated more by the lower cycles than by the upper ones.

The maximum flooding surface of the G24 HFS is placed in the lower portion of cycle 24.6, indicated by the maximum landward extent of subtidal (moderate energy) outer shelf facies. The upper sequence boundary was characterized again by significant facies tract offset of siliciclastics sharply overlying the shelf crest to outer shelf facies of cycle 24.13. The only documented evidence of karst was located along the growth fault above the terminal G23 margin; here previous authors have documented paleocavern development and mixed carbonate-siliciclastic fill (Kosa and Hunt, 2006a).

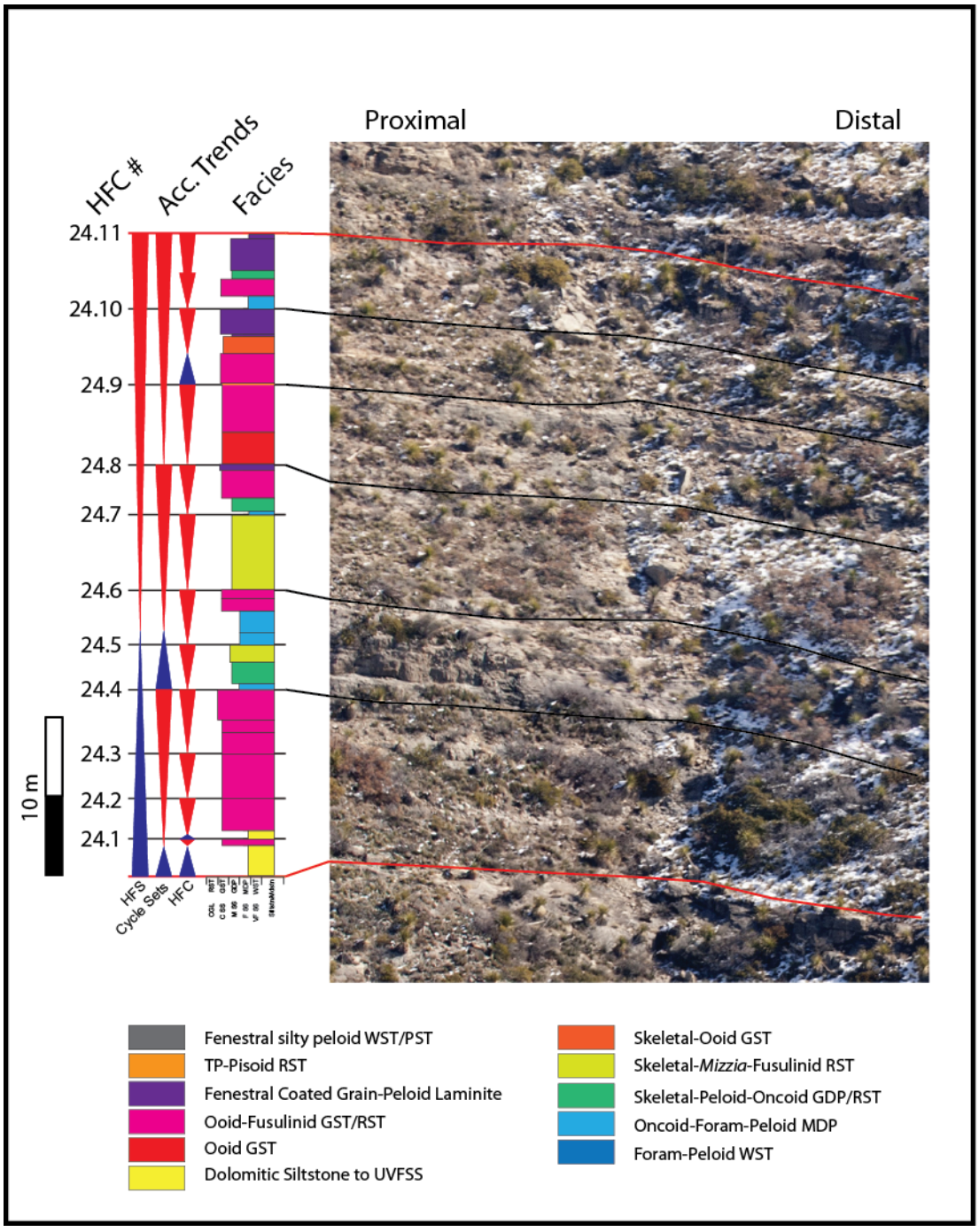

Figure 30: Measured Section I covering the G24 HFS and referenced to its approximate outcrop location. Cycle, cycle set, and HFS accommodation trends indicated. Abbreviations identical to those in Figure 23. Photograph from Plate I.

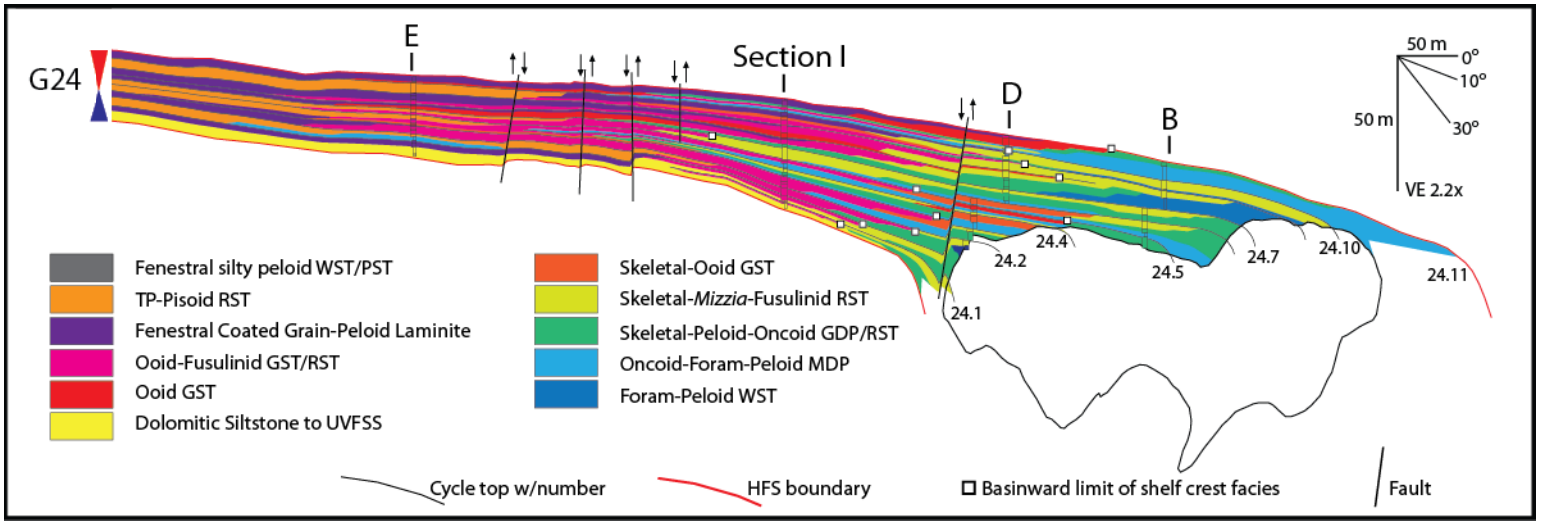

Figure 31: Reconstructed lidar-projected cross section showing the cycle-scale distribution of facies within the G24 HFS. The location of Measured Section I is noted for reference to Figure 22. Solid black lines show the location of faults. HFS-scale accommodation triangles for the G24 are shown at the left; their shared apex represents the location of the maximum flooding surface. See Plate # for a more detailed version of this figure.

G25

The G25 HFS is characterized by 14 HFC's which contain middle shelf to shelf margin facies within the study area (Figures 32, 33). There is significant proximal cycle amalgamation as cycles 25.1 and 25.3 grade into siliciclastics and cycles 25.7 to 25.13 grade into a thick stack of tepee-pisoid rudstone. Cycles 25.1 and 25.2 both exhibit dolomitic siltstone-to-sandstone at their bases with 25.1 shallowing to fenestral laminite updip (seaward of siliciclastic amalgamation) and foreshore ooid-fusulinid grainstone/rudstone to outer shelf rudstones and packstones distally. Cycle 25.2 contains a higher percentage of outer shelf facies which are present considerably further updip, relative to 25.1; likewise, this cycle is capped by thinner ooid grainstone foreshore facies and grades distally into only outer shelf packstones. Carbonate facies within siliciclastic-based cycle 25.3 are significantly limited in dip width, grading from outer shelf packstone through foreshore ooid grainstone into siliciclastics within ~350 meters of the margin. Cycle 25.4 is similarly siliciclastic-based, but shallows to predominantly shelf crest facies across the study area, with outer shelf skeletal-ooid grainstones and packstones distally. Cycles 24.5 to 24.14 are almost entirely carbonates, with an aggradational to progradational stacking pattern. A thin tongue of outer shelf packstone extends well up the shelf in 24.5, across the proximal half of the study area tepee-pisoid rudstones dominate above it, broken only by thin fenestral laminites and occasional dolomitic siltstone-to-sandstone. Distally, cycle bases are typically outer shelf packstones shallowing to outer shelf grainstones, rudstones, and shelf crest grainstones respectively. The tepee-pisoid rudstone complex prograded significantly following cycle 25.10, resulting in a severe reduction in outer shelf dip width and a facies tract offset of low to moderate energy shelf crest facies over those from the moderate to low energy outer

shelf. Shelf crest facies are present in close proximity to the 26.0 sequence bounding margin.

Although faulting obscures much of the early shelf margin development, it is likely that progradation and aggradation were relatively balanced during the deposition of cycles 25.1 to 25.7, with progradation slightly exceeding aggradation. Progradation was strongly dominant at the margin for the remainder of the cycles (25.8-25.14).

Growth faulting occurred in a number of locations during G25 deposition within the study area. In the Walnut Canyon Syncline group of faults, maximum cycle offset occurred on the proximal downthrown block (~ 5m), and growth largely ceased by cycle 25.7. The fault above the terminal G23 margin was also active during G25 deposition, with a maximum cycle offset of approximately 8 meters; growth progressively declined upward throughout the HFS, terminating in the amalgamated shelf crest facies. Large faults additionally developed distally in the Ogle Cave Fault System; however, growth was difficult to measure on these faults due to poor marker beds through the area. It is likely that some amount of growth occurred across these faults as growth is observed in the G26 HFS and correction for basinward bed rotation (up to 5.5 degrees) was needed for the reconstruction of the G25.

There are two good candidates for a maximum flooding surface within the G25 HFS, found in cycles 25.2 and 25.5. Cycle 25.2 shows the furthest landward extent of subtidal outer shelf facies however it contains a siliciclastic base and is also overlain by siliciclastics, both indicating low (but increasing) accommodation across the shelf. Cycle 25.5 shows the next most landward extent of subtidal outer shelf facies, but it grades into shelf crest facies soon afterward. The cycle architecture above 25.5 is dominantly aggradational and progradational; therefore cycle 25.5 better represents the turnaround

from transgression through aggradation to progradation; while 25.2 is still largely transgressive.

The sequence boundary of the G25 is a significant exposure surface and the CS 13/14 composite sequence boundary. There is significant facies tract offset of thick proximally sourced siliciclastics sharply overlying the uppermost shelf crest and high energy outer shelf facies. Caliche crusts and brecciated laminite intraclasts are common along this surface similar to the observations of Kerans and Harris (1993) in McKittrick Canyon; additionally, Rush and Kerans detail conglomerates of G25-derived dolomite clasts within the lowest G26 siliciclastics along strike in Walnut Canyon.

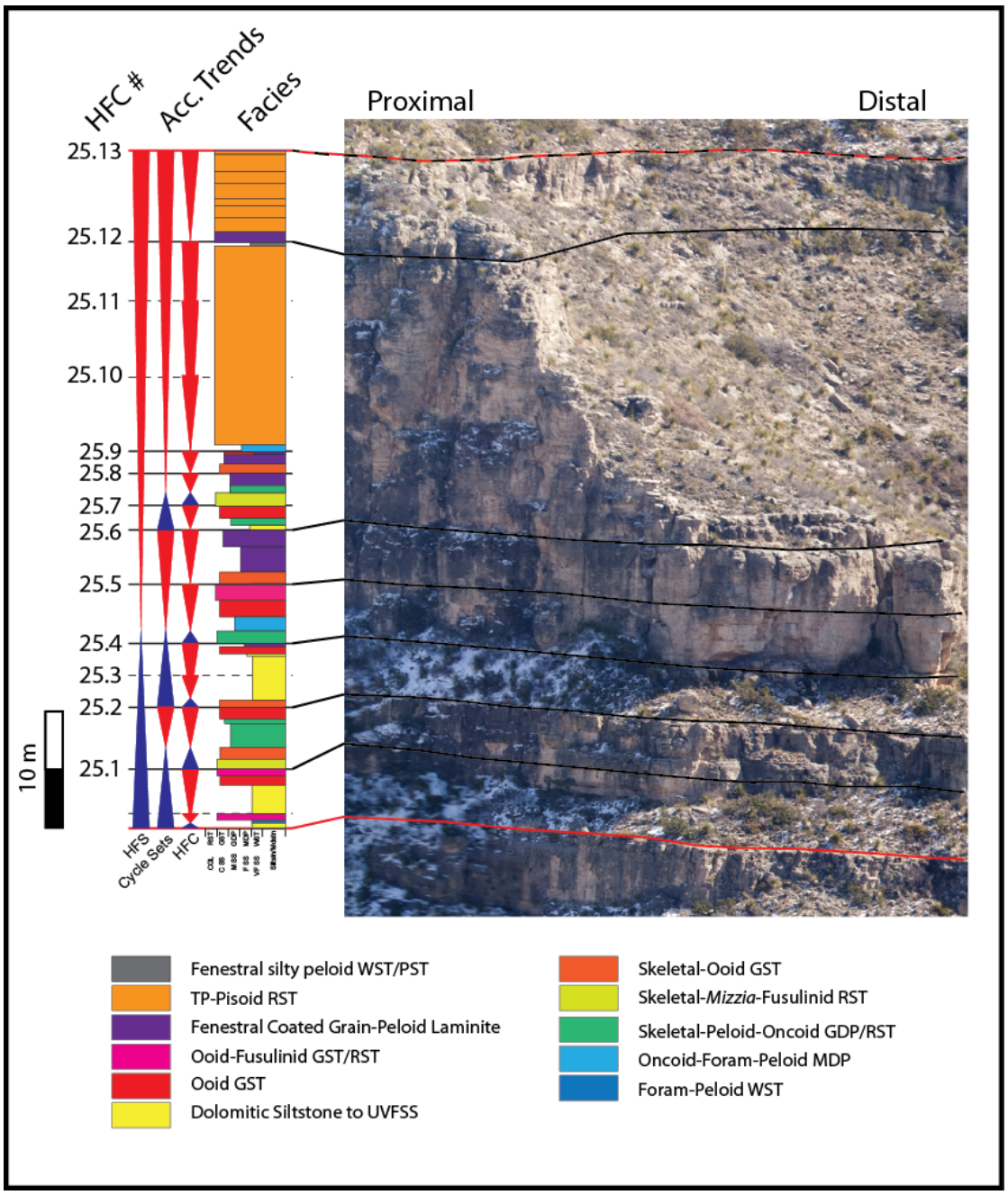

Figure 32: Measured Section D covering the G25 HFS and referenced to its approximate outcrop location with cycle number, cycle set, and HFS accommodation trends indicated. Abbreviations identical to those in Figure 20. Photograph from Plate I.

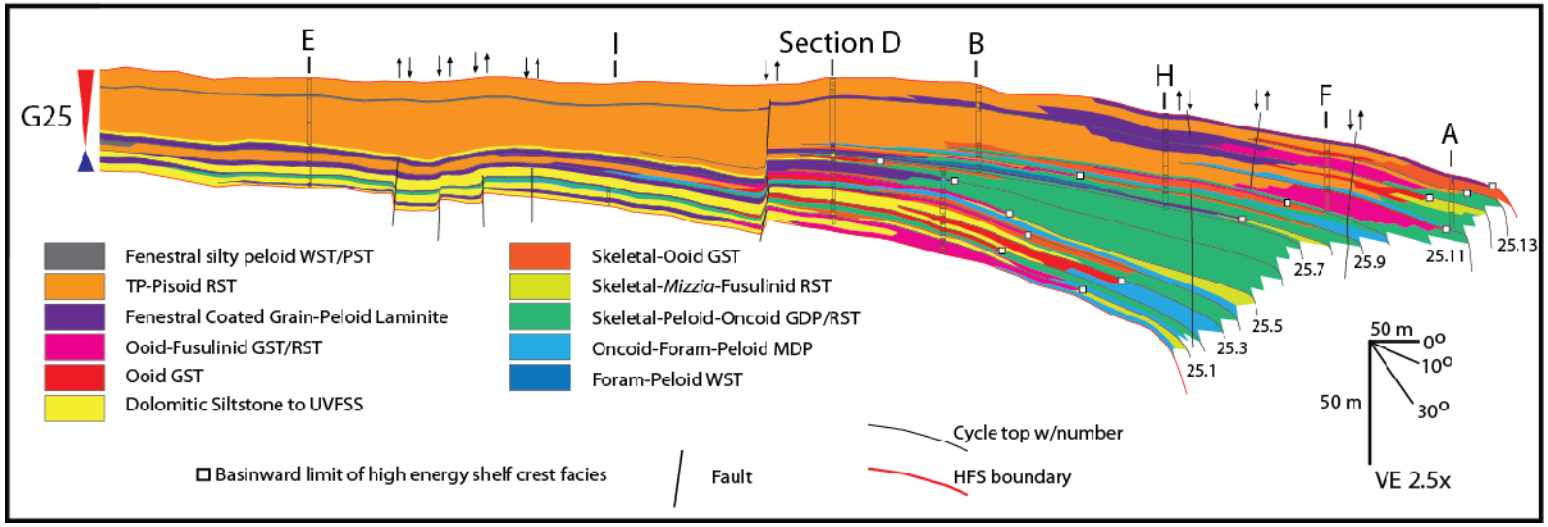

Figure 33: Reconstructed lidar-projected cross section showing the cycle-scale distribution of facies within the G25 HFS. The location of Measured Section D is noted for reference to Figure 24. Solid black lines show the location of faults. HFS-scale accommodation triangles for the G25 are shown at the left; their shared apex represents the location of the maximum flooding surface. See Plate # for a more detailed version of this figure.

G26

The G26 HFS outcrops across the entire study area and is one of the most distinctive intervals throughout the canyon, due to the large percentage of siliciclastics which progressively split and thin in a basinward direction (Figures 34, 35, 36). It is characterized by 7 high-frequency cycles of which cycles 26.1, 26.2, 26.6 and 26.7 all amalgamate into siliciclastics updip. Cycle 26.1 is distinct only within a few hundred meters of the margin and is composed of a lower dolomitic siltstone-to-sandstone bed grading up into high energy outer shelf skeletal-ooid grainstones and outer shelf packstones distally. This cycle records the initial transgression following the G25/G26 CS13 boundary. Cycle 26.2 transgresses further on the shelf and contains a thicker carbonate package above a lower siliciclastic bed that extends almost all the way to the margin. This cycle shallows through outer shelf packstones to shelf crest ooid grainstones distally and to shelf crest/middle shelf fenestral laminites proximally. Cycles 26.1 and 26.2 lose their carbonate facies at approximately 1 km from the margin and are represented by only siliciclastics further landward. Cycles 26.3 and 26.4 are closely related as 26.3 amalgamates into 26.4 in a series of stacked foreshore ooid grainstones close to the margin. Where they are distinct, cycle 26.3 is siliciclastic-based and shallows proximally to fenestral laminites and distally to foreshore grainstones with outer shelf packstones at the margin. Cycle 26.4 is characterized by a foreshore ooid grainstones grading distally into outer shelf skeletal-ooid grainstones and *Mizzia* packstones. Proximal to the foreshore, facies deepen to outer shelf packstones over the Ogle Cave Fault System in what may be an area of localized subsidence, before grading into shelf crest fenestral laminites. Cycle 26.5 shows the typical proximal to distal facies transition of shelf crest to outer shelf, although there is little record of initial transgression except as the margin. Cycles 26.6 and 26.7 are very similar to the siliciclastic-based 26.1 and 26.2,

but they show a larger proportion of high energy shelf crest and outer shelf facies within upper carbonate-rich portions of the cycles.

Although the sequence-bounding shelf margins are relatively well exposed, the margin is poorly exposed in between; stacking patterns suggest that progradation (88 m) was relatively more balanced with aggradation (22 m) during the deposition of the G26.

Thickening of G26 cycles occurred in the area of the Ogle Cave Fault System. Maximum cycle offset around the OCFS was approximately 4 meters, most of which was accommodated by the deposition of cycle 26.5. Two additional faults are present above the G25 terminal margin but again the lack of a good marker bed impedes the ability to measure growth.

The maximum flooding surface of the G26 developed in the middle of cycle 26.4, as indicated by the greatest landward transgression of subtidal outer shelf facies.

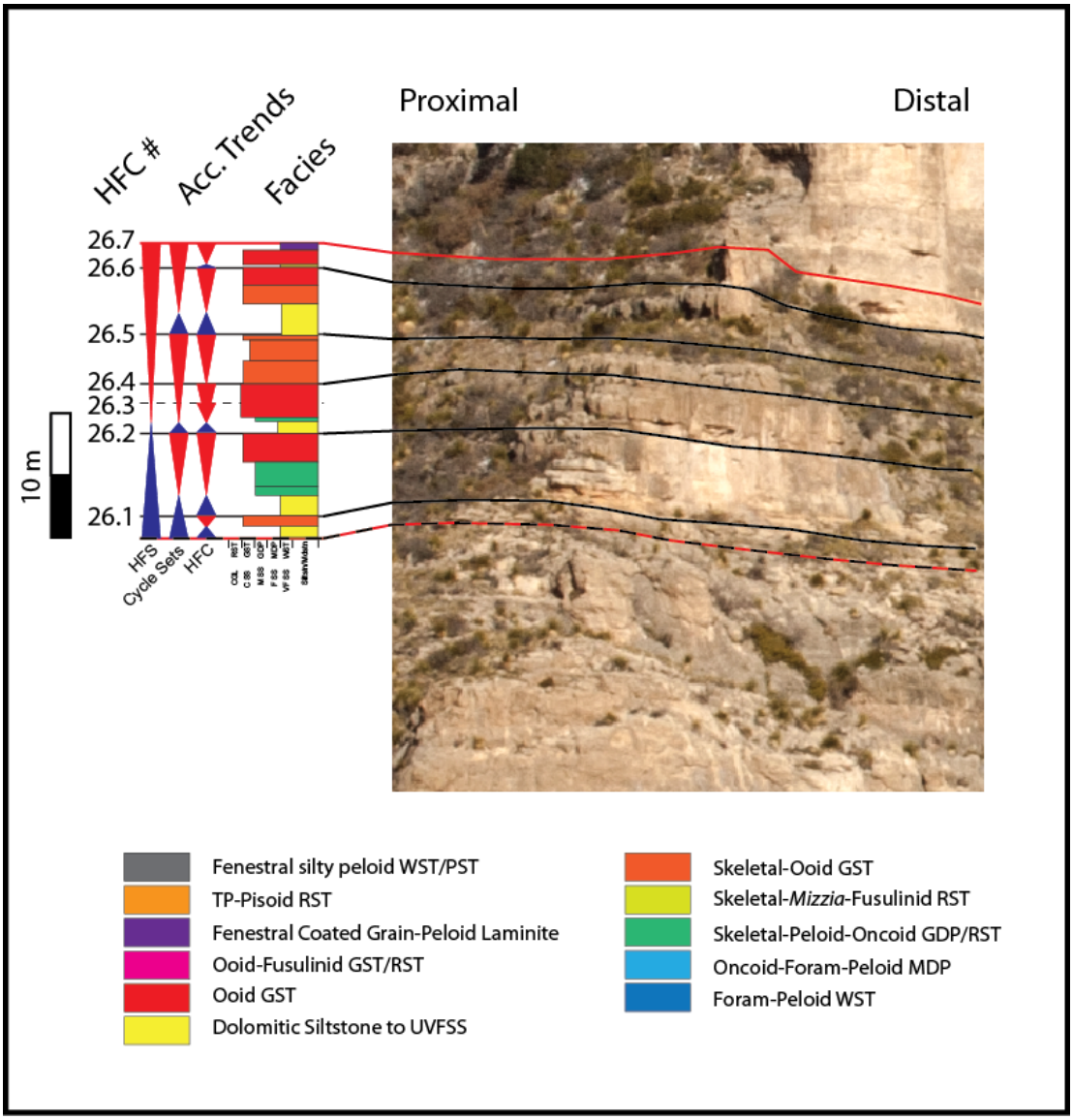

Figure 34: Measured Section A covering the G26 HFS and referenced to its approximate outcrop location with cycle number, cycle set, and HFS accommodation trends indicated. Abbreviations identical to those in Figure 20. Photograph from Plate II.

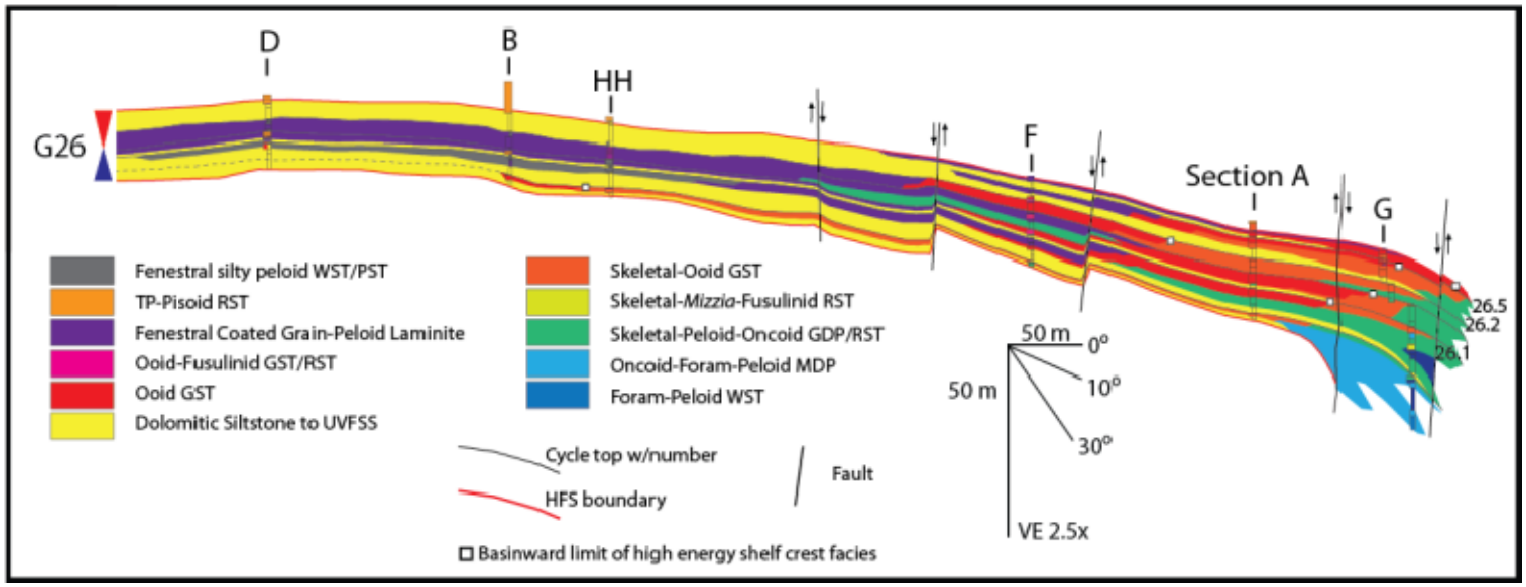

Figure 35: Reconstructed lidar-projected cross section showing the cycle-scale distribution of facies within the G26 HFS. The location of Measured Section A is noted for reference to Figure 26. Solid black lines show the location of faults. HFS-scale accommodation triangles for the G26 are shown at the left; their shared apex represents the location of the maximum flooding surface. See Plate # for a more detailed version of this figure.

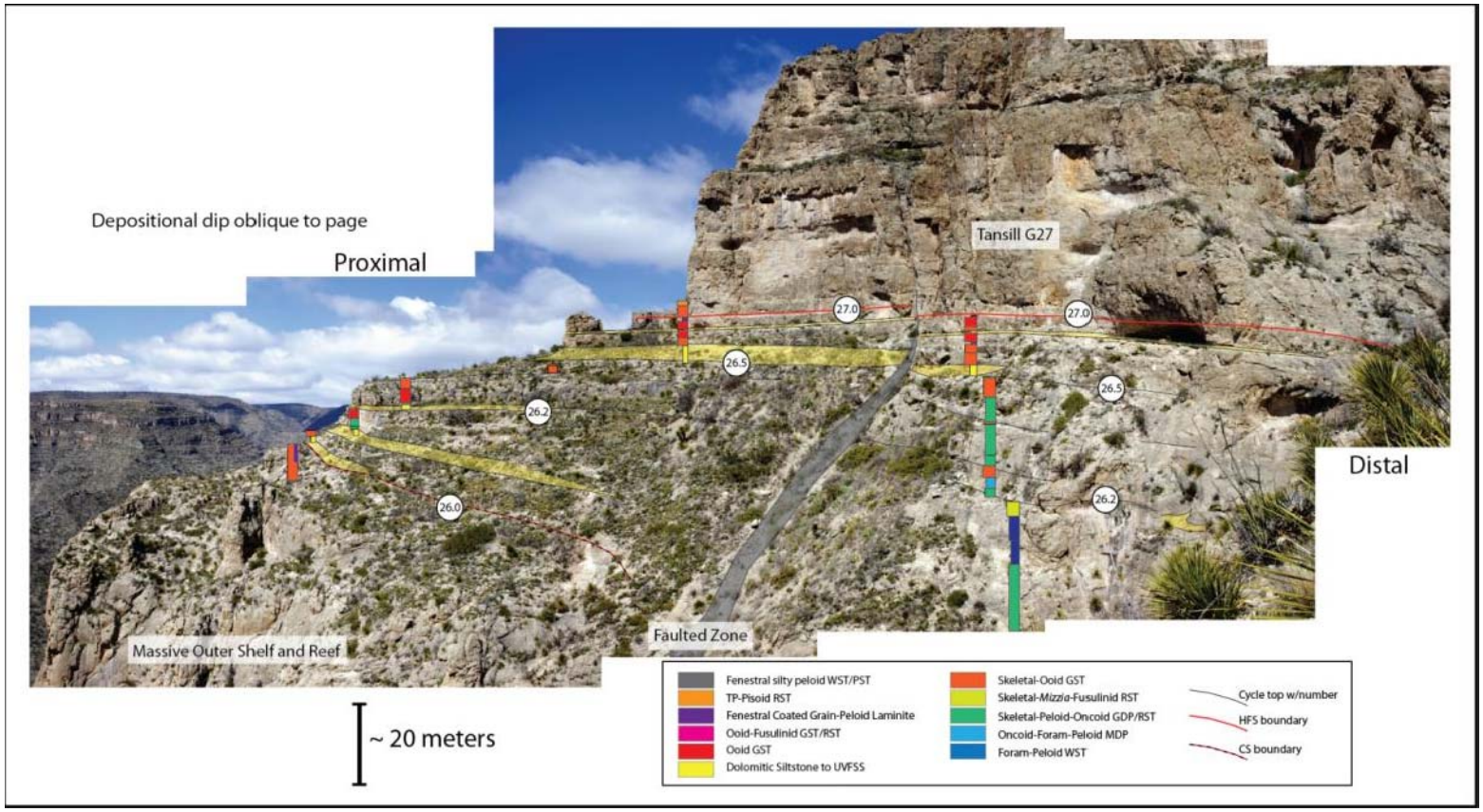

Figure 36: Interpreted outcrop photomosaic with Sections A (left) and G (right) showing the most distal portion of the G26 HFS, showing the basinward pinch out of the middle shelf-derived dolomitic siltstone to sandstones which converge updip. The massive, cliff-forming shelf margin facies are visible at the bottom left. Horizontal field of view ~170 meters, outcrop is oblique to photographer.

QUANTIFIED STRATIGRAPHIC VARIABLES

Quantification of key depositional parameters provides a means to evaluate the evolution of a depositional system and provides values which can be compared to other related systems (Sonnenfeld and Cross, 1993; Kerans and Fitchen, 1995; Tinker, 1996, 1998; Osleger, 1998; Kerans and Tinker, 1999; Osleger and Tinker, 1999; Carvajal and Steel, 2006; Frost and Kerans, 2009; Pyles et al., 2010). The quantified stratigraphic variables of: progradation to aggradation (P/A) ratio, facies proportions, facies tract widths, and facies tract bedding angles were used to assess the intrinsic and extrinsic controls on facies distribution and stratal architecture (Figure 32). Measurements were taken from the projected lidar cross sections (insitu and/or reconstructed) in Adobe Illustrator with the appropriate unit conversion in spreadsheet software. A number of previous studies have quantified various aspects of the Yates depositional system (Tinker, 1996, 1998; Osleger, 1998; Kerans and Tinker, 1999; Osleger and Tinker, 1999; Hunt et al., 2002; Kosa and Hunt, 2005); although most cover the lower HFS's (G21-G25), leaving the G26 largely undocumented (P/A found in Kerans and Tinker, 1999). The new data of this study overlaps some of this previous work (P/A ratios particularly), but largely addresses complimentary new stratigraphic variables at the cycle-scale that build on the prior foundation.

Work by Tinker (1996, 1998) showed the utility of quantified stratigraphic variables for sequence stratigraphic analysis in the Seven Rivers-Yates-Capitan system exposed in McKittrick Canyon. This work documented the HFS-scale (TST and HST) shelf margin and shelf crest P/A ratios and the analogous respective offlap angles, the dip width between the shelf crest and reef, the depth of the reef, the dip of the outer shelf, the dip width from the shelf crest to the basin, the depth to the basin, and HFS-scale accumulation rates. A number of trends were recognized: (1) aggradation was greater

during TST's at the shelf crest and margin, (2) P/A ratios of the margin decreased towards CS-scale MFS's and increased towards CS-scale SB's, (3) the shelf margin prograded in both the CS 13 TST and HST, (4) the shelf crest to margin distance is greater during each HFS's MFS than its respective SB, (5) the depth to the margin increases in TST's and decreases in HST's.

Osleger's (1998) study of the Yates Fm. in Slaughter Canyon characterized a similar set of stratigraphic variables including: the HFS-scale (not split into TST/HST) shelf margin and shelf crest P/A ratios and the analogous respective offlap angles, the downdip thickness increase, the shelf crest aspect ratio, the outer shelf aspect ratio, the distance from the shelf crest to the reef, the landward extent of maximum flooding, the shelf crest progradation rate, and the depth to the reef. The results of these measurements largely agree with the trends outlined in Tinker (1998), indicating an along-strike correlation illustrated and discussed in Osleger and Tinker (1999).

Kerans and Tinker (1999) used shelf margin progradation to aggradation ratios to characterize the evolution from ramp to rimmed shelf recorded by the CS 9 to CS 14, encompassing the majority of the stratigraphic section exposed in the Guadalupe Mountains. They showed that different styles of carbonate platforms can be categorized by P/A ratios when accommodation setting is considered (TST or HST), as well as the influx of siliciclastics (more with high P/A). Additionally, they establish a link between the occurrence of well-developed tepee complexes, time-equivalent shallow reef margins, and shelf margin P/A values < 20. This relationship is founded on the model that tepee development requires a relatively stable shoreline (low P/A), and that the distal reefs have more growth potential when they are protected from restricted, inner and middle shelf waters by robust tepee complexes (Kerans and Tinker, 1999). Consequently, HFS with

shelf margin P/A ratios > 20 have deeper reefs (if at all) and more poorly developed shelf crest tepee complexes.

Hunt et al. (2002) and Kosa and Hunt (2005) quantified the geometry and distribution of Seven Rivers and Yates-aged growth faults in the Yates, as well as their displacement, the rates of fault propagation, growth percentage, and tilting of associated strata. Within the study area the authors documented a maximum syndepositional fault displacement of 24 meters, fault widths up to 9 m, and maximum rates of propagation (0.088-0.123 m/ka) which were less than platform accumulation rates (0.053-0.336 m/ka). Although the rate data suggests that faulting rarely broke the depositional surface, Kosa and Hunt documented a few examples where this did occur, coinciding predominantly with platform exposure. Poor chronostratigraphic resolution impedes our ability to better describe the dynamic interaction and partitioning of accumulation and propagation rates.

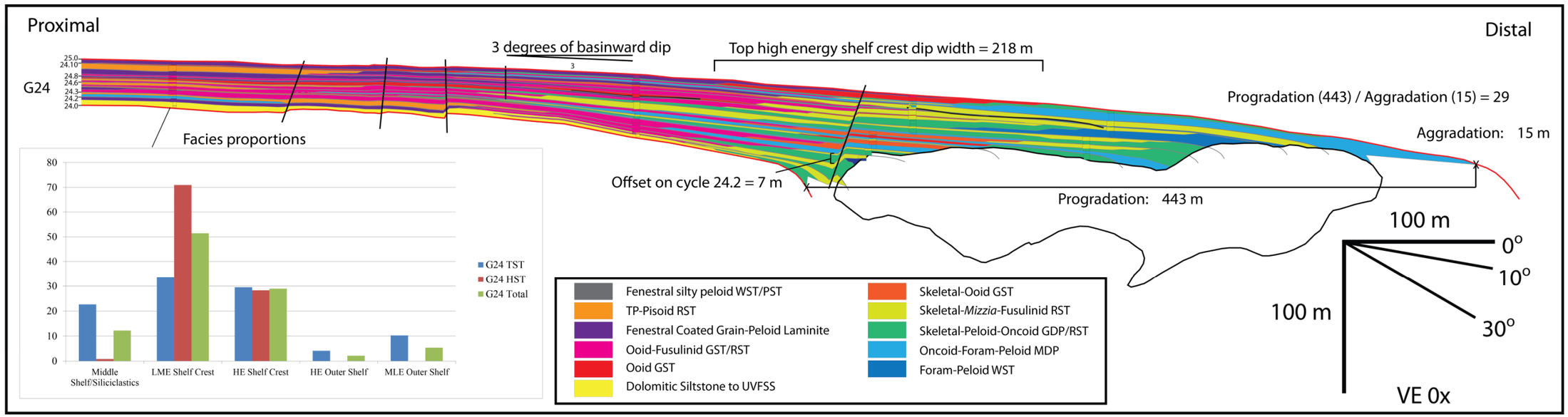

Figure 37: Reconstructed G24 HFS with annotation of the quantified P/A ratios, facies proportions from Section E, facies tract dip widths, facies tract bedding angles, and growth/cycle offset during G24 deposition. These measurements were applied throughout this and the other studied HFS. See following Tables and Figures for a summary of the data. The faults shown here correspond to the F, G, H, I, and J (left-to-right) faults of Kosa and Hunt, 2006a.

Progradation to Aggradation Ratios

The ratio of progradation to aggradation for a defined stratigraphic unit is a useful value to evaluate the accommodation and sediment supply conditions during its deposition, and to compare changes in those conditions between related units (Kerans and Tinker, 1999). The progradation to aggradation ratios were determined using the methodology for the shelf margin progradation to aggradation ratios (SMP/A) outlined in Kerans and Tinker (1999). These measurements were done at the HFS-scale, as poor outcrop of the shelf margin hindered a finer scale of investigation. The P/A ratio for each HFS was taken on the reconstructed cross sections, eliminating any alteration of the sequence geometry by younger fault movement (Figure 37).

The G23 HFS is characterized by a P/A ratio of 16 (471 m/29 m), the G24 showed more relative progradation with a ratio of 29 (443 m/15 m), the G25 exhibited a more balanced ratio of 5 (339 m/62 m), and the G26 showed the lowest ratio of 4 (88 m/22 m). These values follow the same general trend as those in the literature for the Yates in Slaughter and McKittrick Canyons (Table 2, Figure 38). The ratios for the G23 and G24 are larger than those computed by Osleger (1998) in Slaughter, suggesting that this study's lidar-projected cross section methodology contributed to this difference in P/A value. Variability in time-equivalent P/A values between Slaughter and McKittrick Canyons is likely due to strike-variability in the Yates-Capitan depositional system (Osleger and Tinker, 1999).

The series of HFS P/A values (16-29-5) below the composite sequence boundary between the G25 and G26 show that while cycle stacking on the shelf indicates progressive accommodation loss, the P/A ratio did not simply increase. This divergence from the model of Tinker (1998) (who placed of the CS boundary above the G24) is

supported by the association of robust tepee development with shallow reef development from Kerans and Tinker (1999). Therefore the establishment of a wide, well developed low to moderate energy shelf crest in the G25 allowed for enhanced aggradation (growth) of the time equivalent reef, lowering the P/A ratio for the HFS despite significant shelf progradation. The low P/A ratio of the G26 is logical considering its transgressive position in the CS 14.

Facies Proportions

Facies proportions quantify the percentage of a vertical stratigraphic unit composed by an individual facies or facies tract. These values allow for the identification of partitioning of facies by stratigraphic interval (CS/HFS) as well as accommodation setting (TST/HST). Facies proportions were calculated using Measured Section E, which is the only section to fully intersect the G23 through the G26 within the study area; serving as an analogue to a vertical core through the profile. Section E is located about 700 m distal to the projected location of the Gulf PDB-04 core (Osleger, 1998). The percent thickness of each shelf facies tract was measured at the scale of entire HFS as well as the finer HFS transgressive cycles versus HFS highstand cycles (Table 3). These two scales of measurement show differentiation of facies tracts by accommodation position within a HFS (TST or HST) as well as by dip position, due to the progradation of the entire shelf from G23 to G26 deposition.

The G23 HFS in Section E is composed of 2% middle shelf/siliciclastic facies, 4% low to moderate energy shelf crest facies, 36% high energy shelf crest facies, 27% high energy outer shelf faces, and 30% moderate to low energy outer shelf facies (Table 3). The transgressive cycles of the G23 contain a relatively higher percentage of moderate to low energy outer shelf facies and middle shelf/siliciclastics and a relatively lower

percentage of high energy outer shelf facies, high energy shelf crest facies, and low to moderate energy shelf crest facies. The highstand cycles of the G23 show the opposite trend of the TST, with greater relative percentages of high energy outer shelf, high energy shelf crest, and low to moderate energy shelf crest facies. Percentages of middle shelf/siliciclastics and moderate to low energy outer shelf facies likewise decreased (Figure 39). Section E is located 527 m proximal to the terminal G23 margin.

The G24 HFS in Section E is composed of 12% middle shelf/siliciclastics, 51% low to moderate energy shelf crest facies, 29% high energy shelf crest facies, 2% high energy outer shelf facies, and 5% moderate to low energy outer shelf facies (Table 3). The transgressive cycles of the G24 again show larger relative percentages of moderate to low energy outer shelf facies, high energy outer shelf facies, and middle shelf/siliciclastic facies; with lower percentages of low to moderate energy shelf crest facies and nearly equivalent high energy shelf crest facies. The highstand cycles of the G24 also show the inverse, with higher percentages of low to moderate energy shelf crest facies and lower percentages of moderate to low energy outer shelf facies, high energy outer shelf facies, and middle shelf/siliciclastic facies (Figure 39). Section E is located 860 m proximal to the terminal G24 margin.

HFS		G23	G24	G25	G26
Reconstructed P/A (This Study)		16	29	5	4
McKittrick Canyon from Tinker and Osleger (1999)		11	37	5	
Slaughter Canyon from Tinker and Osleger (1999)		10	23	7	
Kerans and Tinker (1999)					5
McKittrick Lidar (Unpublished)				10	5
Average		12	30	7	5

Table 2: Progradation to aggradation ratios (P/A) for the G24-G26 HFS's observed in the study as well as those from previous work in Slaughter and McKittrick Canyons. Note the generally strike-parallel trends between Slaughter and McKittrick Canyons. See Figure for graphical comparison of these values.

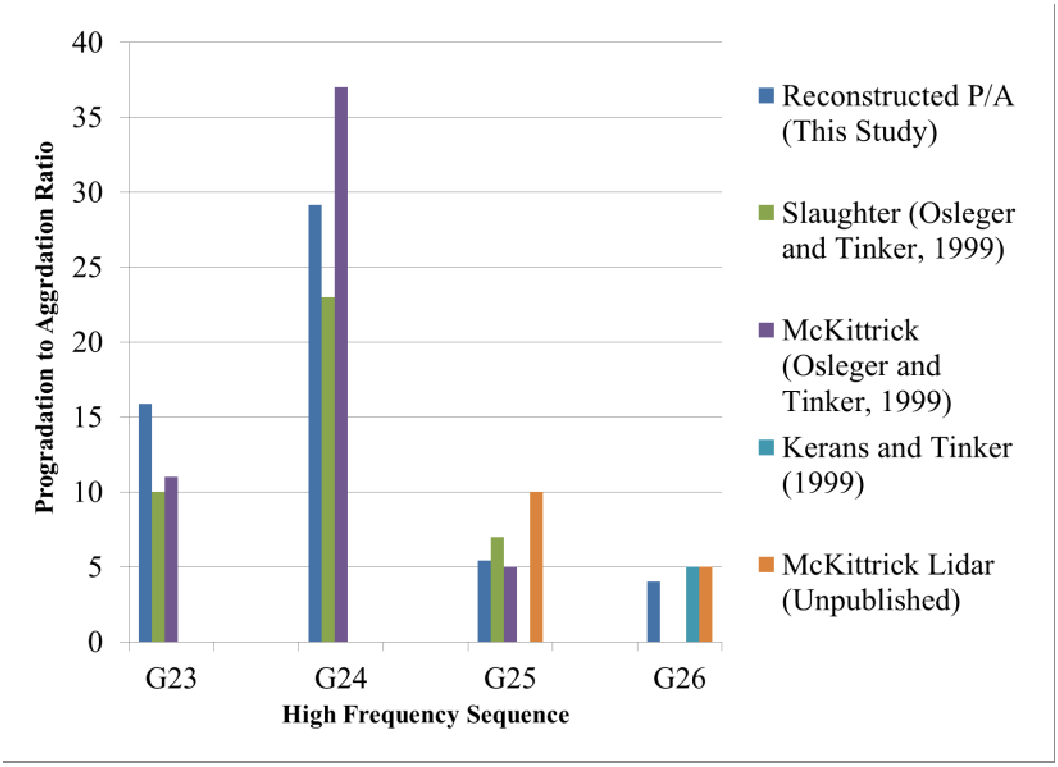

Figure 38: Graphical comparison of the P/A ratios calculated for the G23-G26 HFS in this study versus those from previous work in Slaughter and McKittrick canyons. Again note that despite small variations, the overall P/A trends correlate along strike between Slaughter and McKittrick Canyons.

G26 - Section E					
Middle Shelf/Siliciclastics	LME Shelf Crest	HE Shelf Crest	HE Outer Shelf	MLE Outer Shelf	
70	30	0	0	0	**TST**
70	30	0	0	0	**HST**
70	30	0	0	0	**Total**

G25 - Section E					
Middle Shelf/Siliciclastics	LME Shelf Crest	HE Shelf Crest	HE Outer Shelf	MLE Outer Shelf	
44	45	4	0	8	**TST**
6	94	0	0	0	**HST**
18	78	1	0	3	**Total**

G24 - Section E					
Middle Shelf/Siliciclastics	LME Shelf Crest	HE Shelf Crest	HE Outer Shelf	MLE Outer Shelf	
23	34	29	4	10	**TST**
1	71	28	0	0	**HST**
12	51	29	2	5	**Total**

G23 - Section E					
Middle Shelf/Siliciclastics	LME Shelf Crest	HE Shelf Crest	HE Outer Shelf	MLE Outer Shelf	
11	0	19	15	55	**TST**
0	6	41	30	24	**HST**
2	4	36	27	30	**Total**

Table 3: Facies proportions (percent total thickness) for each HFS, calculated using Section E. Each HFS was divided into transgressive cycles (TST) and highstand cycles (HST) to illustrate any partitioning relative to the entire HFS (Total). LME = low to moderate energy; HE = high energy; MLE = moderate to low energy. Graphical representation of this data found in Figure 34.

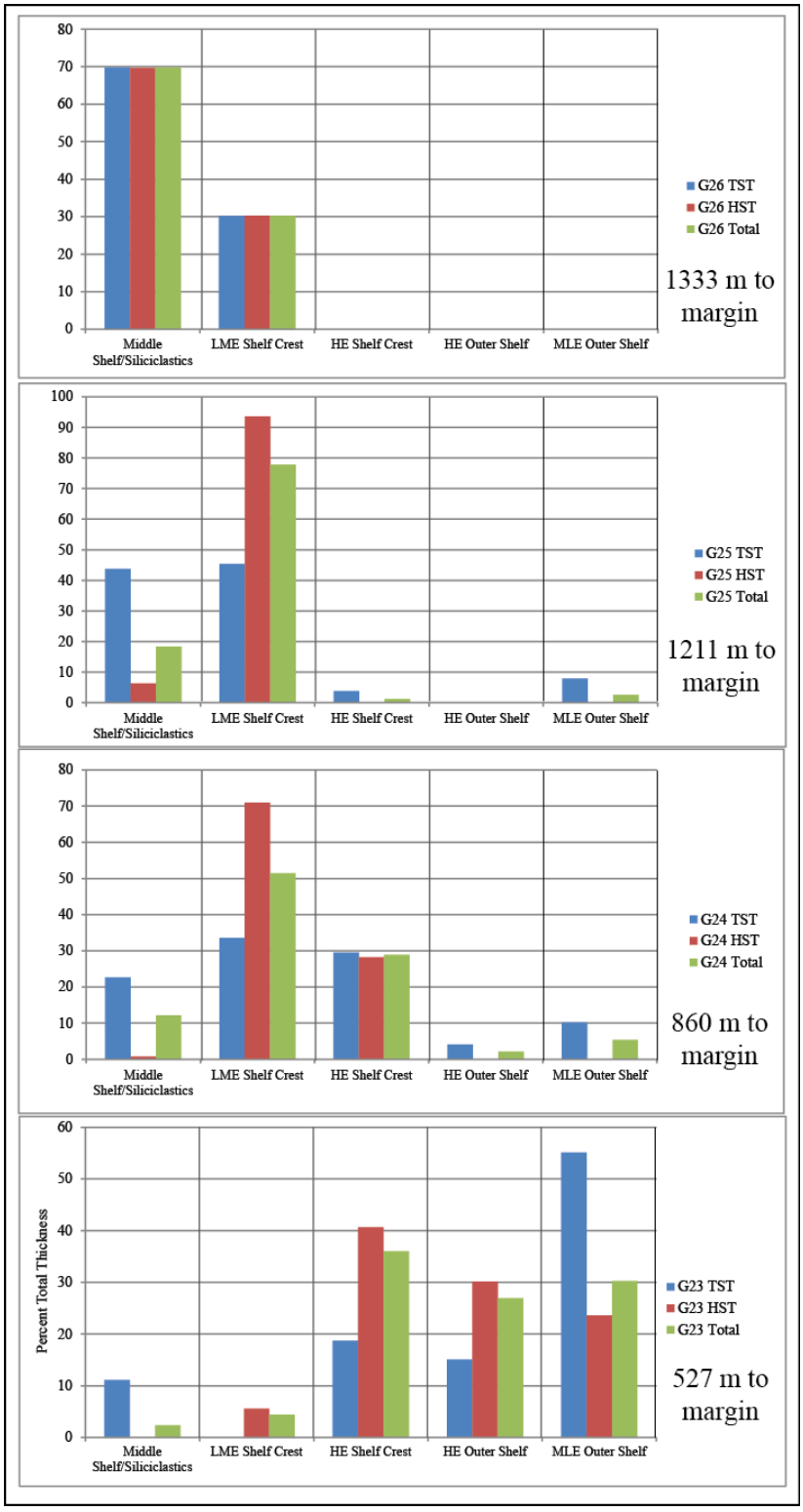
80
70
60
50
40
30
20
10
0
Middle Shelf/Siliciclastics
LME Shelf Crest
HE Shelf Crest
HE Outer Shelf
MLE Outer Shelf
G26 TST
G26 HST
G26 Total
1333 m to margin
100
90
80
70
60
50
40
30
20
10
0
Middle Shelf/Siliciclastics
LME Shelf Crest
HE Shelf Crest
HE Outer Shelf
MLE Outer Shelf
G25 TST
G25 HST
G25 Total
1211 m to margin
80
70
60
50
40
30
20
10
0
Middle Shelf/Siliciclastics
LME Shelf Crest
HE Shelf Crest
HE Outer Shelf
MLE Outer Shelf
G24 TST
G24 HST
G24 Total
860 m to margin
60
50
40
30
20
10
0
Percent Total Thickness
Middle Shelf/Siliciclastics
LME Shelf Crest
HE Shelf Crest
HE Outer Shelf
MLE Outer Shelf
G23 TST
G23 HST
G23 Total
527 m to margin

Figure 39: Graphical representation of facies proportion data for the G23-G26 in Section E. Note partitioning of facies tracts to transgressive or highstand cycles relative to the total for the HFS, as well as the upward decrease in outer shelf facies associated with shelf progradation. Vertical scales are not identical; abbreviations are the same as in Table 3.

The G25 HFS in Section E is composed of 18% middle shelf/siliciclastic facies, 78% low to moderate energy shelf crest facies, 1% high energy shelf crest facies, 3% moderate to low energy outer shelf facies, and contains no high energy outer shelf facies (Table 3). The transgressive cycles of the G25 are characterized by higher relative percentages of moderate to low energy outer shelf facies and middle shelf/siliciclastic facies as well as the only occurrence of high energy shelf crest facies. The highstand cycles of the G25 are dominated by low to moderate energy shelf crest facies and a relatively lower percentage of middle shelf/siliciclastic facies (Figure 39). Section E is located 1211 m proximal to the terminal G25 margin.

The G26 HFS in Section E is entirely composed of middle shelf/siliciclastic facies (70%) and low to moderate energy shelf crest facies (30%) (Table 3). Interestingly, there was no differentiation of these percentages between the TST and the HST, likely due to the accommodation-limited nature of the whole sequence and the updip (1333 m proximal to the G26 terminal margin) location of Section E (Figure 39).

While the HFSs and their constituent TST's and HST's are defined by the stacking patterns of facies, these quantified proportions support the consistency and predictability established with the current sequence organization.

Facies Tract Dip Widths

The variable facies tract dip width is similar to the dip widths and aspect ratios described by Tinker (1998) and Osleger (1998). This study provides new data at the high frequency cycle-scale of investigation, rather than HFS as for previously mentioned works. The value of each cycle-scale facies tract dip width represents the maximum horizontal extent of that depositional environment during that cycle’s deposition (Figure 37). A distinction of facies tracts from geobodies here is important, as similar adjacent

facies are grouped (facies tract) rather than measurement of individual sedimentologically-continuous geobodies. While some of these measurements do likely record the width of an individual geobody, many record the width of composite geobodies that formed in similar depositional environments.

Cycle-scale dip widths of the high energy shelf crest, high energy outer shelf, and moderate to low energy outer shelf facies tracts were measured in the reconstructed G24-G26 HFS. Facies tract widths from the G23 HFS were not calculated as the updip limits of most facies tracts did not occur in the study area. The dip widths of the middle shelf and low to moderate energy shelf crest facies tracts were also not measured as both often do not have updip terminations within the study area (non-stationary data). A graphical summary of the facies tract dip width data is shown in Figure 40 and the raw data can be found in the Appendix. A summary of the trends for each measured facies tract follows.

When present in a cycle, the moderate to low energy outer shelf facies tract dip widths vary from less than 100 m to over 1000 m. These widths generally increase towards HFS maximum flooding surfaces, consistent with the observations of Tinker (1998). The G25 and G26 HST's both show progressively smaller dip widths with proximity to the sequence boundary; however, the G24 HST does not contain as clear a trend (Figure 40).

Dip widths of the high energy outer shelf facies tract are smaller than those of the moderate to low energy outer shelf, with a range of less than 100 m to just more than 500 m, when present in a cycle. The G24 HFS exhibits a trend of increasing high energy outer shelf dip widths towards the maximum flooding surface and stable to decreasing dip widths from the MFS to the sequence boundary. The G25 TST likewise shows increasing dip widths through the TST to the MFS, but has no distinct trend in the HST. The G26 HFS contains the largest high energy outer shelf dip width (521 m) in the first cycle of its

TST, above which dip width of this facies tract is significantly less, although there is a subtle increase towards the MFS and decrease towards the SB (Figure 40).

Dip widths of the high energy shelf crest facies tract range from less than 100 m to just over 600 m. The TST of the G24 roughly increases towards the MFS, the TST dip widths of the G25 remains relatively constant, and the dip widths of the G26 increase then decrease. The highstand cycles of the G24 and G25 both show an increasing then decreasing dip width trend, although at different scales (G24 significantly greater); while the HST of the G26 shows little change in high energy shelf crest dip widths (Figure 40).

The dip width of each of these facies tract is controlled by the dip extent of their depositional conditions and the processes governing them. As a whole, these facies tracts represent deposition across a high energy intertidal (foreshore) to low energy subtidal bathymetric profile. The distribution (dip width) of depositional conditions across that profile is controlled by the bathymetric gradient, water depth, and wave/current energy. Therefore each cycle's facies tract dip width assemblage shows the maximum transgression of low energy, subtidal conditions, the extent of high energy subtidal conditions, and the progradation of the foreshore. The observed HFS-scale increase and decrease pattern best represents cyclic changes in eustasy, rather than any other process (subsidence pulses), especially considering the facies tract offset of siliciclastics and karstification of faults at sequence boundaries.

Facies Bedding Angle

Facies bedding angles were measured along lidar-referenced surfaces in the "*in situ*" projected cross section where fault displacement and rotation was not corrected. These values are therefore relative dips derived from line tracing of bedding planes in the lidar survey projected to a vertical plane parallel to depositional dip. These dip

measurements average across stratigraphic surfaces approximately 10 to 100 meters in length, rather than decimeter-scale surfaces measured with a compass; thus capturing a more general sense of bathymetry (Figure 37). Previous studies by Hunt et al. (2002) and Kosa and Hunt (2005) documented standard strike and dip measurements mostly updip of this study area; values using this new methodology shows agreement with their published data when applied to the same area. The majority of lidar-resolvable surfaces were either cycle tops or sequence boundaries; as such there are significantly more dip data for cycle capping facies (shelf crest). Each bedding angle was categorized by its underlying facies tract, sequence position, and dip position; a full data table is found in the Appendix. The average dips for facies tracts at the HFS-scale and as a whole are detailed in Table 4.

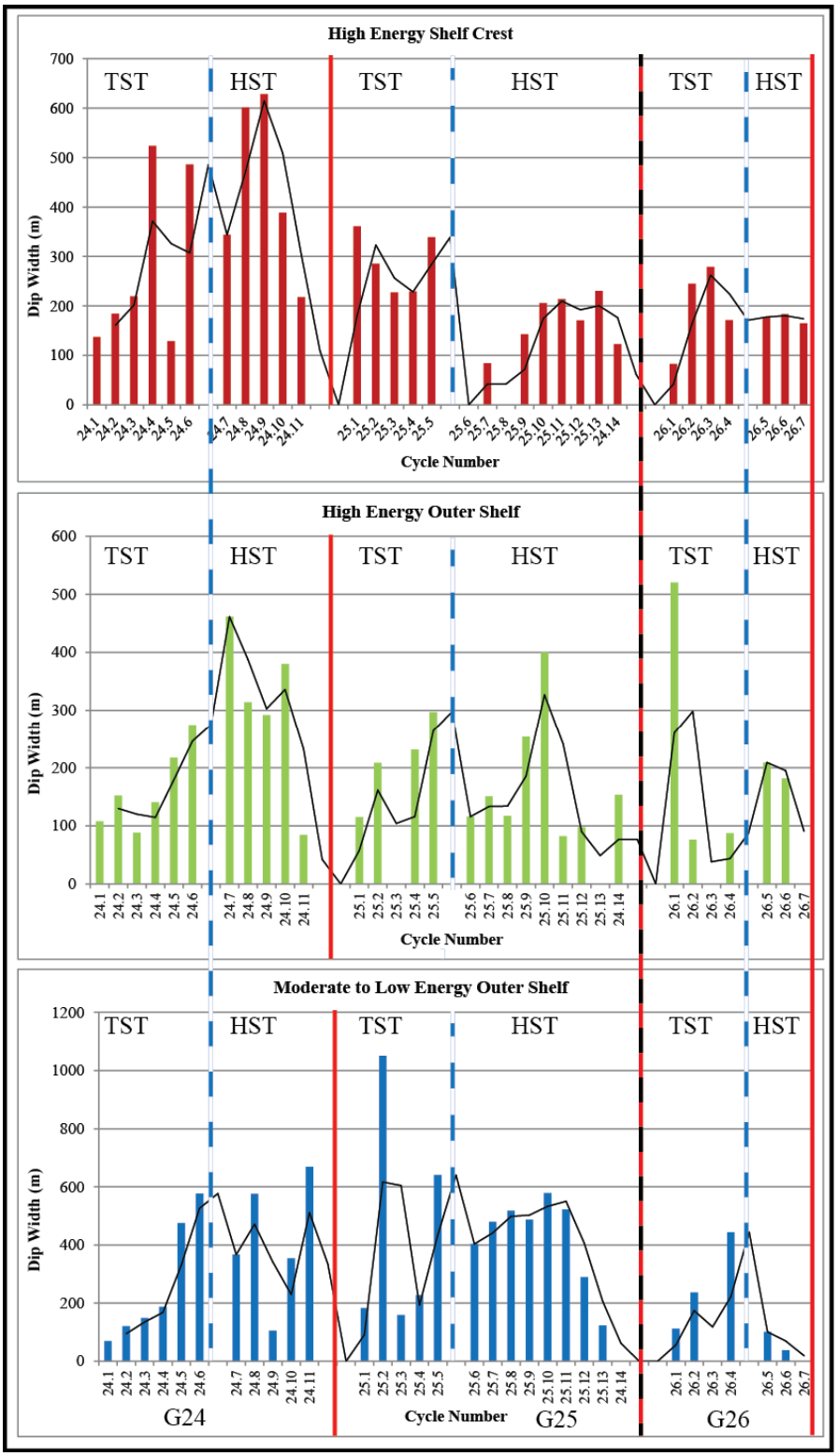
High Energy Shelf Crest
TST
HST
TST
HST
TST
HST
Dip Width (m)
Cycle Number
High Energy Outer Shelf
TST
HST
TST
HST
TST
HST
Dip Width (m)
Cycle Number
Moderate to Low Energy Outer Shelf
TST
HST
TST
HST
TST
HST
Dip Width (m)
Cycle Number
G24
G25
G26

Figure 40: Charts showing cycle-scale facies tract dip width variation in the context of increasing (TST) and decreasing (HST) accommodation. Dashed blue lines are maximum flooding surfaces, solid red lines are HFS sequence boundaries and the black/red dashed line is the CS 13/14 composite sequence boundary. Black trend lines are 2-point moving averages used to illustrate general themes within the data. If a cycle has a zero value, the relevant facies tract was not observed within it. Note that the vertical scales are different (moderate to low energy outer shelf has the largest).

	G23	G24	G25	G26	Overall Average
LME Shelf Crest	2.5	2.3	1.7	1.3	1.7
HE Shelf Crest	3.8	4.0	6.9	6.0	5.8
HE Outer Shelf	6.5	5.0	x	6.0	6.0
MLE Outer Shelf	10.0	8.0	5.0	x	7.9

Table 4: Average facies tract dip angles measured in each HFS, "x" indicating that there were no lidar-referenced surfaces in that HFS overlying the applicable facies tract. Note that within an individual HFS and overall, dip typically decreases in a distal to proximal direction. Additionally note that average dips from the high energy shelf crest and the high energy outer shelf do not increase with age. LME = low to moderate energy; HE = high energy; MLE = moderate to low energy.

Facies tracts within the G23 HFS are characterized by average dips ranging from 10 degrees (moderate to low energy outer shelf) to 2.5 degrees (low to moderate energy shelf crest). Each of the facies tracts excluding the high energy shelf crest exhibited their greatest dip values in the G23 HFS. The G24 HFS's facies tract dips were again greatest in the moderate to low energy outer shelf (8 degrees) and decreased in the respectively shallower facies tracts to 2.3 degrees on the low to moderate energy shelf crest. The average G25 moderate to low energy outer shelf facies tract dip was unusually low (5 degrees) likely due to a limited number of lidar-referenced lines on that facies. The high energy outer shelf facies tract was not represented by the data in the G25, although the high energy shelf crest showed the greatest dips with an average of 6.9 degrees. As in all the HFS, the low to moderate energy shelf crest facies tract showed the lowest average dip of 1.7 degrees. The G26 HFS exhibited a facies tract dip range of 6 degrees (high energy outer shelf and high energy shelf crest) to 1.3 degrees (low to moderate energy shelf crest). There were no lidar-referenced bedding planes of moderate to low energy outer shelf facies in the G26. Overall, the average value of facies tract dip between each HFS decreased from 7.9 degrees in the moderate to low energy outer shelf to 1.7 degrees in the low to moderate energy shelf crest.

While averages are useful to pull apart general trends, evaluation of individual dips from a single facies tract is valuable with the context of time (HFS's) and dip position (Figure 41). Assuming that the fenestral, laminated, and intertidal/supratidal low to moderate energy shelf crest facies tract was deposited in the most flat (0 degree dip) environment (as it was accommodation limited by sea level); tracking the changes and position of this environment's dip effectively documents the geometric evolution of the stratigraphic profile. This data yields a number of general observations: (1) low to moderate energy shelf crest dips are generally inclined basinward, and range from 9.5

degrees dipping towards the basin to 6 degrees dipping towards land (plotted as a negative value in Figure 41); (2) dip angle on younger low to moderate energy shelf crests is typically lower than older crests in the same dip position; (3) the greatest variability in low to moderate energy shelf crest dip angles occurs in close proximity to faults.

The lidar-projected cross section additionally allows for bedding angles to be measured along km-scale bedding plane surfaces which overlie multiple facies tracts. The dip on any surface represents the composite geometry of depositional bathymetry, differential compaction, syndepositional faulting, and post-depositional structural deformation. Given that post-depositional deformation in the area largely occurred on and around pre-existing syndepositional faults (Kosa and Hunt, 2006b), a surface that changes dip across multiple facies tracts away from faults likely records depositional topography with some unknown influence of differential compaction. Data from the G25 HFS shows such a relationship, where a single surface overlies low to moderate energy shelf crest facies dipping 0 degrees that grade into moderate to low energy outer shelf facies dipping 5 degrees (Figure 42). While the number of these multi-facies tract, lidar-resolvable bedding planes is unfortunately low, there are also a number of individual facies tract bedding planes documenting facies tract-partitioned dip values within the same HFS and between faults.

Facies tract dips also aid in the reconstruction of sequence-scale geometric evolution. Starting with the present geometry one can work backward, restoring successive HFS-boundaries based on the assumption that the surface overlying the shelf crest facies tracts should be generally flat. This process of reconstruction highlights the periods of fault offset as well as basinward rotation of bedding between faults (Figure 43). With this analysis we see that at the HFS-scale, growth on the faults occurred

syndepositionally while basinward rotation of surfaces between the faults largely occurred during the deposition of the overlying sequences. Basinward rotation of strata was also dominantly focused on the most distal portion of each HFS, typically only in the sediments distal to the underlying HFS margin.

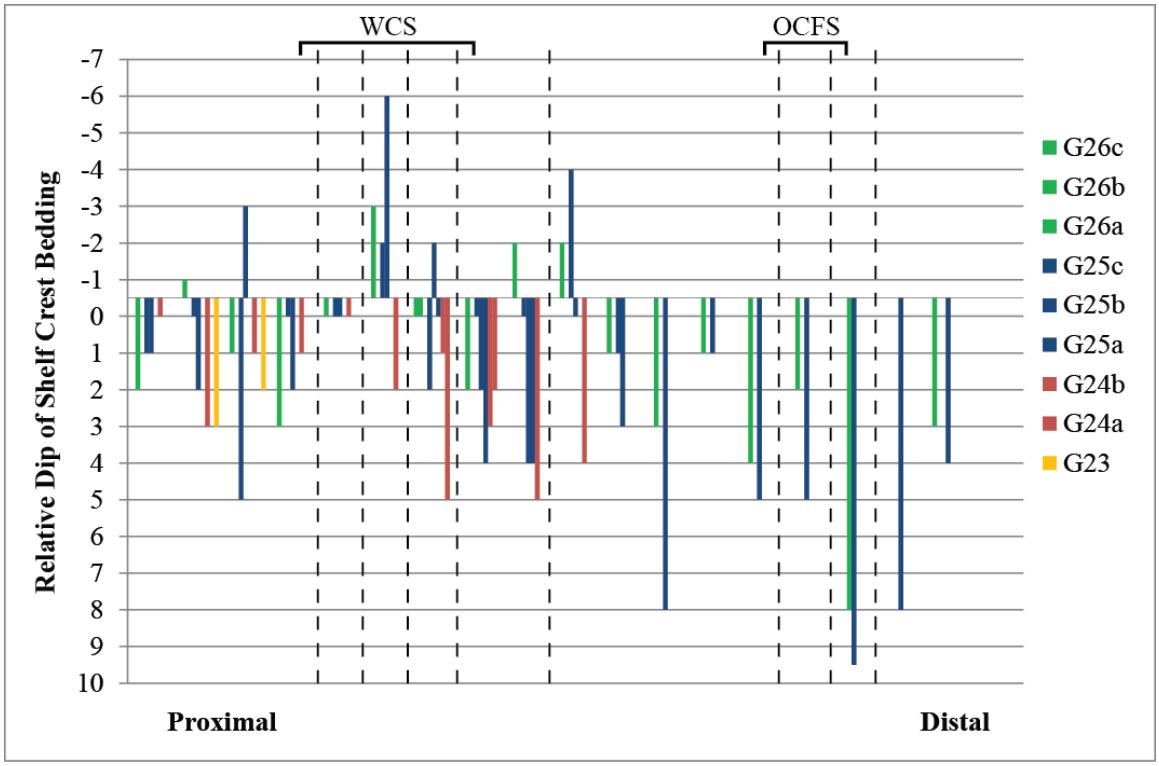

Figure 41: Graph of the temporal and spatial evolution of the low to moderate energy shelf crest facies tract dip. Here we can see that the bedding of this facies tract is generally not flat (average = 1.7 degrees basinward), basinward dip generally increases with age and distal position, and that shelfward-oriented dips typically occur in close proximity to faults. Positive values (downward oriented) indicate basinward dip while negative values (upward-oriented) indicate shelfward dip, note the non-zero value of the x-axis (-0.5 so that dips of 0 are visible). Bars color coded by age (HFS). Dashed vertical black lines indicate the location of faults (WCS = Walnut Canyon Syncline; OCFS = Ogle Cave Fault System).

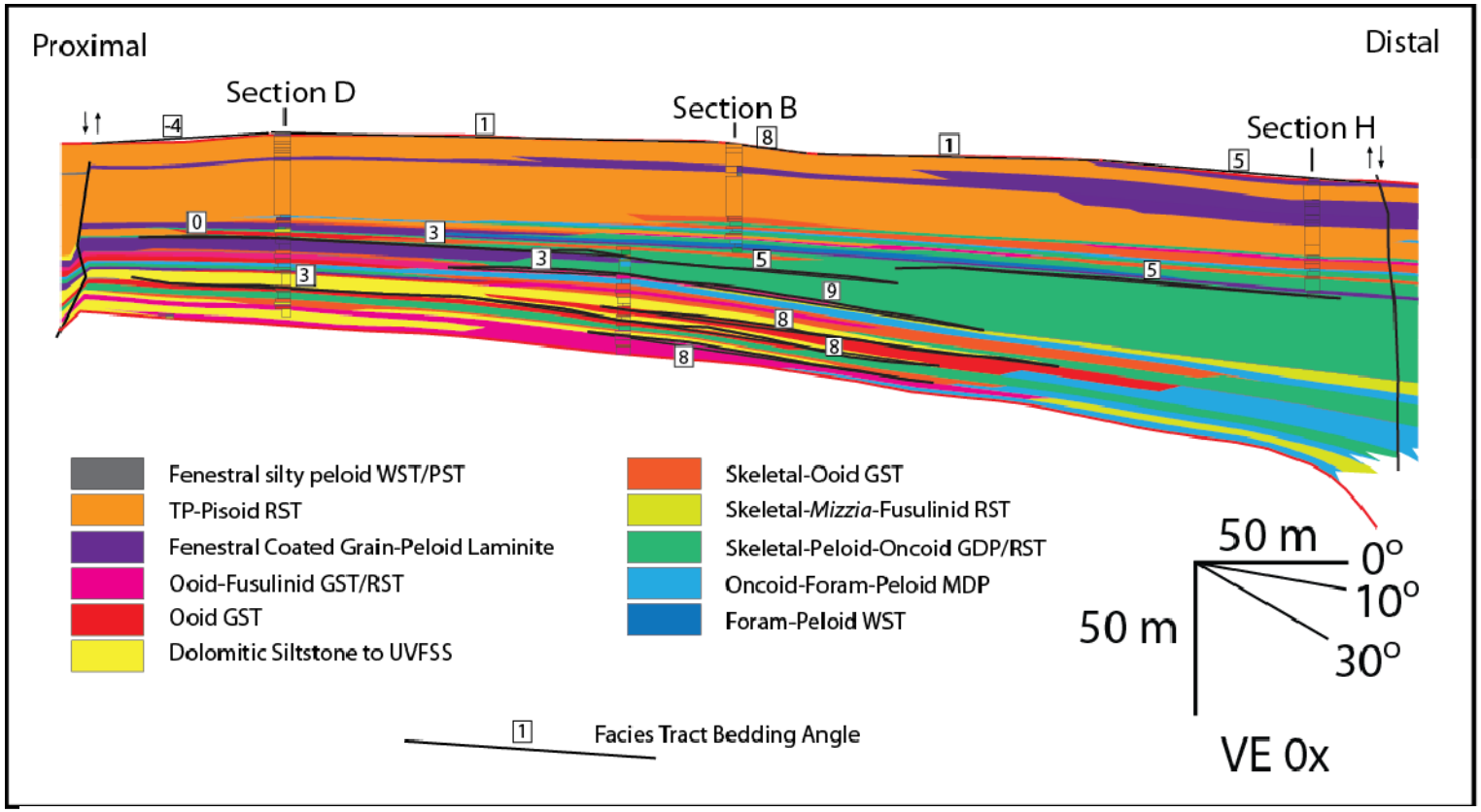

Figure 42: Close up window of the G25 HFS where changes in dip are observed along continuous surfaces crossing multiple facies tracts. These changes in dip cannot be explained structurally as they occur distant from faults. Note also the partitioning of steeper dips to more distal facies.

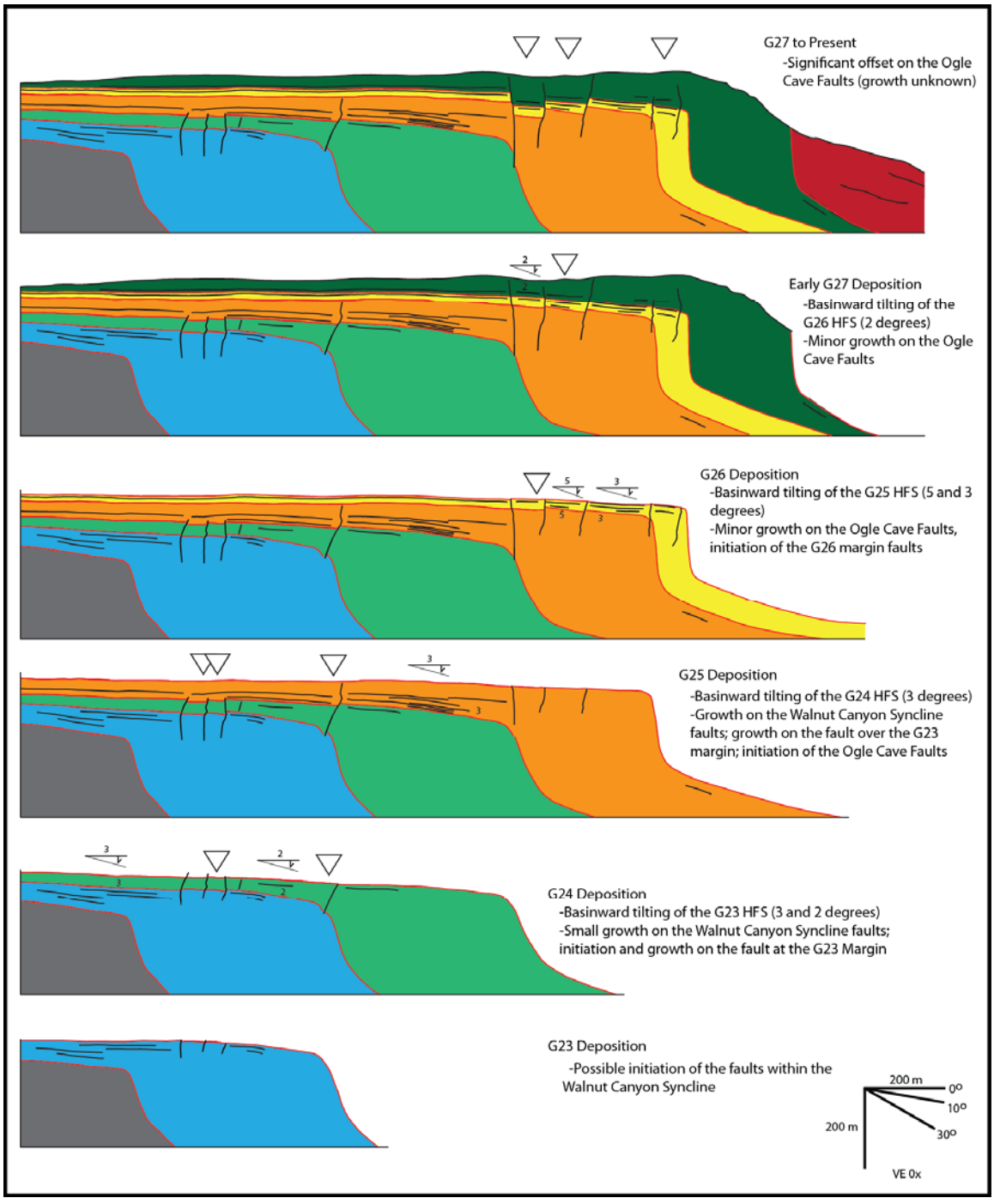
G27 to Present
-Significant offset on the Ogle Cave Faults (growth unknown)
Early G27 Deposition
-Basinward tilting of the G26 HFS (2 degrees)
-Minor growth on the Ogle Cave Faults
G26 Deposition
-Basinward tilting of the G25 HFS (5 and 3 degrees)
-Minor growth on the Ogle Cave Faults, initiation of the G26 margin faults
G25 Deposition
-Basinward tilting of the G24 HFS (3 degrees)
-Growth on the Walnut Canyon Syncline faults; growth on the fault over the G23 margin; initiation of the Ogle Cave Faults
G24 Deposition
-Basinward tilting of the G23 HFS (3 and 2 degrees)
-Small growth on the Walnut Canyon Syncline faults; initiation and growth on the fault at the G23 Margin
G23 Deposition
-Possible initiation of the faults within the Walnut Canyon Syncline
200 m
200 m
0°
10°
30°
VE 0x

Figure 43: Reconstruction of the geometric evolution from the G23 to the present. Note the preferential location of growth faults above and distally adjacent to the previous HFS's terminal margin, indicating fracture and fault development over that paleotopography and progressive progradation of younger deformation. This additionally shows that faults (triangles) were active during deposition (growth) while large-scale basinward rotation of a given HFS occurred following its deposition, preferentially tilting the facies distal to the underlying terminal margin.

DISCUSSION

The observed G23 to G25 HFS show hierarchical stacking of facies into cycles, cycle sets, and high frequency sequences which form an overall regressive trend (CS 13 highstand) from the G23-G25 HFS and initiate a transgressive trend (CS 14 TST) in the G26 HFS (Kerans and Tinker, 1999). Variation in accommodation conditions, largely controlled by paleotopography and eustasy, was the major driving factor in the spatial and temporal distribution of facies in the Yates-Capitan system. The resulting progradational reef-rimmed shelf-to-basin facies distribution was prone to syndepositional fracture and fault development which influenced depositional topography during exposure (Kosa and Hunt, 2005) and created a structural fabric for post-depositional deformation (basinward rotation). Below I address the distribution of the individual facies tracts in the quantified context of sequence stratigraphic position (facies proportions), P/A ratio, facies tract dip width, and facies tract bedding angle.

Facies Distributions

Siliciclastic Facies

Partitioning of siliciclastic-based cycles in the lower, transgressive portions of the G23, G24, and G25 is well documented in the literature and was a key facies for sequence identification (Tinker, 1996, 1998; Osleger, 1998; Osleger and Tinker, 1999) Figure 44). The presence of the sands represents significant facies tract offsets of proximal shelf sourced siliciclastics sharply overlying shelf crest and outer shelf carbonates (Tinker, 1996, 1998; Osleger, 1998; Osleger and Tinker, 1999). The observed increasing proportion of siliciclastics from the G23 to the G26 additionally supports the interpretation of low order accommodation loss approaching the G25/G26 boundary with major composite sequence-scale lowstand bypass and subsequent trapping of siliciclastics

across the shelf during the early CS 14 transgression (G26). Numerous siliciclastic-based cycles amalgamated to pure siliciclastics updip within the study area (24.1, 25.1, 25.3, 26.1, 26.2, and 26.6), most of which occurred at the base of their respective HFS. These sand-bounded wedges of shallowing-upward carbonates represent the transgressive incursion of shelf crest and outer shelf facies following major siliciclastic bypass, and notably do not develop the classic tepee-pisoid rudstone facies diagnostic of the low to moderate energy shelf crest. This phenomenon corroborates the aggradation-dependent model for tepee formation from Tinker (1998) and Kerans and Tinker (1999), as these cycles were likely too accommodation-limited to maintain a stable shoreline long enough for the formation of tepee structures.

The G26 HFS is additionally significant as its constituent cycles above the MFS contain a large percentage of siliciclastics, an observation unique to the G26 compared to the highstands of the lower HFSs. Here the higher proportion of siliciclastics in both the transgressive and highstand cycles simply indicates lower overall accommodation, such that the shelf during G26 deposition was never flooded sufficiently to cause major retrogradation of the middle shelf siliciclastic source.

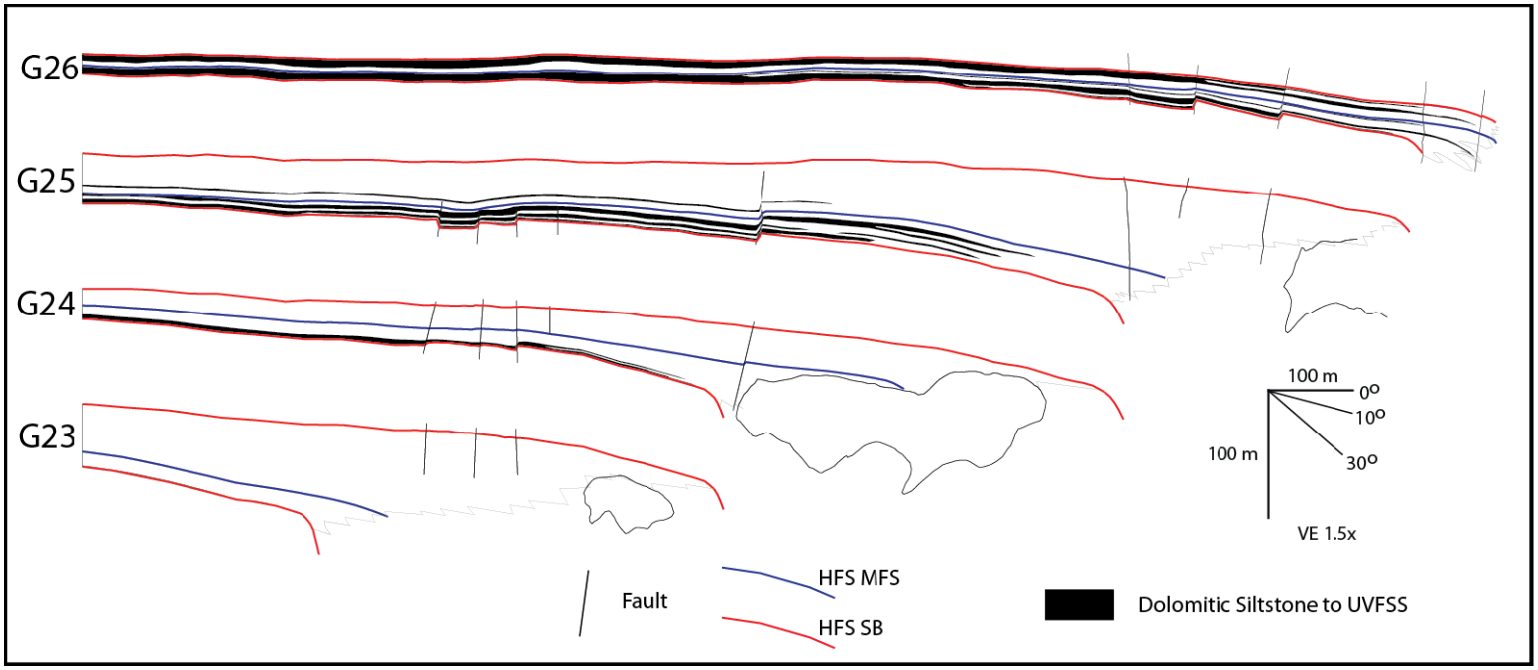

Figure 44: High frequency sequence-scale distributions of dolomitic siltstone to sandstone facies. Note the partitioning of this facies to the TST cycles of each HFS, with the exception of the G26 HST.

Middle Shelf Facies

Carbonate middle shelf facies were rare in the study area and appeared only at the top of the most proximal portions of cycles 25.5, 25.12 and 26.2. It is likely that much of the proximal portions of cycles 26.3-26.5 also contain middle shelf carbonate facies but clear separation from the shelf crest is impeded by common pisoid allochems and small tepee structures (~30 cm high). The appearance of these facies only in the G25 and G26 HFS (within the study area) is a result of both the distal location of observation as well as progressive progradation and expansion of the shelf crest from G23 to G25, with the middle shelf exposed only in the most proximal region prior to the CS boundary; and shelf crest contraction in the G26 following the CS boundary.

Low to Moderate Energy Shelf Crest Facies

The low to moderate energy shelf crest facies best developed in the late TST to HST of the G25 HFS (P/A = 5); here it exhibits the greatest amalgamation and facies dip width (Figure 45). The distal position of the study area limits the extent of these facies in the G23, as they appear only immediately beneath the G23/G24 sequence boundary. Within the observed extent of the G24 (P/A = 29), there is a relatively well balanced ratio of fenestral coated grain-peloid laminite and tepee pisoid rudstone, with the laminites prograding further basinward and more dominant in the HST than the tepee facies. Again, this supports the model of aggradation-dependent tepee formation (Tinker, 1996, 1998; Kerans and Tinker, 1999). The G25 is initially characterized by thin, laterally extensive fenestral coated grain-peloid laminites during the early TST and by the classic amalgamated tepee pisoid rudstone interval of the “Hairpin Dolomite” (Esteban and Pray, 1977) in the HST. As the G25 contains the most voluminous accumulation of the shallowest facies, its interpretation as the final HFS in the CS 13 is reasonable. However, the thickness of the tepee facies does suggest a significant amount of aggradation during

what should be an in-phase CS and HFS highstand. Previous authors have consequently included the G25 in the overlying CS 14 (Tinker, 1998), or suggested that too much relief had been constructed at the margin to allow for continued progradation (Osleger, 1998). This author favors the interpretation of relief-limited progradation coupled with an advantageous paleotopography set up by the underlying G24. The transgressed surface of the underlying G24 was largely constructed by shallow, flat-lying shelf crest sediments, directly over which the shelf crest of the G25 established. This provided a shallow, flat foundation on which new tepees formed during the transgressive to aggradational development of the G25.

As stated previously, the shelf crest of the G26 is dominated by the fenestral coated grain-peloid facies rather than tepee pisoid rudstone. Although shallow and high energy facies dominate this sequence, a robust shelf crest with large tepees did not develop as in the G25 due to the low relative aggradation (22 m in the G26 versus 69 m in G25) and the repeated exposure and bypass of siliciclastics.

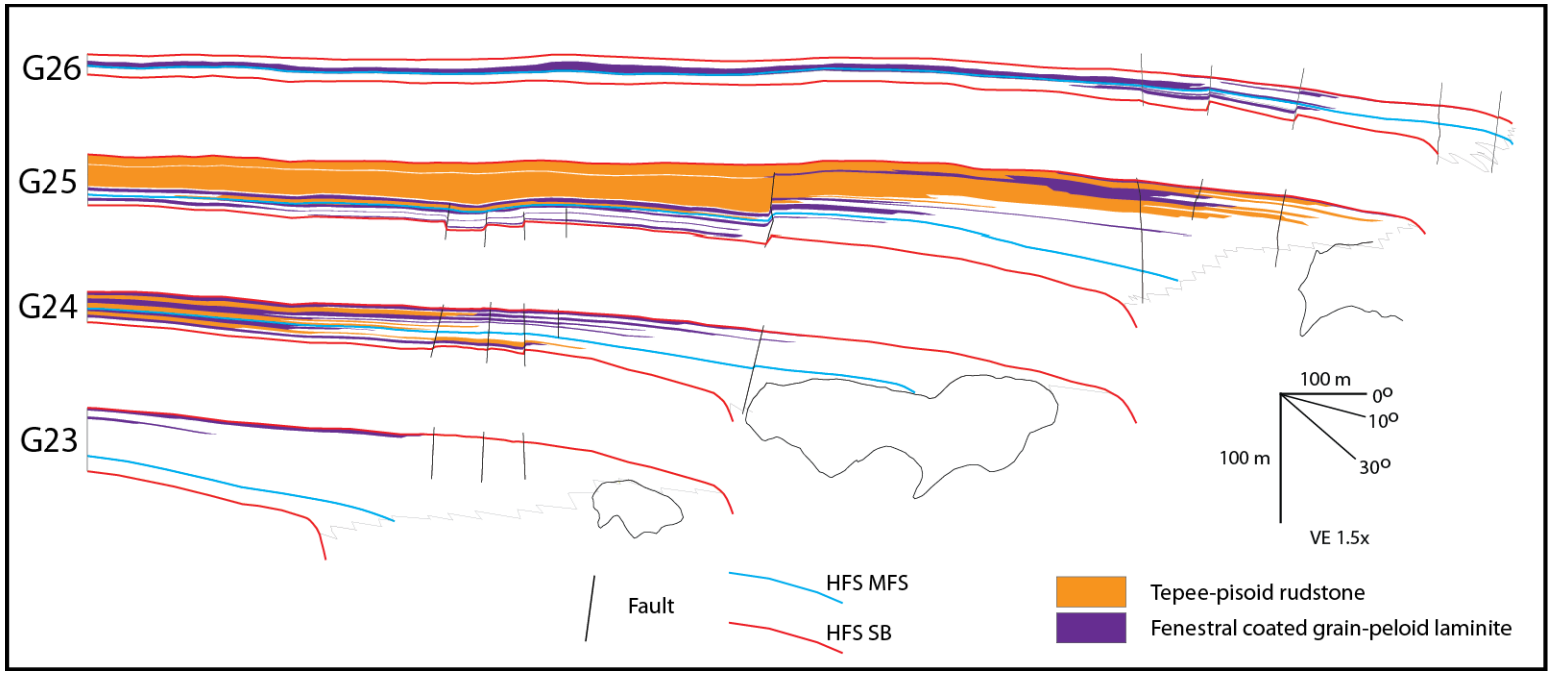

Figure 45: High frequency sequence-scale distribution of the low to moderate energy shelf crest facies. Note the well-developed, amalgamated tepee-pisoid rudstones in the G25 HST (P/A=5) compared to the thin, planar tepee-pisoid rudstones in the G24 HST (P/A =29). This facies tract occurs in the G23 HFS updip of the study area (Osleger, 1998).

High Energy Shelf Crest Facies

The ooid grainstones and ooid-fusulinid rudstone/grainstones of the high energy shelf crest track the seaward edge of the shelf crest and represent foreshore environments (Figure 46). Both facies are present in the G23-G25 HFS, while the G26 is dominated by ooid grainstones, likely due to the transition from the large, abundant fusulinid *Polydiexodina* to the smaller fusulinid *Codonofusiella extensa* at the CS 13/14 boundary. The two-dimensional stacking of this facies tract is largely reflective of the accommodation settings across the shelf and shows significant variation between the successive HFSs. The G23 HFS is characterized by initially aggradational foreshores within the study area which eventually thin and prograde upwards towards the sequence boundary. The G24 HFS contains initially amalgamated, aggradational ooid-fusulinid foreshores which backstep and thin following the MFS and progressively prograde after cycle 24.7. The occurrence of ooid grainstone foreshores increases distally, although the fusulinid facies dominate. The transgressive portion of the G25 HFS is again characterized by amalgamated, aggradational foreshores with roughly equal proportions of ooid grainstones and ooid-fusulinid rudstones. Following the G25 MFS the foreshore facies thin in dip width and thickness, then prograde significantly distal to the amalgamated tepee pisoid complex, where they reside nearly at the margin. Lastly, the high energy shelf crest facies of the G26 are dominated by ooid grainstones which developed in close proximity to the margin. These foreshores are aggradational to retrogradational through the MFS and subsequently prograde to the margin during the HST.

Overall, this facies tract best develops in aggradational to retrogradational, siliciclastic-based cycles in the early TST and in progradational cycles of the HST. The intra-sequence alternation between fusulinid-dominated and ooid-dominated foreshores is

interpreted to be controlled by storm energy and not generally related to accommodation. There is additionally a correlation between the G25 HFS's high P/A ratio (29) and the establishment of wide high energy shelf crest dip widths (Figure 40). This suggests that when aggradation was not sufficient to encourage tepee growth, wide progradational strand plains dominated; and that when tepees were present, these strand plains contracted distally, due potentially to a steeper gradient between the shelf crest and reef margin. Average bedding angles on this facies tract reflect a steeper dip (5.8 degrees) in all the observed sequences relative to the low to moderate energy shelf crest (1.7 degrees); this reflects a bathymetric steepening of the depositional profile.

High Energy Outer Shelf Facies

The high energy outer shelf facies were typically found in close proximity to each HFS's terminal margin (within ~700 m) and were slightly more prevalent (greater facies proportion) in the HFS HST's (Figures 39, 47). Dip widths of this facies tract were again greatest in the G24 HFS, indicating another positive correlation between high energy, grain-dominated fabrics and comparatively higher P/A ratios. There is not a distinct trend of facies partitioning between skeletal-ooid grainstones and skeletal-*Mizzia*-fusulinid rudstones as both facies occur throughout the G23-G26 HFSs, typically as distal cycle caps. In a dip perspective, the skeletal-ooid grainstones represent an active shoal facies which likely occurred in shallower water depths than the skeletal-*Mizzia*-fusulinid rudstones, a relationship reflected in most cycles where both facies are present. On a larger scale, the study area records the gradual increase in *Mizzia* green algae from the Seven Rivers into the Tansill, as documented by Babcock (1977) and Yurewicz (1977). The average bedding angle of this facies (6 degrees) is greater than but close to that of the high energy shelf crest (5.8 degrees), but is again considerably steeper than that of the

low to moderate energy shelf crest (1.7) suggesting a basinward-oriented bathymetric profile distal to the shelf crest.

Moderate to Low Energy Outer Shelf

The moderate to low energy outer shelf facies represent the gradational transition to deeper, lower energy facies proximal to the shelf margin. This facies tract was best developed at or near each HFS's MFS and in the underlying transgressive cycles (Figure 48). Cycle-scale facies tract dip widths record the transgressive-regressive nature of this facies distribution in the G24 through G26 (Figure 40). Prediction of this facies abundance is not directly linked to P/A ratio however, as the G26 shows the lowest ratio observed (P/A = 4) whose large relative value of aggradation could be interpreted to suggest wide low to moderate energy outer shelf development; which in reality was very poorly developed in terms of dip width (Figure 40). The average bedding angle of this facies tract is the greatest of those quantified (7.9 degrees) and the fabric likewise indicates the lowest depositional energy; these facts continue to support the basinward-dipping bathymetry of the shelf crest to shelf margin profile.

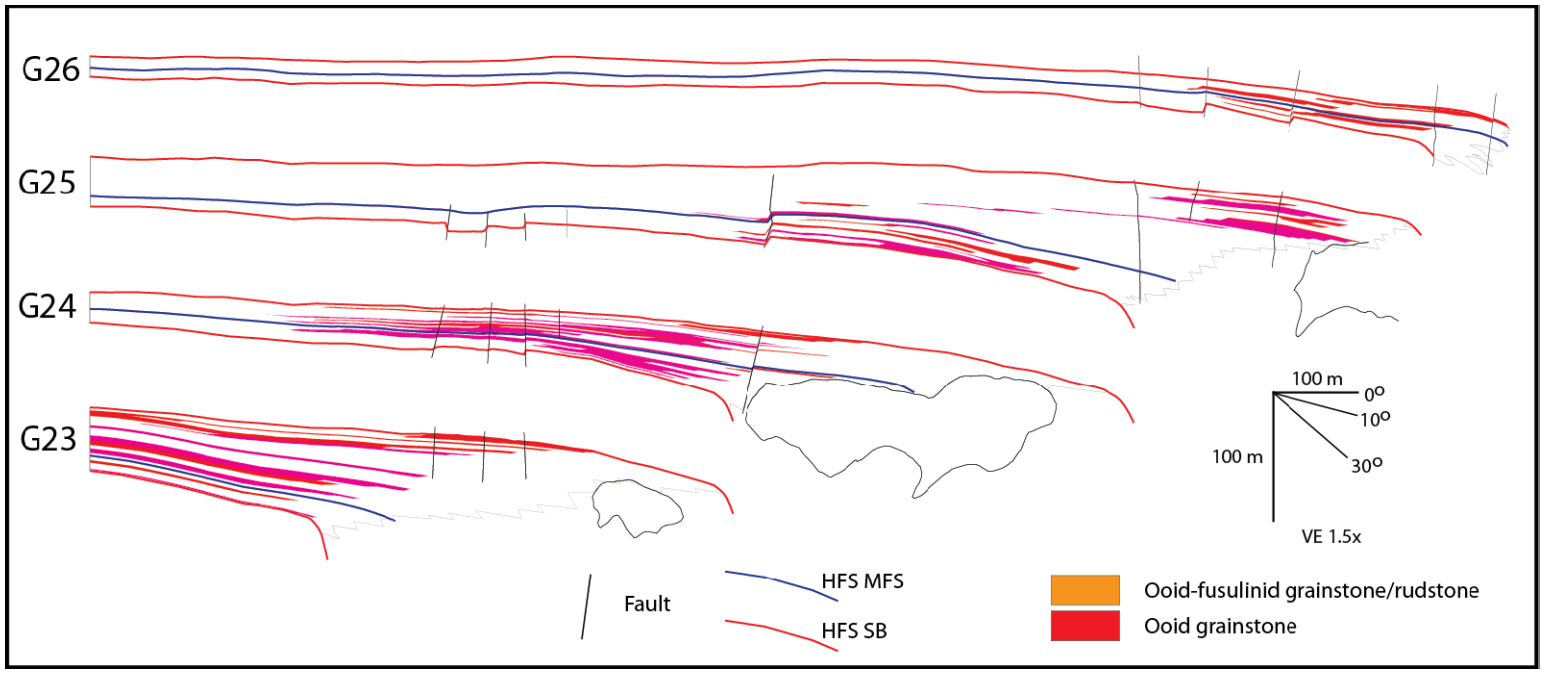

Figure 46: High frequency sequence scale distribution of high energy shelf crest facies. Note the aggradational stacking of these foreshore grainstones/rudstones during TST's and progradational stacking in HST's. Dip widths of these facies were also greater in the G24 versus the G25, likely due to the lack of an amalgamated tepee complex proximally.

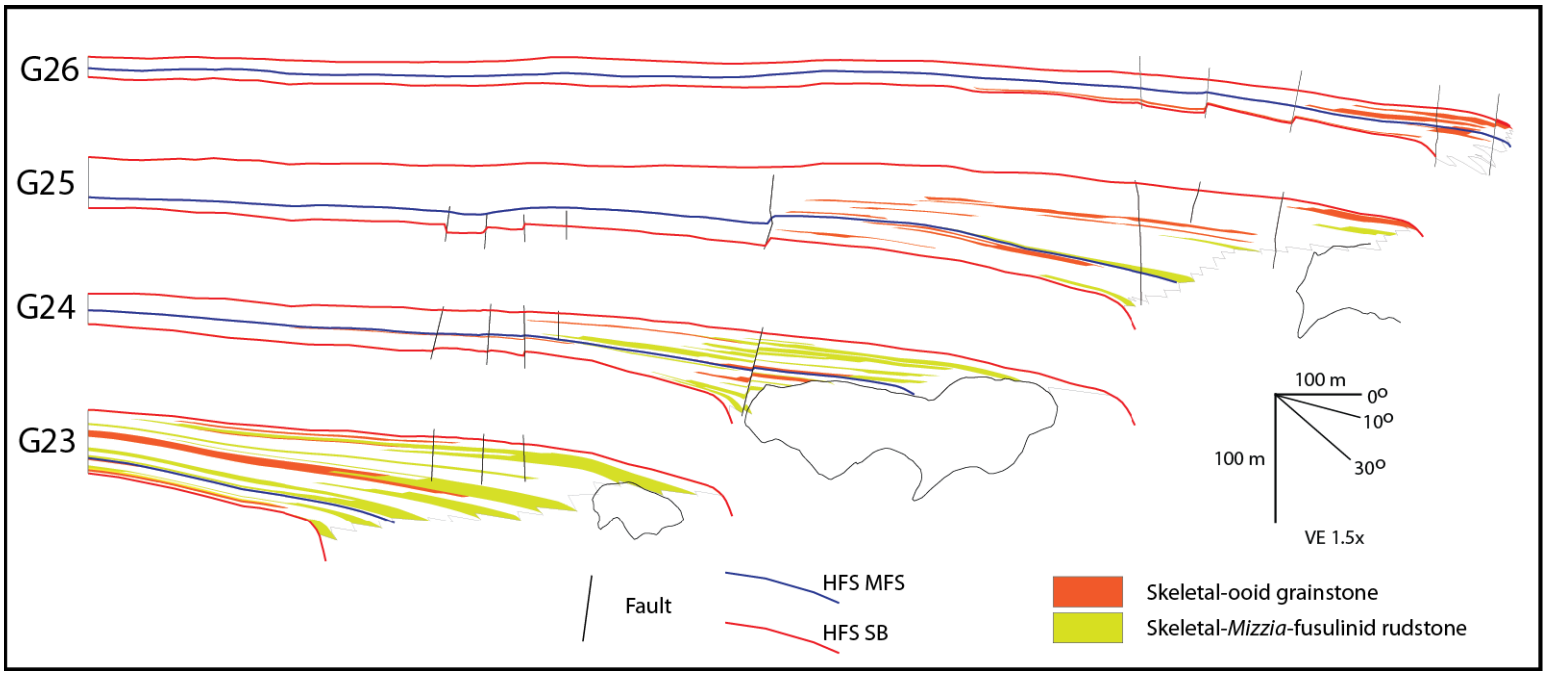

Figure 47: High frequency sequence scale distribution of high energy outer shelf facies. Note the subtle portioning into highstand cycles of each HFS, indicating progressively higher energy conditions on the outer shelf associated with accommodation loss.

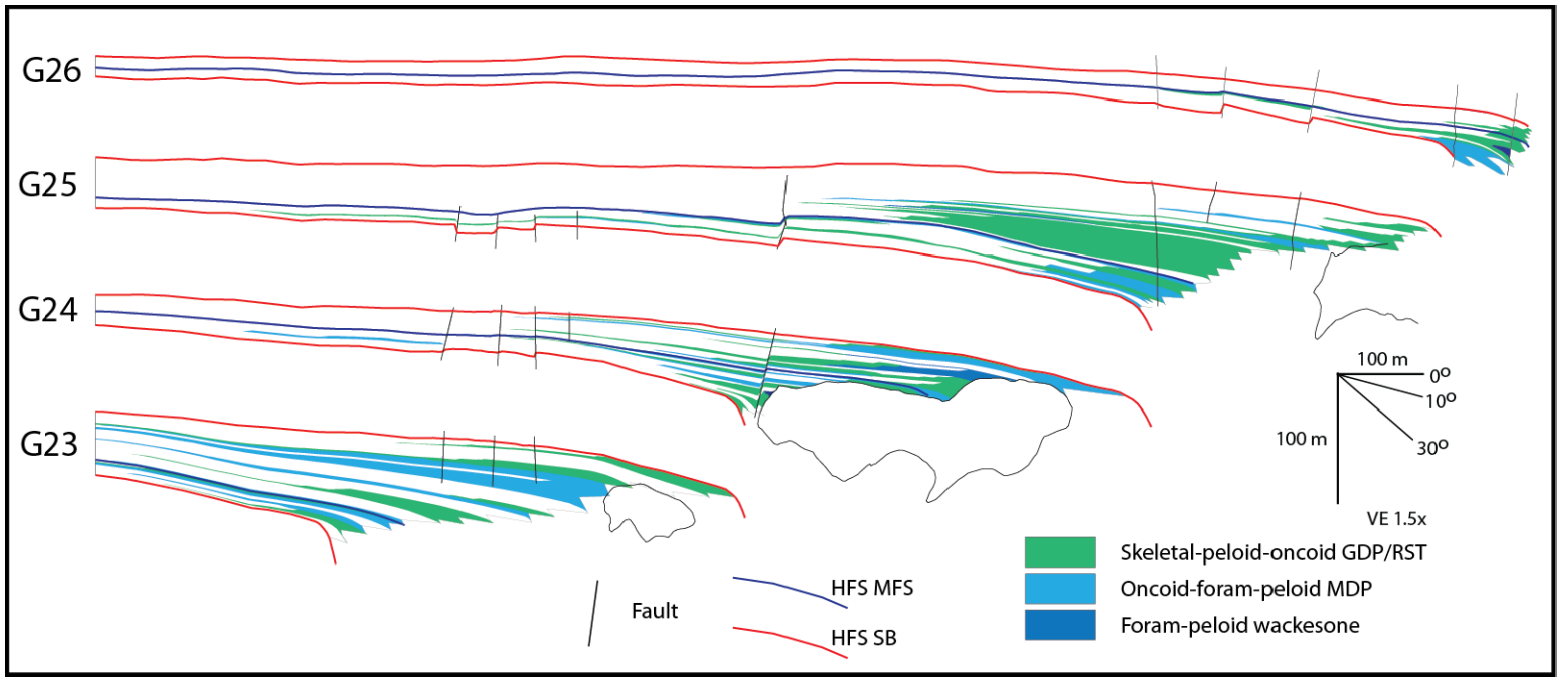

Figure 48: High frequency sequence scale distribution of moderate to low energy outer shelf facies. Note how the updip limit in each cycle roughly tracks the transgressive-aggradational-progradational pattern expected from hierarchical, cyclic changes in eustasy.

Sequence Geometry and Deformation

The facies tract bedding angles support contributions from depositional topography, local syndepositional structural deformation and later structural rotation (Figures 41, 42, 43). The documented HFS-scale structural deformation of faulting and subsequent basinward rotation is likely founded on the distribution of fractures, as some fractures eventually became faults and most rotated strata were fault-bound. The development of syndepositional fractures in the Yates-Capitan system was likely due to a combination of gravitational instability and differential compaction over antecedent topography (Kosa and Hunt, 2005; Frost and Kerans, 2009). Syndepositional fractures likely developed throughout the prograding and aggrading, early lithified high relief Capitan shelf margin. As the system initially aggraded above and then prograded beyond the underlying HFS's margin, stress from the compaction of underlying finer grained slope and basinal strata preferentially built on the fractures above and distally adjacent to the older, lithified margin (Kosa and Hunt, 2005). The accumulation of this extensional stress caused upward propagation of the shelf margin fractures into the mechanically weaker outer shelf facies tracts leading to displacement and growth on the fractures above the paleo-margin (Kosa and Hunt, 2005) (Figure 49). The development of these fractures and faults establishes conduits for fluid flow which bisect the surrounding cyclic stratigraphy (Melim, 1991; Hunt et al., 2002; Kosa and Hunt, 2005, 2006a, 2006b; Frost et al., 2010) Bedding geometry was significantly altered in close proximity (~50 m) to the growth faults during deposition (Hunt et al., 2002; Kosa et al., 2003; Hunt et al., 2005; Kosa and Hunt, 2005, 2006a, 2006b); however HFS-scale basinward rotation of strata typically occurred during the deposition of the overlying sequence (or in the lowstand hiatus between them), creating a progressive basinward-migration of younger deformational features. This model has a subtle, but new interpretation which places the

timing for large-scale rotation of strata between faults after the deposition of the rotated HFS, and emphasizes the combined facies/accommodation position control over fault development.

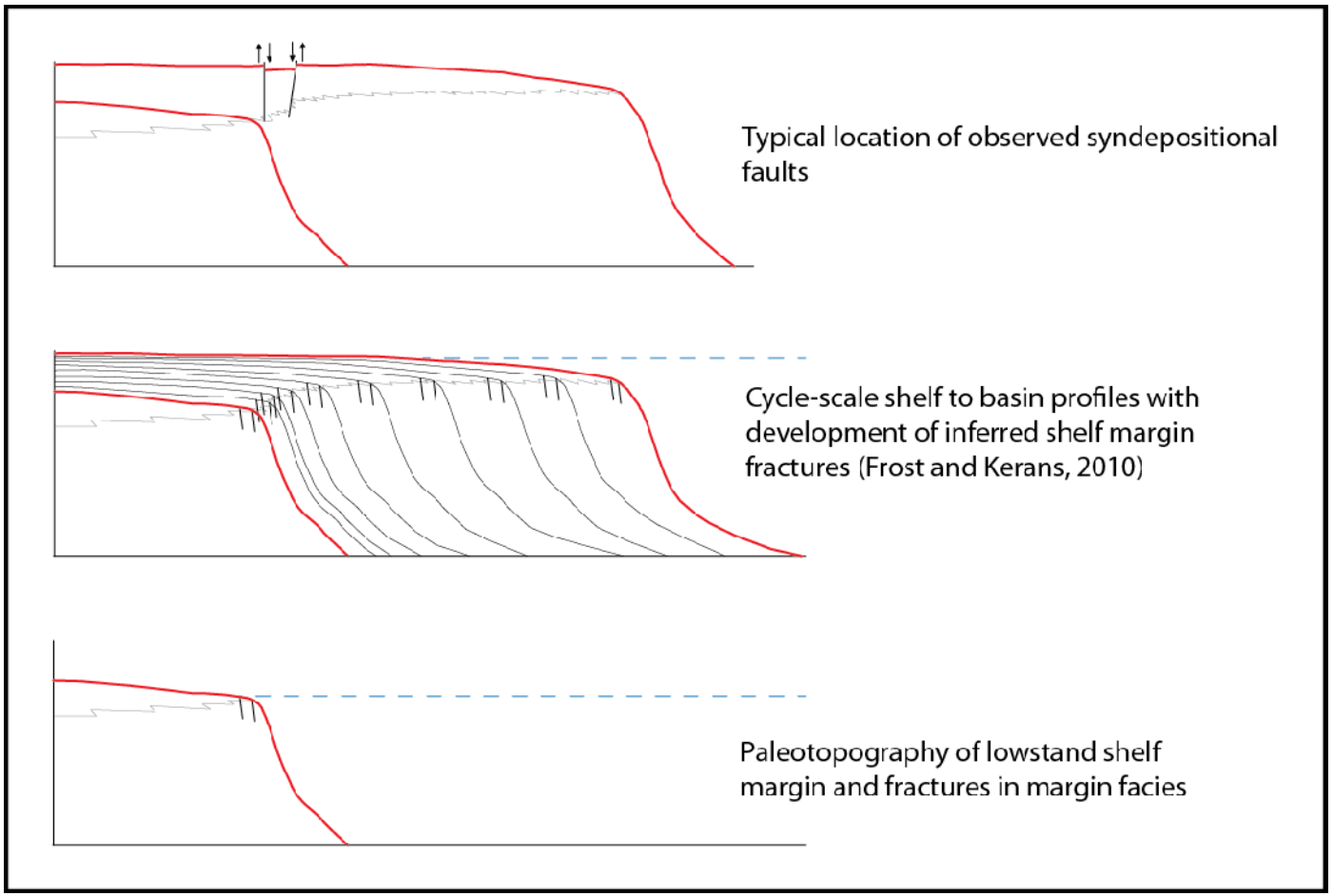

Figure 49: Conceptual model illustrating the potential role of syndepositional fractures in the shelf margin due to paleotopography and gravitational instability in the development of faults above and distally adjacent to HFS bounding shelf margins. The cycle stacking and linked position of the margin in the TST (aggradational) may serve to concentrate fractures above the older margin, where upward propagation and displacement are most likely to occur.

CONCLUSIONS

The G23 to G26 HFS demonstrate dynamic sedimentation and coupled structural deformation of a mixed carbonate-siliciclastic reef-rimmed shelf. The studied facies are best organized into a proximal to distal series of facies tracts: middle shelf, low to moderate energy shelf crest, high energy shelf crest, high energy outer shelf, moderate to low energy outer shelf, and shelf margin. Using integrated field and lidar data sets, it was possible to calculate progradation to aggradation ratios for each HFS, facies proportions, cycle-scale facies tract dip widths, and facies tract bedding angles. These quantified stratigraphic variables support the interpretation that facies character and distribution was largely controlled by eustatic changes in relative sea level, and that the current sequence stratigraphic framework provides a predictive organization in which facies partition. These data also support a marginal mound, basinward-dipping depositional profile from the low to moderate energy shelf crest to the shelf margin. The additional presence of syndepositional faults was found to locally influence the thickness of facies and their respective bedding angles, but most facies crossed faults, indicating that there was not significant bathymetric relief generated by the fault during deposition. In contrast to previous studies of syndepositional deformation in the Yates HFS, reconstruction of HFS-scale bedding angles shows that basinward rotation of strata between faults occurred following that sequence's deposition, not synchronously. Lastly, a model is proposed that links the stacking pattern of the shelf margin facies tract (and its gravitationally-induced syndepositional fractures) to the development of syndepositional faults above and distally adjacent to underlying shelf margins. This model emphasizing the facies and thereby eustatic control over initiation of structural deformation in the G23 to G26 high frequency sequences.

Appendix

Cycle #		HE SC Width (m)		HE OS Width (m)		MLE OS Width (m)
24.1		137		108		69
24.2		184		152		121
24.3		219		88		149
24.4		524		141		187
24.5		129		218		475
24.6		486		275		577
24.7		344		461		367
24.8		601		314		576
24.9		628		292		106
24.10		388		380		354
24.11		218		84		669
25.1		361		115		183
25.2		285		208		1050
25.3		227		0		159
25.4		229		232		228
25.5		339		297		641
25.6		0		116		403
25.7		84		151		479
25.8		0		117		518
25.9		143		254		487
25.10		206		400		579
25.11		214		82		522
25.12		171		98		289
25.13		230		0		123
24.14		123		154		0
26.1		83		521		112
26.2		245		76		236
26.3		279		0		0
26.4		171		87		444
26.5		177		209		101
26.6		183		181		38
26.7		165		0		0

Appendix A: Values of facies tract dip widths for the cycles of the G24-G26 HFS. HE SC = high energy shelf crest; HE OS = high energy outer shelf; MLE OS = moderate to low energy outer shelf. All dip widths in meters.

LME Shelf Crest					WCS	WCS				G23MF					OCFS	OCFS			GF
23		3	2																
24							5	2											
24	0	3	1	1	0	2	1	3	5	4									
25							0	4	4										
25	1	2	-3	2	0	-6	-2	2	4	0	3								
25	1	0	5	0	0	-2	2	0	0	-4	1	8	1	5	5	9.5	8	4	
26																8			
26	2	-1	1	3	0	-3	0	2	-2	-2	1	3	1	4	2				
26																		3	

HE Shelf Crest																			
23	3																		
23					2	4	6												
24											4								
25													8						
25											3	8	8						
25													8	8					
25												3	9						
26																		4	
26																5			
26																	5	9	
26																5			
26																			8

HE Outer Shelf																			
23	8																		
23	5																		
24											5								
26																			10
26																	4	4	

MLE Outer Shelf																			
23	4																		
23							9	16											
23								11											
24											5	9	9	9					
25												5							
25													5	5					

Appendix B: Facies tract dip angles classified by HFS (values along the same row are from the same lidar bedding surface) and dip position (left = proximal; right = distal). Negative values indicate a landward dip. LME = low to moderate energy; HE = high energy; MLE = moderate to low energy. WCS = horst block in Walnut Canyon Syncline; G23MF = position distally adjacent to the G23 margin fault; OCFS = horst block in the Ogle Cave fault system; GF = position distally adjacent to the faults above the G25 margin.

References

Andreason, M.W., 1992, Coastal siliciclastic sabkhas and related evaporative environments of the Permian Yates formation, North Ward-Estes field, Ward County, Texas: AAPG Bulletin, v. 76, p. 1735-1759.

Babcock, J.A., 1977, Calcareous algae, organic boundstones, and the genesis of the Upper Capitan Limestone (Permian, Guadalupian), Guadalupe Mountains, West Texas and New Mexico, *in* Hileman, M.E., and Mazzullo, S.J., eds., Upper Guadalupian Facies, Permian Reef Complex, Guadalupe Mountains, New Mexico and West Texas: 1977 Field Conference Guidebook, v. 1, Permian Basin Section SEPM, Publication 77–16, p. 3–44.

Babcock, J.A., and Yurewicz, D.A., 1989, The massive facies of the Capitan Limestone, Guadalupe Mountains, Texas and New Mexico, *in* Harris, P.M., and Grover, G.A., eds., Subsurface and Outcrop Examination of the Capitan Shelf Margin, Northern Delaware Basin: SEPM, Core Workshop 13, p. 365–372.

Bambach, R.K., Scotese, C.R., and Ziegler, A.M., 1980, Before Pangea: the geographies of the Paleozoic world: American Scientist, v. 68, p. 26–38.

Bebout, D.G., and Kerans, C., eds., 1993, Guide to the Permian Reef Geology Trail, McKittrick Canyon, Guadalupe Mountains National Park, West Texas: Texas Bureau of Economic Geology, Guidebook 26, 48 p.

Bellian, J.A., Kerans, C., Jennette, D.C., 2005, Digital Outcrop Models: Applications of terrestrial scanning lidar technology in stratigraphic modeling: Journal of Sedimentary Research, v. 75, p. 166-176.

Borer, J.M., and Harris, P.M., 1989, Depositional facies and cycles in Yates Formation outcrops, Guadalupe Mountains, New Mexico, *in* Harris, P.M., and Grover, G.A., eds., Subsurface and Outcrop Examination of the Capitan Shelf Margin, Northern Delaware Basin: SEPM, Core Workshop 13, p. 305–317.

Borer, J.M., and Harris, P.M., 1991a, Lithofacies and cyclicity of the Yates Formation, Permian Basin: Implications for reservoir heterogeneity: AAPG Bulletin, v. 75, p. 726–779.

Borer, J.M., and Harris, P.M., 1991b, Depositional facies and model for mixed siliciclastics and carbonates of the Yates Formation, Permian Basin, *in* Lomando A.J., and Harris, P.M., eds., Mixed carbonate-silicilastic sequences: SEPM Core Workshop 15, p. 1-133.

Borer, J.M., and Harris, P.M., 1995, Computer simulation of the Yates formation (Permian Delaware basin) sequence stratigraphy and shelf to basin correlation implications, *in* Martin, R.L. ed., In Search of New Permian Basin Oil and Gas Fields: Using Today's Technologies and Tomorrows Ideas for Exploration, Development, and 3D Seismic in a Mature Basin: Midland, West Texas Geological Society Symposium, Publication 95-98, p. 111-132

Brown, A.A., and Loucks, R.G., 1993, Toe of slope, *in* Bebout, D.G., and Kerans, C., eds., Guide to the Permian Reef Geology Trail, McKittrick Canyon, Guadalupe Mountains National Park, West Texas, Guidebook 26: Austin, Bureau of Economic Geology, University of Texas, p. 5-13.

Candelaria, M.P., 1982, Sedimentology and depositional environment of Upper Yates Formation siliciclastics (Permian, Guadalupian), Guadalupe Mountains, southeast New Mexico [unpublished M.S. thesis]: University of Wisconsin, Madison, Wisconsin, 267 p.

Candelaria, M.P., 1989, Shallow marine sheet sandstones, upper Yates Formation, Northwest Shelf, Delaware Basin, New Mexico, *in* Harris, P.M., and Grover, G.A., eds., Subsurface and Outcrop Examination of the Capitan Shelf Margin, Northern Delaware Basin: SEPM Core Workshop, n. 13, p. 319-324.

Dunham, R. J., 1969, An environmental re-interpretation of the Permian evaporite/carbonate shelf sediments of the Guadalupe Mountains: GSA Bulletin, v. 80, p. 2503-2562.

Dunham, R.J., 1972, Capitan Reef, New Mexico and Texas: facts and questions to aid interpretation and group discussion: SEPM, Permian Basin Section, Publication 72–14, 291 p.

Esteban, M., and Pray, L.C., 1977, Locality Guide, Stop I, Introduction to strata of the shelf crest, inner Walnut Canyon and Carlsbad Caverns area, Upper Yates and Lower Tansill formations, *in* Pray, L.C., and Esteban, M., eds., Upper Guadalupian Facies, Permian Reef Complex, Guadalupe Mountains, New Mexico and West Texas, Volume 2, Road logs and locality guides (1977 Field Conference Guidebook): Midland, Texas, Permian Basin Section SEPM, Guidebook Publication 77-16, p. G87–G90.

Esteban, M., and Pray, L.C., 1983, Pisoids and pisolite facies (Permian), Guadalupe Mountains, New Mexico and West Texas, *in* Peryt, T.M., ed., Coated Grains: New York, Springer-Verlag, p. 503–537.

Fischer, A.G., and Sarnthein, M., 1988, Airborne silts and dune-derived sands in the Permian of the Delaware Basin: Journal of Sedimentary Petrology, v. 58, p. 637–643.

Frost, E.L., III, and Kerans, C., 2009, Platform-margin trajectory as a control on syndepositional fracture patterns, Canning Basin, Western Australia: Journal of Sedimentary Research, v. 79, p. 44–55.

Frost, E.L., III, and Kerans, C., 2010, Controls on syndepositional fracture patterns, Devonian reef complexes, Canning Basin, Western Australia: Journal of Structural Geology, v. 32, p. 1231-1249.

Frost, E.L., III, Budd, D.A., Kerans, C., and Allwardt, T., 2010, Syndepositional fault and fracture control on diagenetic fluid-flow, Tansill carbonates (Permian), Dark Canyon, Guadalupe Mountains, New Mexico, AAPG Annual Convention abstract, Search and Discovery, n. 90104.

Garber, R.A., Grover, G.A., and Harris, P.M., 1989, Geology of the Capitan shelf margin—subsurface data from the northern Delaware basin, *in* Harris, P.M., and Grover, G.A., eds., Subsurface and Outcrop Examination of the Capitan Shelf Margin, Northern Delaware Basin, SEPM, Core Workshop 13, p. 3–269.

Harris, P.M., and Saller, A.H., 1999, Subsurface expression of the Capitan depositional system and implications for hydrocarbon reservoirs, northeastern Delaware Basin, in Saller, A.H., Harris, P.M., Kirkland, B.L., and Mazzullo, S.J., eds., Geologic framework of the Capitan Reef, SEPM, Special Publication 65, p. 37–49.

Harwood, G.M., and Kendall, A.C., 1999, Reef margin collapse, gully formation and filling within the Permian Capitan Reef: Carlsbad Caverns, New Mexico, USA: Sedimentology, v. 46, p. 443–461.

Hayes, P. T., 1964, Geology of the Guadalupe Mountains, New Mexico: U.S. Geological Survey Professional Paper 446, 69 p.

Haynes, J., 1981, Foraminifera: New York, Wiley, 433 p.

Hillgartner, H., Dupraz, C., and Hug, W., 2001, Microbially induced cementation of carbonate sands: Are micritic meniscus cements good indicators of vadose diagenesis?: Sedimentology, v. 48, p. 117-131.

Hunt, D., Fitchen, W.M., Swarbrick, R., and Allsop, T., 1995. Differential compaction as a primary control of sequence architecture and development in the Permian Basin: geological significance and potential as a hydrocarbon exploration model. In:

Garber, R.F., Lindsay, R.F. eds., Wolfcampian –Leonardian Shelf Margin Facies of the Sierra Diablo: Seismic Models for Subsurface Exploration, West Texas Geological Society Publications, v. 95– 97, p. 83– 104.

Hunt, D.W., and Fitchen, W.M., 1999, Compaction and the dynamics of carbonate platform development; insights from the Permian Delaware and Midland basins; southeastern New Mexico and West Texas, U.S.A., *in* Harris, P.M., Saller, A.H., and Simo, J.A., eds., Advances in Carbonate Sequence Stratigraphy; Application to Reservoirs, Outcrops and Models, SEPM, Special Publication 63, p. 75–106.

Hunt, D.W., Fitchen, W.M., and Kosa, E., 2002, Syndepositional deformation of the Permian Capitan Reef carbonate platform, Guadalupe Mountains, New Mexico, USA: Sedimentary Geology, v. 154, p. 89–126.

Hunt D.W., Kosa, E., Simo, A.J., and Piccoli, L., 2005, Synsedimentary deformation of the upper Permain Capitan reef carbonate platform, New Mexico: AAPG 2005 Annual Convention, abstract with poster, v. 14, p. A65.

Hurley, N.F., 1978, Facies mosaic of the lower Seven Rivers Formation (Permian), North McKittrick Canyon, Guadalupe Mountains, New Mexico [unpublished M.S. thesis]: University of Wisconsin, Madison, Wisconsin, 198 p.

Hurley, N.F., 1989, Facies mosaic of the lower Seven Rivers Formation, McKittrick Canyon, New Mexico, in Harris, P.M., and Grover, G.A., eds., Subsurface and Outcrop Examination of the Capitan Shelf Margin, Northern Delaware Basin, SEPM, Core Workshop 13, p. 325–346.

Irving, E., 1979, Pole positions and continental drift since the Devonian, in McElhinny, M.W., ed., The Earth; Its Origin, Structure and Evolution: London, U.K., Academic Press, p. 567–590.

Jacka, A.D., Thomas, C.M., Beck, R.H., Williams, K.W., and Harrison, S.C., 1972, Guadalupian depositional cycles of the Delaware Basin and Northwest Shelf, *in* Elam, J.G., and Chuber, S., eds., Cyclic Sedimentation in the Permian Basin, 2nd Edition: West Texas Geological Society, Publication 69-56, p. 152–196.

Janson, X., Kerans, C., Bellian, J.A., and Fitchen, W.M., 2007, Three-dimensional geological and synthetic seismic model of Early Permian redeposited basinal carbonate deposits, Victorio Canyon, West Texas, AAPG Bulletin, v. 91, p. 1405-1436.

Jagnow, D.H., 1979, Cavern Development in the Guadalupe Mountains: Columbus, Ohio, Cave Research Foundation, 55 p.

Kendall, C.G.St.C., 1969, An environmental re-interpretation of the Permian evaporite/carbonate shelf sediments of the Guadalupe Mountains: Geological Society of America, Bulletin, v. 80, p. 2503–2526.

Kerans, C., Fitchen, W.M., Gardner, M.H., Sonnenfeld, M.D., Tinker, S.W., and Wardlaw, B.R., 1992, Styles of sequence development within uppermost Leonardian through Guadalupian strata of the Guadalupe Mountains, Texas and New Mexico, *in* Mruk, D.H., and Curran, B.C., eds., Permian Basin Exploration and Production Strategies: Applications of Sequence Stratigraphic and Reservoir Characterization Concepts: West Texas Geological Society, Symposium 92–91, p. 1–7.

Kerans, C., and Harris, P.M., 1992, Relative sea level record of Yates and Tansill Formation shelf facies, Permian reef geology trail: implications for platform development (abstract): American Association of Petroleum Geologists, Annual Convention, Book of Abstracts, v. 1, p. 65.

Kerans, C., and Harris, P.M., 1993, Outer shelf and shelf crest, *in* Bebout, D.G., and Kerans, C., eds., Guide to the Permian Reef Geology Trail, McKittrick Canyon, Guadalupe Mountains National Park, West Texas: Texas Bureau of Economic Geology, Guidebook 26, p. 32–42.

Kerans, C., Lucia, F.J., Senger, R.K., 1994, Integrated characterization of carbonate ramp reservoirs using Permian San Andres Formation outcrop analoges: AAPG Bulletin, v. 78, p. 181-216.

Kerans, C., and Fitchen, W.M., 1995, Sequence hierarchy and facies architecture of a carbonate-ramp system: San Andres Formation of the Algerita escarpment and western Guadalupe mountains, West Texas and New Mexico: Texas Bureau of Economic Geology, Report of Investigations 235, 86 p.

Kerans, C., and Tinker, S., 1999, Extrinsic stratigraphic controls on development of the Capitan reef complex, *in* Saller, A.H., Harris, P.M., Kirkland, B.L., and Mazzullo, S.J., eds., Geologic framework of the Capitan Reef, SEPM, Special Publication 65, p. 15–36.

Kirkland-George, B.L., 1992, Distinctions between reefs and bioherms based on studies of fossil algae *Mizzia*, Permian Capitan Reef complex (Guadalupe Mountains, Texas and New Mexico) and *Eugonopllyllum*, Pennsylvanian Holder Formation (Sacramento Mountais, New Mexico) [unpublished Ph D dissertation]: Louisiana State University, Baton Rouge, Louisiana, 156 p.

Kirkland, B.L., Longacre, S.A., and Stoudt, E.L., 1993, Reef, *in* D. Bebout, and Kerans, C., eds., Guide to the Permian Reef Geology Trail, McKittrick Canyon, Guadalupe Mountains National Park, west Texas, The University of Texas, Bureau of Economic Geology, Guidebook 26, p. 23–31.

Kirkland, B.L., Dickson, J.A.D., Wood, R.A., and Land, L.S., 1998, Microbialite and microstratigraphy: The origin of encrustations in the middle and upper Capitan Formation, Guadalupe Mountains, Texas and New Mexico, U.S.A.: Journal of Sedimentary Research, v. 68, p. 956-969.

Kosa, E., Hunt, D.W., Fitchen, W.M., Bockel-Rebelle, M.-O., and Roberts, G., 2003, The heterogeneity of paleocavern systems developed along syndepositional faults; Upper Permian Capitan platform, New Mexico, USA, in Ahr, W.M., Harris, P.M., Morgan, W.A., and Somerville, I.D., eds., Permo-Carboniferous Carbonate Platforms and Reefs: SEPM, Special Publication 78, American Association of Petroleum Geologists, Memoir 83, p. 291–322.

Kosa, E., and Hunt, D.W., 2005, Growth of syndepositional faults in carbonate strata: Upper Permian carbonate platform, New Mexico, USA: Journal of Structural Geology, v. 27, p. 1069-1094.

Kosa, E., and Hunt, D.W., 2006a, Heterogeneity in fill and properties of karst-modified syndepositional faults and fractures: Upper Permian Capitan Platform, New Mexico, USA: Journal of Sedimentary Research, v. 76, p. 131-151.

Kosa, E., and Hunt, D.W., 2006b, The effect of syndepositional deformation within the Upper Permian Capitan Platform of the speleogenesis and geomorphology of the Guadalupe Mountains, New Mexico, USA: Geomorphology, v. 78, p. 279-308.

King, P. B., 1948, Geology of the southern Guadalupe Mountains, Texas: U.S. Geol. Survey Prof Paper 215, 183 p.

Lambert, L.L., Wardlaw, B.R., Nestell, M.K., and Nestell, G.P., 2002, Latest Guadalupian (Middle Permian) conodonts and foraminifers from West Texas: Micropaleontology, v. 48, p. 343–364.

Longley, A.J., 1999, Differential compaction and its effects on the outer shelf of the Permian Capitan reef complex, Guadalupe Mountains, New Mexico, *in* Saller, A.H., Harris, P.M., Kirkland, B.L., and Mazzullo, S.J., eds., Geologic Framework of the Capitan Reef, SEPM, Special Publication 65, p. 85–105.

Mazzullo, S.J., Mazzullo, J., and Harris, P.M., 1985, Eolian origin of quartzose sheet sands in Permian shelf facies, Guadalupe Mountains (abstract), *in* Cunningham,

B.K., and Hedrick, C.L., eds., Permian Carbonate/Clastic Sedimentology, Guadalupe Mountains: Analogs for Shelf and Basin Reservoirs: SEPM, Permian Basin Section, Publication 85-24, p. 71.

Mazzullo, S.J., and Cys, J.M., 1977, Submarine cements in Permian boundstones and reef-associated rocks, Guadalupe Mountains, West Texas and southeastern New Mexico, *in* Hileman, M.E., and Mazzullo, S.J., eds., Upper Guadalupian Facies, Permian Reef Complex, Guadalupe Mountains, New Mexico and West Texas: SEPM, Permian Section, Publication 77-16, 1977 Field Conference Guidebook, p. 151-200.

Meissner, F.F., 1972, Cyclic sedimentation in Middle Permian strata of the Permian Basin, *in* Elam, J.G., and Chuber, S., eds., Cyclic Sedimentation in the Permian Basin, 2nd Edition: West Texas Geological Society, Publication 72-60, p. 203–232.

Melim, L.A., 1991, The origin of dolomite in the Permian (Guadalupian) Capitan Formation, Delaware Basin, West Texas and New Mexico: Implications for dolomitization models [unpublished Ph.D. thesis]: Southern Methodist University, Dallas, Texas, 200 p.

Melim, L.A., and Scholle, P.A., 1995, The forereef facies of the Permian Capitan Formation: the role of sediment supply versus sea-level changes: Journal of Sedimentary Research, v. 65, p. 107–118.

Mitchum, R.M, Jr, and Van Wagoner, J.C., 1991, High-frequency sequences and their stacking patterns: sequence-stratigraphic evidence of high-frequency eustatic cycles, *in* Biddle, K.T., and Schlager, W., eds., The Record of Sea-Level Fluctuations: Sedimentary Geology, v. 70, p. 131–160.

Mruk, D.H., and Bebout, D.G., 1993, Slope, *in* Bebout, D.G., and Kerans, C., eds., Guide to the Permian Reef Geology Trail, McKittrick Canyon, Guadalupe Mountains National Park, West Texas, The University of Texas, Bureau of Economic Geology, Guidebook 26, p. 32–43.

Mutti, M., and Simo, J.A., 1993, Stratigraphic patterns and cycle-related diagenesis of Upper Yates Formation, Permian, Guadalupe Mountains, *in* Loucks, R.G., and Sarg, J.F., eds., Carbonate Sequence Stratigraphy: Recent Developments and Applications: AAPG, Memoir 57, p. 515–534.

Neese, D.A., and Schwartz, A.H., 1977, Facies mosaic of the upper Yates and lower Tansill Formations, Walnut and Rattlesnake canyons, Guadalupe Mountains, New Mexico, *in* Hileman, M.E., and Mazzullo, S.J., eds., Upper Guadalupian Facies,

Permian Reef Complex, Guadalupe Mountains, New Mexico and West Texas: SEPM, Permian Section, Publication 77-16, 1977 Field Conference Guidebook, p. 437–450.

Neese, D.A., 1989, Peritidal facies of the Guadalupian shelf crest, Walnut Canyon, New Mexico, *in* Harris, P.M., and Grover, G.A., eds., Subsurface and Outcrop Examination of the Capitan Shelf Margin, Northern Delaware Basin, SEPM, Core Workshop 13, p. 295-304.

Newell, N. D., J. K. Rigby, A. G. Fischer, A. J. Whiteman, J. E. Hickox, and J. S. Bradley, 1953, The Permian reef complex of the Guadalupe Mountains region, Texas and New Mexico— a study in paleoecology: San Francisco. California, W. H. Freeman, 236 p.

Osleger, D.A., 1998, Sequence architecture and sea level dynamics of late Permian shelfal facies, Guadalupe Mountains, southern New Mexico: Journal of Sedimentary Research, v. 68, p. 327–346.

Osleger, D.A., and Tinker, S.W., 1999, Three-dimensional architecture of upper Permian high-frequency sequences, Yates–Capitan shelf margin, Permian basin, USA, *in* Harris, P.M., Saller, A.H., Simo, T., and Handford, R., eds., Advances in Carbonate Sequence Stratigraphy—Application to Reservoirs, Outcrops, and Models: SEPM, Special Publication 63, p. 169-185.

Phelps, R.M., and Kerans, C., 2007, Architectural Characterization and Three-Dimensional Modeling of a Carbonate Channel–Levee Complex: Permian San Andres Formation, Last Chance Canyon, New Mexico, U.S.A.: Journal of Sedimentology, v.77, p. 939-964.

Phelps, R.M., Kerans, C., Scott, S.Z., and Janson, X., 2008, Three-dimensional modeling and sequence stratigraphy of a carbonate ramp-to-shelf transition, Permian Upper San Andres Formation: Sedimentology, v. 55, p. 1777-1813.

Playton, T.E., 2008, Characterization, variations, and controls of reef-rimmed carbonate foreslopes [unpublished Ph.D. dissertation], The University of Texas at Austin, Austin, TX, 302 p.

Pray, L.C., and Esteban, M., 1977, Upper Guadalupian facies, Permian reef complex, Guadalupe Mountains, New Mexico and west Texas: SEPM, Permian Section, Publication 77- 16, 1977 Field Conference Guidebook, vol. 2, 194 p.

Pyles, D.R., Jennette, D.C., Tomasso, M., Beaubouef, R.T., and Rossen, C., 2010, Concepts learned from a 3D outcrop of a sinuous slope channel complex: Beacon

Channel Complex, Brushy Canyon Formation, West Texas, U.S.A.: Journal of Sedimentary Research, v. 80, p. 67-96.

Rankey, E.C., and Lehrmann, D.J., 1996, Anatomy and origin of toplap in a mixed carbonate– clastic system, Seven Rivers Formation (Permian, Guadalupian), Guadalupe Mountains, New Mexico, USA: Sedimentology, v. 43, p. 807–826.

Resor, P.G., and Flodin, E.A., 2010, Forward modeling synsedimentary deformation associated with a prograding steep-sloped carbonate margin: Journal of Structural Geology, v. 32, p. 1187-1200.

Ross, C.A., 1978, Late Pennsylvanian and Early Permian sedimentary rocks and tectonic setting of the Marathon Geosyncline, *in* Mazzullo, S.J., ed., Tectonics and Paleozoic Facies of the Marathon Geosyncline, West Texas, Permian Basin Section, SEPM, Publication 78-17, p. 89–93.

Rush, J., and Kerans, C., 2010, Stratigraphic response across a structurally dynamic shelf: The latest Guadalupian composite sequence at Walnut Canyon, New Mexico, U.S.A.: Journal of Sedimentary Research, v. 80, p. 808-828.

Saller, A., 1996, Differential compaction and basinward tilting of the prograding Capitan reef complex, Permian, west Texas and southeast New Mexico, USA: Sedimentary Geology, v. 101, p. 21–30.

Saller, A.H., Harris, P.M., Kirkland, B.L., and Mazzullo, S.J., 1999, Geologic framework of the Capitan depositional system—previous studies, controversies and content of this special publication, in Saller, A.H., Harris, P.M., Kirkland, B.L., and Mazzullo, S.J., eds., Geological Framework of the Capitan Reef: SEPM, Special Publication 65, p. 1–14.

Scotese, C.R., and McKerrow, W.S., 1990, Revised world maps and introduction, in McKerrow, W.S., and Scotese, C.R., eds., Palaeozoic Palaeogeography and Biogeography, The Geological Society of London, Memoir 12, p. 1–21.

Silver, B. A., and R. G. Todd, 1969, Permian cyclic strata, northern Midland and Delaware basins, West Texas and southeastern New Mexico: AAPG Bulletin, v. 53, no. 11, p. 2223-2251.

Smith, D.B., 1974a, Origin of tepees in upper Permian shelf carbonate rocks of Guadalupe Mountains, New Mexico: AAPG Bulletin, v. 58, p. 63-70.

Smith, D.B., 1974b, Sedimentation of Upper Artesia (Guadalupian) cyclic shelf deposits of northern Guadalupe Mountains, New Mexico: AAPG Bulletin, v. 58, p. 1699–1730.

Sonnenfeld, M.D., and Cross, T.A., 1993, Volumetric partitioning and facies differentiation within the Permian upper San Andres Formation of Last Chance Canyon, Guadalupe Mountains, New Mexico, *in* Loucks, R.G., and Sarg, J.F., eds., Carbonate Sequence Stratigraphy; Recent Developments and Applications, AAPG, Memoir 57, p. 435–474.

Stanton, R.J., Jr, and Pray, L.C., 2004, Skeletal-carbonate Neptunian dikes of the Capitan Reef; Permian, Guadalupe Mountains, Texas, U.S.A.: Journal of Sedimentary Research, v. 74, p. 805-816.

Tinker, S.W., 1996, Reservoir-scale sequence stratigraphy: McKittrick Canyon and 3-D subsurface examples, west Texas and New Mexico [unpublished Ph.D. thesis]: The University of Colorado, Boulder, Colorado, 245 p.

Tinker, S.W., 1998, Self-to-basin facies distributions and sequence stratigraphy of a steep-rimmed carbonate margin: Capitan depositional system, McKittrick Canyon, New Mexico and Texas: Journal of Sedimentary Research, v. 68, p. 1146-1174.

Tyrrell, W.W, JR, 1962, Petrology and stratigraphy of near-reef Tansill–Lamar strata, Guadalupe Mountains, Texas and New Mexico, in Permian of the central Guadalupe Mountains, Eddy County, New Mexico—Field Trip Guidebook and Geological Discussions, West Texas Geological Society, p. 59–69.

Van Wagoner, J. C., R. M. Mitchum, K. M. Campion, and V. D. Rahmanian, 1990, Siliciclastic sequence stratigraphy in well logs, cores and outcrops: concepts for high–resolution correlation of time and facies: AAPG Methods in Exploration Series 7, 55 p.

Walker, D.A., Golonka, J., Reid, A., and Reid, S., 1995, The effects of paleolatitude and paleogeography on carbonate sedimentation in the late Paleozoic, *in* Huc, A.Y., ed., Paleogeography, Paleoclimate, and Source Rocks, AAPG, Studies in Geology, no. 40, p. 133-155.

Ward, R.F., Kendall, C.G.ST.C., and Harris, P.M., 1986, Upper Permian (Guadalupian) facies and their association with hydrocarbons—Permian Basin, west Texas and New Mexico: AAPG Bulletin, v. 70, p. 239–262.

Wardlaw, B.R., Davydov, V., and Gradstein, F.M., 2005, The Permian Period, in Gradstein, F., Ogg, J., and Smith, A., eds., A Geologic Time Scale 2004: Cambridge, U.K., Cambridge University Press, p. 249–270.

Wilde, G.L., Rudine, S.F., and Lambert, L.L., 1999, Formal designation: Reef Trail Member, Bell Canyon Formation, and its significance for recognition of the Guadalupian–Lopingian boundary, in Saller, A.H., Harris, P.M., Kirkland, B.L., and Mazzullo, S.J., eds., Geologic Framework of the Capitan Reef, SEPM, Special Publication 65, p. 63–83.

Wilson, J.L., 1967, Cyclic and reciprocal sedimentation in Virgilian strata of southern New Mexico: Geological Society of America, Bulletin, v. 78, p. 805–818.

Wood, R., Dickson, J.A.D., and Kirkland-George, B., 1994, Turning the Capitan reef upside down: a new appraisal of the ecology of the Permian Capitan reef, Guadalupe Mountains, Texas and New Mexico: PALAIOS, v. 9. p. 422–427.

Wood, R., Dickson, J.A.D., and Kirkland, B.L., 1996, New observations on the ecology of the Permian Capitan reef, Texas and New Mexico: Paleontology, v. 39, p. 733-762.

Yang, K.M., and Dorobek, S.L., 1992, Mechanisms for late Paleozoic synorogenic subsidence of the Midland and Delaware basins, Permian Basin, Texas and New Mexico, *in* Mruk, D.H., and Curran, B.C., eds., Permian Basin Exploration and Production Strategies—Application of Sequence Stratigraphy and Reservoir Characteristic Concepts, Midland, Texas, West Texas Geological Society, Publication 92-91, p. 45–60.

Yang, K.M., and Dorobek, S.L., 1993, Late Paleozoic synorogenic stratigraphy and tectonic evolution of the Permian Basin, West Texas and New Mexico, *in* Gibbs, J., and Cromwell, D., eds., New Dimensions in the Permian Basin, Midland, Texas, West Texas Geological Society, Publication 93-93, p. 8–18.

Yang, K.M., and Dorobek, S.L., 1994, The Permian Basin of West Texas and New Mexico: Tectonic history of a ‘‘composite’’ foreland basin and its effects on stratigraphic development, in Dorobek, S.L., and Ross, G.M., eds., Stratigraphic Evolution of Foreland Basins, SEPM, Special Publication 52, p. 147–172.

Ye, H., Royden, L., Burfiel, C., and Schuepbach, M., 1996, Late Paleozoic deformation of interior North America: the greater ancestral Rocky Mountains: American Association of Petroleum Geologists, Bulletin, v. 80, p. 1397–1432.

Yurewicz, D.A., 1977, The origin of the massive facies of the Lower and Middle Capitan Limestone (Permian), Guadalupe Mountains, New Mexico and West Texas, *in* Hileman, M.E., and Mazzullo, S.J., eds., Upper Guadalupian Facies, Permian Reef Complex, Guadalupe Mountains, New Mexico and West Texas: San Diego, California, vol. 1, p. 45–92.

Vita

Charles Harman grew up in Southport, CT and graduated from St. Lawrence University in Canton, New York in 2009 with a BS in Geology *magna cum laude*. He wrote an undergraduate thesis on the carbonate facies and sequence development of the Aptian stage in Southern Croatia and won the W.A. Tarr Award from Sigma Gamma Epsilon. He moved to Austin, TX in the summer of 2009 to pursue a Masters at the Jackson School of Geoscience under Dr. Charlie Kerans. From 2009 to 2011 he worked as a research assistant for the Reservoir Characterization Research Laboratory (RCRL) and teaching assistant in the Department of Geological Sciences. He moved to Denver, CO in the fall of 2011 and now works for Whiting Petroleum.

Permanent email: charles.harman@gmail.com

This thesis was typed by Charles Harman.